RECENT DEVELOPMENTS IN SCIENTIFIC RESEARCH IV

EDITORS
Prof. Dr. Ayşegül GÜMÜŞ
Prof. Dr. Selçuk GÜMÜŞ

İKSAD
Publishing House

RECENT DEVELOPMENTS IN SCIENTIFIC RESEARCH IV

EDITORS

Prof. Dr. Ayşegül GÜMÜŞ

Prof. Dr. Selçuk GÜMÜŞ

AUTHORS

Prof. Dr. Selçuk GÜMÜŞ

Prof. Dr. Ayşegül GÜMÜŞ
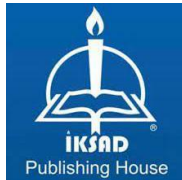
Assoc. Prof. Dr. Nurdan YAVUZ

Assoc. Prof. Dr. Zeynep Şilan TURHAN

Assist. Prof. Dr. Ayşegül Feray GÖKDERE

Assist. Prof. Dr. Erhan ÖZTÜRK

Lect. Dr. Yasemin KEŞKEK KARABULUT

MSc (PhD Student) Renas Ali ROSTM

ISBN: 978-625-378-435-5

Cover Design: İbrahim KAYA

December / 2025

Ankara / Türkiye

Size: 16x24cm

CONTENTS

PREFACE

This book seeks to illuminate the complexities of science, offering readers a comprehensive exploration of its principles, discoveries, and evolving frontiers. The book consists of seven chapters written by researchers from Bartin University, Iğdir University, and Van Yuzuncu Yil University. İn the first chapter of this book, phenanthroline based D-π-A type OLED molecules investigated for their TADF properties, in the second chapter, the results of a research on aromatic characther of triazaanthracenes have been reported, in the third chapter, the role of paleoclimate reconstructions in assessing climate model accuracy has been discussed, in the fourth chapter, the impact of human in lake sediments in Türkiye has been presented using palynological evidence, in the fifth chapter, structural design and electronic properties of pyridoquinolysis derivative OLED materials are examined. In the sixth chapter, coumarin–triazole hybrids as emerging anticholinergıc agents have been discussed deeply,and in the last chapter, eco-friendly pesticide design at the molecular level using pyrethrum extract components has been reported. We, as the editors, deeply appreciate the invaluable efforts of the contributors to this book. Our heartfelt thanks go especially to the İKSAD Publishing family, the scientific committee, the authors, and the readers whose support in the preparation, design, and printing of this work has been indispensable.

Prof. Dr. Ayşegül GÜMÜŞ
Prof. Dr. Selçuk GÜMÜŞ

CHAPTER 1

TADF PROPERTIES OF NOVEL D-π-A TYPE OLEDS

Prof. Dr. Selçuk GÜMÜŞ[1], Prof. Dr. Ayşegül GÜMÜŞ[2]

[1] Bartin University, Engineering, Architecture and Design Faculty, Department of Basic Sciences, Bartın, Turkey, sgumus@bartin.edu.tr, 0000-0002-8628-8943

[2] Bartin University, Faculty of Science, Department of Biotechnology, Bartın, Turkey, agumus@bartin.edu.tr, 0000-0002-1613-7074

1. INTRODUCTION

Organic Light Emitting Diodes (OLEDs) have revolutionized the world of display and lighting technologies, providing unparalleled advancements in terms of performance, flexibility, and energy efficiency. As a significant departure from traditional light-emitting diodes (LEDs), OLEDs use organic (carbon-based) materials to emit light when an electric current is applied. This fundamental difference in material composition allows OLEDs to offer a wide range of innovative possibilities, from ultra-thin, flexible displays to energy-efficient, high-quality lighting solutions. The working principle behind OLEDs is rooted in electroluminescence, where organic materials emit light upon the application of an electric current. These materials are typically applied in thin layers, with the most crucial layers being the emissive layer and the conductive layer. The emissive layer is where light is generated, and it consists of organic molecules or polymers that are capable of emitting light when electrons from the cathode meet holes from the anode. Unlike traditional LCDs that require an external backlight, OLEDs are "self-emissive," meaning each pixel generates its own light, providing exceptional contrast ratios and deep blacks. One of the most compelling features of OLEDs is their thinness and flexibility. OLEDs can be manufactured on flexible substrates, such as plastic or even fabric, making them ideal for applications in flexible, foldable, or rollable displays. This property has opened the door to new design possibilities, from curved television screens to flexible wearable displays and rollable smartphones. The ability to produce OLED panels with minimal thickness also results in displays that are lighter, more compact, and more energy-efficient than their traditional counterparts (Adachi, et al. 2001; Aydemir, et al. 2016; Atkins, et al. 2006; Baldo, et al. 1999; Baldo, et al. 1998; Baldo, et al. 1999).

OLED technology has quickly gained traction in various industries, particularly in consumer electronics. High-end televisions, smartphones, tablets, and monitors often incorporate OLED screens due to their superior color accuracy, fast refresh rates, and impressive contrast ratios. The ability to achieve true black levels by individually turning off pixels contributes to more vibrant, immersive visuals compared to other display technologies such as Liquid Crystal Displays (LCDs). OLED displays also consume less power when displaying darker images, making them more energy-efficient than traditional backlit displays.

Beyond displays, OLED technology is also making strides in lighting applications. OLED lighting panels offer a softer, more diffused light compared to traditional lighting solutions like LEDs and fluorescent bulbs. These panels are thinner, lighter, and can be shaped into a variety of forms, enabling their use in architectural lighting, automotive lighting, and even in innovative applications such as OLED-based light fixtures that can be embedded into surfaces or walls. Moreover, OLED lighting is highly energy-efficient, providing an eco-friendly alternative to conventional lighting sources.

Despite their impressive benefits, OLEDs face several challenges that must be overcome for the technology to reach its full potential. One of the main concerns is degradation—the organic materials used in OLEDs, particularly blue OLEDs, degrade over time with use. This degradation can result in reduced brightness, color shift, and even shortened lifespans, which has limited their use in certain applications. Moisture sensitivity is another significant hurdle; OLEDs are highly susceptible to damage from oxygen and water vapor, requiring them to be carefully encapsulated to protect the organic layers from environmental exposure. Additionally, OLEDs are prone to a phenomenon known as burn-in, where static images that remain on the screen for extended periods can cause permanent damage to specific areas of the display, resulting in ghost images or uneven color reproduction. While manufacturers have made significant progress in mitigating burn-in effects through various techniques, this remains a challenge for long-term usage. Another challenge is the high manufacturing cost of OLEDs. Compared to traditional LCD panels, OLEDs are more expensive to produce due to the complexity of their manufacturing processes and the cost of organic materials. However, as production techniques improve and economies of scale are realized, the cost of OLED technology is expected to decrease, making it more accessible for a wider range of applications and products.

Fluorescence and phosphorescence are two distinct but related phenomena of photoluminescence, where materials absorb light (or other forms of electromagnetic radiation) and subsequently re-emit it as visible light. While both processes involve the excitation of electrons to higher energy states followed by their relaxation and emission of light, the key differences lie in the duration of the emitted light and the mechanisms that govern these processes.

These differences have significant implications for a wide range of applications across various scientific and industrial fields.

Fluorescence is characterized by a rapid emission of light that occurs almost instantaneously after the material absorbs photons. This phenomenon typically happens on the order of nanoseconds, with the emitted light having a longer wavelength (and lower energy) than the absorbed light. The process is highly efficient and ceases immediately once the excitation source is removed. Fluorescence plays a crucial role in numerous applications, including biological imaging, environmental monitoring, and fluorescence-based sensors, thanks to its fast response and high sensitivity.

In contrast, phosphorescence involves a slower emission of light, with the light persisting much longer than in fluorescence. After the material absorbs energy, the electron undergoes a transition to a lower-energy triplet state, which is less stable and causes a delayed release of light. This delayed emission can last from microseconds to hours, depending on the material. Phosphorescence is widely used in applications requiring afterglow effects, such as in glow-in-the-dark materials, safety signage, and various forms of security printing (Binggeli, et al. 2012; Tsai, et al. 2014; Czerwieniec, et al. 2011; Çiçek, et al. 2018; de Sa, et al. 2000; Endo, et al. 2009; Endo, et al. 2011).

While both phenomena are rooted in the same fundamental principle of electroluminescence, their differences in emission time and underlying mechanisms make them suitable for very different uses. Fluorescence is typically favored for applications that require fast, high-efficiency light emission, whereas phosphorescence is employed where prolonged light emission is desired (Fourassier, 1984; Förster, and Kasper 1954; Ivanov, et al. 2006; Kalyani, et al. 2017).

A Jablonski diagram is a graphical representation used in photophysics to illustrate how a molecule absorbs and emits light by showing its electronic energy levels and the transitions between them. It includes singlet states (S_0, S_1, S_2) where electrons have paired spins, and triplet states (T_1, T_2) where spins are unpaired. When a molecule absorbs a photon, it is excited from the ground state S_0 to a higher singlet state, after which it may lose some energy without emitting light through internal conversion. It then returns to the ground state by emitting light as fluorescence, typically within nanoseconds and at a lower energy than the absorbed light. Alternatively, the molecule may undergo intersystem

crossing to a triplet state, from which it can slowly emit light as phosphorescence—a spin-forbidden and therefore much slower process that can last milliseconds to seconds. The Jablonski diagram provides a concise way to visualize these radiative and non-radiative pathways (Figure 1).

Figure 1. Three dimensional Jablonski Diagram

A series of pyrene-derived molecules (Figure 2) were designed and subsequently examined to determine their structural and electronic characteristics through Density Functional Theory analysis. These donor–acceptor (D-π-A) systems exhibit promising features for use in organic optoelectronic technologies, including organic solar cells, OLEDs, and fluorescent organic materials.

Figure 2. Structure of the parent compound (Pyrene (**P**))

2. METHOD OF CALCULATION

The ground-state (S_0) three-dimensional geometries of all molecules were optimized within the framework of Density Functional Theory (DFT) (Kohn and Sham, 2015), using the Gaussian 16W computational suite (Frisch et al., 2016). In these calculations, the hybrid exchange–correlation functionals B3LYP and CAM-B3LYP were applied. B3LYP combines Becke's three-parameter exchange formalism (Becke, 1988) with the Lee–Yang–Parr correlation functional (Lee et al., 1988). Because these functionals incorporate empirical constraints derived from the uniform electron gas approximation (Zhao and Truhlar, 2006, 2008; Karton et al., 2008), they mitigate some of the limitations encountered in conventional DFT, particularly in describing dispersion interactions. Vibrational frequency analyses were performed using the same basis sets as those employed for the geometry optimizations. The lack of imaginary frequencies confirmed that the obtained structures represent at least local minima on the potential energy surface. Standard vibrational mode evaluation was carried out for the 3N-6 degrees of freedom, where N denotes the total number of atoms in the system.

Minimum-energy structures of the relevant excited states were subsequently determined by optimizing low-lying singlet (S) and triplet (T) states. Time-Dependent DFT (TD-DFT) calculations with several hybrid functionals and basis sets were then used to compute vertical excitation energies and oscillator strengths for the lowest singlet and triplet transitions at the ground-state geometries (Casida et al., 1998). These TD-DFT results provided the electronic absorption characteristics, including peak absorption wavelengths, oscillator strengths, and dominant configuration contributions.

Although deviations exist in certain cases, previous studies indicate that the PBE0, wB97XD, and CAM-B3LYP functionals generally reproduce experimental excitation energies with higher accuracy (Yanez et al., 2017). Therefore, the TD-DFT analyses in this work were conducted using the B3LYP/6-311++G(d,p) level of theory, and the computed results were subsequently compared.

3. RESULTS AND DISCUSSION

The global demand for sustainable and scalable energy solutions has intensified interest in novel concepts that rely on affordable, environmentally benign materials with broad availability and structural diversity. Compared with conventional inorganic semiconductors such as silicon, organic semiconductor systems offer lower production costs and enable the fabrication of lightweight, flexible devices, largely due to their exceptionally high optical absorption coefficients.

In fluorescent organic materials, only about 25% of generated excitons typically contribute to radiative decay (Baldo et al., 1999; Segal et al., 2003). The incorporation of phosphorescent emitters can elevate this fraction to unity by exploiting efficient spin–orbit coupling mediated by heavy metals such as iridium and platinum (Baldo et al., 1998; Wilson et al., 2001; Sun et al., 1999; Adachi et al., 2001; O'Brien et al., 1999; Baldo et al., 1999). Although this approach dramatically enhances emissive efficiency, the reliance on scarce noble metals increases OLED fabrication costs. Traditionally, devices employing fluorescence and phosphorescence are constrained by external quantum efficiency (EQE) ceilings of approximately 5% and 20%, respectively. A more recent strategy aims to surpass these limits by enabling the upconversion of non-radiative triplet states into emissive singlet states (Meerholz and Müller, 2001).

Thermally Activated Delayed Fluorescence (TADF) materials have consequently gained considerable attention, prompting the synthesis of many new compounds capable of exhibiting this phenomenon (Endo et al., 2009, 2011; Czerwieniec and Yersin, 2011; Leitl et al., 2013). TADF operates by minimizing the singlet–triplet energy gap (ΔE_{ST}) between the lowest excited singlet (S_1) and triplet (T_1) states (Figure 3). This reduction is achieved by spatially decoupling the highest occupied molecular orbital (HOMO) and lowest unoccupied molecular orbital (LUMO), which facilitates reverse intersystem crossing (R_{ISC}) that thermally promotes triplet excitons back to the singlet manifold according to Boltzmann statistics. This "singlet harvesting" pathway increases the proportion of radiative excitons (Endo et al., 2011), allowing EQE values to exceed classical fluorescence limits and approach those observed in phosphorescent OLEDs (Leitl et al., 2013).

A diminished ΔE_{ST} lowers electron–electron repulsion in the triplet state by reducing the overlap between the molecular wave functions of the ground and excited states (Endo et al., 2009). In this context, the HOMO corresponds to the electronic ground state, whereas the LUMO represents the excited state. Designing molecules in which HOMO and LUMO densities are localized on donor and acceptor fragments, respectively, is an effective means of reducing this overlap. Steric decoupling of these fragments—achieved through bulky substituents or rigid spiro-linked architectures—further enhances orbital separation and thus supports efficient TADF behavior (Endo et al., 2011).

Building upon these findings, this research introduces a series of donor-acceptor (D-π-A) pyrene-based derivatives as potential candidates for thermally activated delayed fluorescence (TADF) emitters (Figure 3 and Figure 4). Pyrene, the parent compound, is a solid polycyclic aromatic hydrocarbon (PAH) with the chemical formula $C_{16}H_{10}$, consisting of four fused benzene rings. It is a component of coal tar. Commercially, pyrene and its derivatives are used in the production of dyes and dye precursors, including pyranine and naphthalene-1,4,5,8-tetracarboxylic acid. Pyrene displays strong absorbance in the UV-Vis region, with three distinct absorption peaks around 330 nm in DCM (dichloromethane). The emission spectrum closely mirrors the absorption, peaking around 375 nm (Lindsey et al., 2014). The signal morphology changes depending on the solvent. Pyrene derivatives are also valuable as molecular probes in fluorescence spectroscopy, exhibiting high quantum yields and extended lifetimes (0.65 and 410 nanoseconds, respectively, in ethanol at 293 K). Pyrene was the first molecule in which excimer behavior was observed, with the excimer emission appearing around 450 nm, a discovery made by Theodor Förster in 1954 (Förster, Th.; Kasper, K., 1954).

In this study, pyrene was modified to create eight new compounds by introducing π-linkers (benzene and furan) in combination with electron-withdrawing groups (cyano groups or cyano-containing organic groups) (Figure 3). The design concept builds on extensive spectroscopic studies of the parent pyrene compound (Khodaee et al., 2012; Nishida et al., 2004; Ivanov et al., 2006). By combining the strong electron-withdrawing properties of pyrene with various acceptor units, this work aims to develop novel TADF-active compounds.
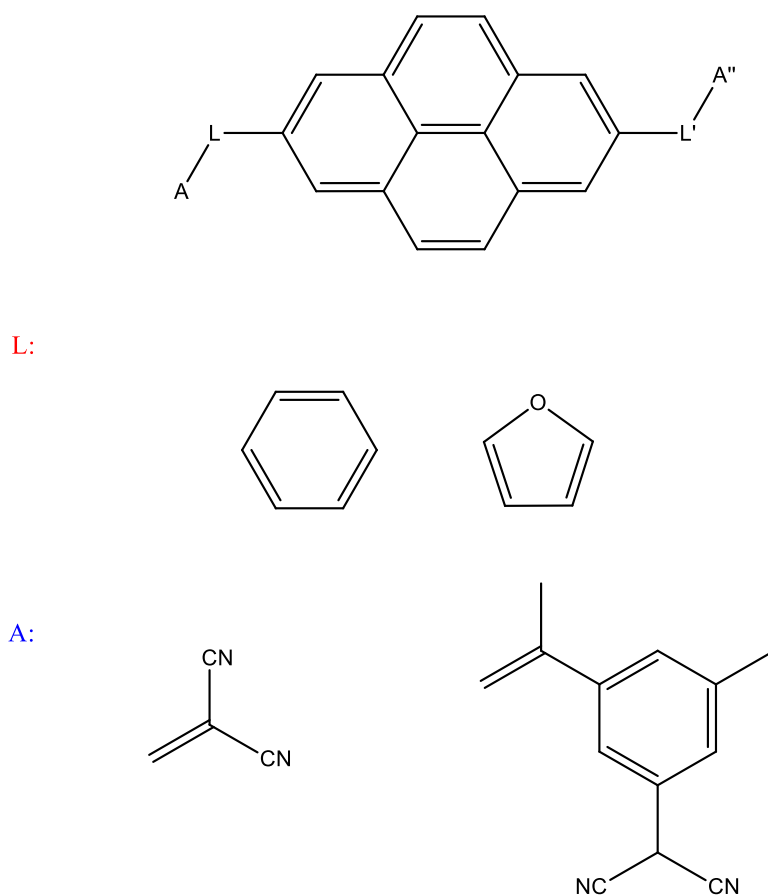
L:

A:

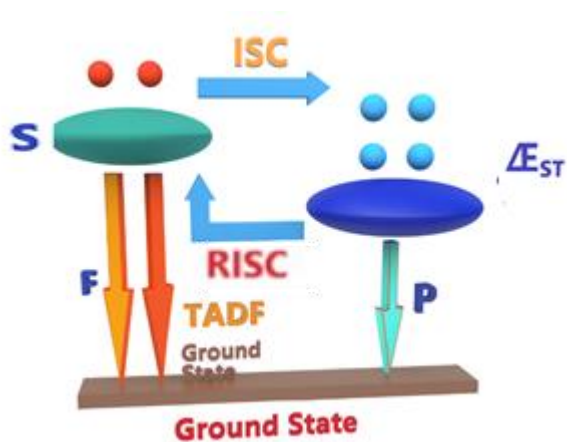**Figure 3.** Structures of the compounds in this study

Figure 4. TADF mechanism on Jablonski Diagram

3.1. Semiconductor Properties

The electronic structure of all organic semiconductors is primarily determined by the conjugation of π-electrons. In conjugated organic systems, carbon-carbon bonds alternate between single and double bonds. Single bonds, with electrons that are localized, are known as σ-bonds, while double bonds consist of a σ-bond and a π-bond. The π-electrons become delocalized due to the overlap of π orbitals along the conjugation chain, allowing them to move across the carbon atoms. The Lowest Unoccupied Molecular Orbital (LUMO) corresponds to the unfilled π-bands, while the Highest Occupied Molecular Orbital (HOMO) represents the filled π-bands. Organic semiconductors typically have band gaps (E) ranging from 0.5 to 4 eV (Atkins et al., 2006).

The geometry-optimized structures of the new compounds are shown in Figure 5. Frontier molecular orbital energies were calculated using the B3LYP/6-311+G(d,p) method, with results summarized in Table 1. All the calculated band gap (ΔE) values were found to be under 4 eV. As anticipated, incorporating donor units with acceptor groups lowers the energy gap between frontier molecular orbitals by lengthening the conjugation path. The parent compound (A) had a band gap of 3.70 eV, which decreased when donor units were added. As a result, all compounds are promising candidates for use as semiconductors, with the smallest band gaps found in compounds 5 and 8.

Figures 5 and 6 show the optimized geometric structures and the 3D frontier molecular orbital energy diagrams for the compounds. These diagrams offer insights into the compounds' reactivity. The LUMO reflects the system's Lewis acidity, while the HOMO indicates its basicity. Therefore, studying these frontier molecular orbitals is crucial, as they determine the reactive centers in the molecules. Identifying the atoms that contribute to these orbitals is equally significant.

For the compounds to be suitable for thermally activated delayed fluorescence (TADF), a clear separation between HOMO and LUMO is necessary to ensure low exchange energy. This separation can be facilitated by steric hindrance, which induces twisting between donor and acceptor units (Nakagawa et al., 2012; Mehes et al., 2012; Nasu et al., 2013). In donor-acceptor (D-A) structures, the HOMOs are mainly localized on the donor components (Figure 6), while the LUMOs are primarily located on the acceptor core, which includes pyrazine and strongly electron-withdrawing cyano groups.

The large dihedral angles (about 25–90°) between the donor units and the pyrene-benzene core with cyano groups result in a distinct spatial separation between the HOMO and LUMO orbitals. This ensures that the HOMO is concentrated on the donor regions and the LUMO on the acceptor regions of the system.

Table 1. Results of computations (All data are in eV)

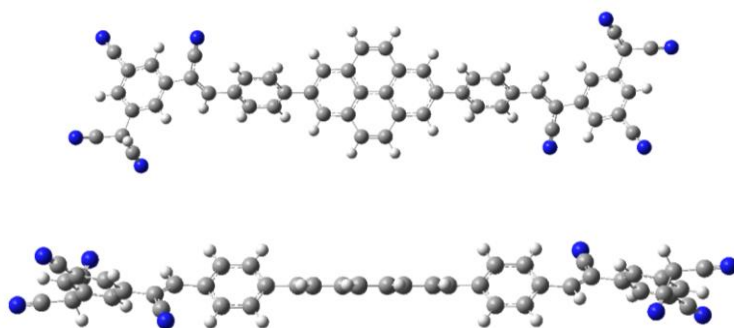| Compound	DFT			TD-DFT (ΔE_{ST})
	B3LYP/6-311++(d,p)			B3LYP
	HOMO	LUMO	ΔE	6-311++(d,p)
P	-6.70	-3.00	3.70	0.53
1	-5.26	-2.69	2.37	0.44
2	-5.78	-3.09	2.69	0.10
3	-5.34	-3.32	2.02	0.12
4	-5.20	-2.81	2.39	0.07
5	-4.74	-2.75	1.99	0.10
6	-5.06	-2.32	2.74	0.63
7	-5.89	-2.78	3.12	0.17
8	-5.17	-2.84	2.33	0.12

Figure 5. Top and side view of geometry optimized structure of one of the eight compounds under study.
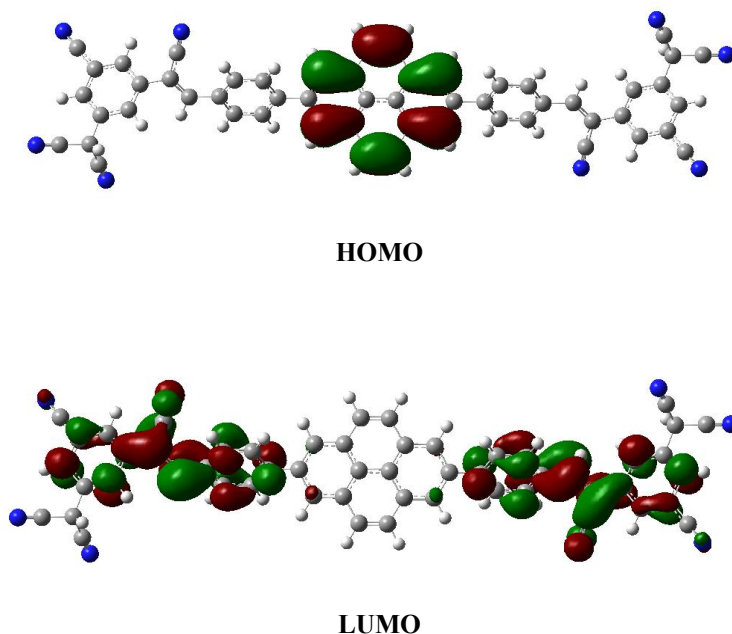
HOMO

LUMO

Figure 6. HOMO and LUMO scheme of the structure obtained at B3LYP/6-311++G(d,p) level.

The pyrene molecule (P), which is rigid and planar, has a fully conjugated core ring with two enes on either side and cyano groups, causing the HOMO and LUMO orbitals to be spread throughout the structure. To effectively separate these frontier molecular orbitals, substituents (R) were added to restrict their free rotation (Figure 5). The geometry-optimized structures for compounds 1–8 are shown in Figures 5 and 6. While excessive conjugation in planar configurations initially impeded orbital separation, introducing tilted geometries with significant dihedral angles successfully created a distinct separation between the HOMO and LUMO.

Modifying the substituents affected the energy levels of the HOMO and LUMO, improving the compounds' semiconducting characteristics. Recent research on oligomeric thiophene systems for OLED applications (Sengoku et al., 2012) inspired efforts to modify substituents in highly conjugated systems. The goal was to separate the HOMO and LUMO distributions and decrease the energy gap between frontier molecular orbitals by extending conjugation. Although the geometry-optimized structures did not show significantly more

tilted configurations, the extended systems led to a narrower HOMO-LUMO gap due to an increase in HOMO energy (Figures 5 and 6).

Compounds 4 and 7, with donor-acceptor dihedral angles of 43° for benzene and 38° for furan, exhibited strong potential for separating the HOMO and LUMO distributions. In all compounds (1–8), the HOMOs were localized on the donor regions, while the LUMOs were localized on the acceptor regions, ensuring robust semiconducting properties ideal for OLED applications.

3.2. TADF Properties

Achieving a narrow singlet-triplet energy gap (ΔE_{ST}) between the S_1 and T_1 states is a key design requirement for Thermally Activated Delayed Fluorescence (TADF) molecules. This condition is met only when the molecule's lowest-energy transition has a small singlet-triplet exchange energy (Turro, 1991). Research on novel TADF emitters mainly focuses on intramolecular donor-acceptor (D-A) type molecules, like the one examined here (Li et al., 2014). For designing full-color TADF molecules with distinct localization of HOMO and LUMO on different molecular fragments, selecting the appropriate donor-acceptor units is crucial. Time-Dependent Density Functional Theory (TD-DFT) calculations, conducted at the B3LYP/6-311++G(d,p) level, provided valuable insights into the geometric and electronic structures of compounds 1–8. Table 1 summarizes the HOMO and LUMO energies for these compounds along with their ΔE_{ST} values.

The separation of frontier molecular orbitals plays a significant role in narrowing the ΔE_{ST}. For molecule A, the calculated ΔE_{ST} using the B3LYP/6-311++G(d,p) method was 0.53 eV. Compounds 1–8 have been identified as strong TADF candidates, with ΔE_{ST} values under 0.50 eV being considered optimal for TADF efficiency. In particular, compounds 2, 3, 5, and 8 exhibit nearly degenerate T_1 and S_1 levels, fully twisted geometries, and significantly separated HOMO-LUMO distributions, making them the most promising TADF emitters. For these compounds, especially 2, 3, 5, and 8, the ΔE_{ST} values predicted by TD-DFT are sufficiently small to allow thermal repopulation of the S_1 state via reverse intersystem crossing (R_{ISC}) from T_1 to S_1. Among them, compound 8 shows the greatest potential due to its highly separated HOMO and LUMO orbitals and the narrowest S_1-T_1 energy gap.

The lowest-energy excited states for all compounds are governed by an intramolecular charge transfer (ICT) mechanism with low exchange energy. Although the pyrene-furan-cyano derivative (3) has a distinct HOMO-LUMO distribution and a 90° dihedral angle, its ΔE_{ST} of 0.63 eV is relatively high, making it less competitive. In contrast, the pyrene-benzene-cyano system (4), with a 90° dihedral angle and a ΔE_{ST} of just 0.07 eV, stands out as the most promising candidate due to its exceptionally narrow ΔE_{ST}.

4. CONCLUSION

Nonlinear optical (NLO) phenomena serve as the foundation for various applications in optical sensing, communication systems, and materials science. These phenomena enable us to manipulate light by altering its color, reshaping it in space and time, and producing some of the shortest events ever achieved by humanity. In contrast to linear optics, where a light wave interacts with a molecule, causing it to vibrate and emit a secondary wave that interferes with the original, NLO materials exhibit unique and advanced optical behaviors.

Nonlinear optical (NLO) phenomena occur when the response of a material to an optical field becomes nonlinear at high light intensities, meaning the material's polarization is no longer directly proportional to the electric field of the light. This leads to a variety of effects that are crucial in modern optics and photonics, such as second-harmonic generation (SHG), where two photons of the same frequency combine to produce a new photon with twice the frequency; third-harmonic generation (THG), which involves three photons combining to create a photon at three times the original frequency; and optical Kerr effect, where the refractive index of a material changes with the intensity of the light, leading to phenomena like self-focusing. Other important NLO phenomena include four-wave mixing (FWM), where interactions between four light waves generate new frequencies, and optical rectification, which creates a static electric field from high-intensity light. Additionally, photon squeezing reduces quantum fluctuations in light, making it valuable for quantum optics, while sum-frequency generation (SFG) and difference-frequency generation (DFG) allow for the production of new frequencies by combining or subtracting the frequencies of two photons. These effects are not only significant for basic research but also for a variety of practical applications, including in

telecommunications, where they are used in optical amplifiers and fiber-optic communication systems, laser technology for frequency conversion, quantum computing and sensing for enhanced measurements, and medical imaging in techniques like two-photon microscopy. Nonlinear optics is also applied in developing optical limiters to protect sensitive devices from high-intensity light, and in nanomaterials, where the unique size and electronic properties of materials like quantum dots, graphene, and carbon nanotubes lead to enhanced nonlinear responses. The use of nonlinear materials, such as organic materials (e.g., conjugated polymers) and inorganic crystals (e.g., KTP and $LiNbO_3$), is integral in shaping next-generation optical devices for faster, more efficient, and more versatile technologies across various scientific and industrial fields.

Pyrene-based organic systems are of particular interest due to their versatile functions, including applications in medicine, chemosensing, and the development of optical materials. As a result, there has been increasing interest in exploring compounds with potential nonlinear optical (NLO) activity. This study uses computational methods to investigate pyrene-based molecules (1–8) with potential NLO properties, aiming to better understand their electronic and structural characteristics. Since NLO materials often exhibit OLED (Organic Light Emitting Diode) activity, these compounds were also analyzed theoretically for their semiconducting properties. Additionally, the compounds' potential for thermally activated delayed fluorescence (TADF) was evaluated to assess their ability to enhance quantum yield through fluorescence, which is driven by excitation and subsequent emission processes. In this study, well-known donor molecules like anthracene were paired with commonly used acceptors to design potential TADF emitters. Density Functional Theory (DFT) calculations at various theoretical levels were carried out to analyze the structural and electronic properties of these compounds. Among the candidates, compounds 9 and 15 were identified as the most promising TADF emitters due to their well-separated HOMO-LUMO orbitals and favorable ΔE_{ST} values. Moreover, all compounds exhibited interfrontier molecular orbital energy gaps below 4.0 eV, highlighting their potential as semiconducting materials.

REFERENCES

1. Adachi, C., Baldo, M. A., Thompson, M. E., & Forrest, S. R. (2001). Nearly 100% internal phosphorescence efficiency in an organic light-emitting device. *Journal of Applied Physics, 90*(10), 5048–5051. DOI: 10.1063/1.1417016

2. Aydemir, M., Haykır, G., Battal, A., Jankus, V., Sugunan, S. K., Dias, F. B., Attar, H., Türksoy, F., Tavaslı, M., & Monkman, A. P. (2016). High efficiency OLEDs based on anthracene derivatives: The impact of electron donating and withdrawing group on the performance of OLED. *Organic Electronics, 30*, 149–157. DOI: 10.1016/j.orgel.2016.01.012

3. Atkins, P., Overton, T., Rourke, J., Weller, M., Armstrong, F., & Shriver, D. (2006). *Inorganic Chemistry* (4th ed.). Oxford University Press.

4. Baldo, M. A., O'Brien, D. A., Thompson, M. E., & Forrest, S. R. (1999). Excitonic singlet-triplet ratio in a semiconducting organic thin film. *Physical Review B, 60*(20), 14422–14428. DOI: 10.1103/PhysRevB.60.14422

5. Baldo, M. A., O'Brien, D. F., You, Y., Shoustikov, A., Sibley, S., Thompson, M. E., & Forrest, S. R. (1998). Highly efficient phosphorescent emission from organic electroluminescent devices. *Nature, 395*(6698), 151–154. DOI: 10.1038/25955

6. Baldo, M. A., Lamansky, S., Burrows, P. E., Thompson, M. E., & Forrest, S. R. (1999). Very high-efficiency green organic light-emitting devices based on electrophosphorescence. *Applied Physics Letters, 75*(1), 4–6. DOI: 10.1063/1.124289

7. Becke, A. D. (1988). Density-functional exchange-energy approximation with correct asymptotic behavior. *Physical Review A, 38*(6), 3098–3100. DOI: 10.1103/PhysRevA.38.3098

8. Binggeli, C. (2012). *Interior Graphic Standards: Student Edition*. Wiley.

9. Tsai, Y. S., Hong, L. A., Juang, F. S., & Chen, C. Y. (2014). Blue and white phosphorescent organic light emitting diode performance improvement by confining electrons and holes inside double emitting layers. *Journal of Luminescence, 153*, 312–316. DOI: 10.1016/j.jlumin.2014.05.030

10. Casida, M. E., Jamorski, C., Casida, K. C., & Salahub, D. R. (1998). Molecular excitation energies to high-lying bound states from time-

dependent density-functional response theory: Characterization and correction of the time-dependent local density approximation ionization threshold. *Journal of Chemical Physics, 108*(11), 4439–4449. DOI: 10.1063/1.476037

11. Czerwieniec, R., Yu, J., & Yersin, H. (2011). Blue-Light Emission of Cu(I) Complexes and Singlet Harvesting. *Inorganic Chemistry, 50*(17), 8293–8301. DOI: 10.1021/ic2012898

12. Çiçek, B., Çalışır, Ü., Tavaslı, M., Tülek, R., & Teke, A. (2018). Synthesis and optical characterization of novel carbazole Schiff bases. *Journal of Molecular Structure, 1153*, 42–47. DOI: 10.1016/j.molstruc.2017.10.078

13. de Sa, G. F., Malta, O. L., de Mello, D. C., Simas, A. M., Longo, R. L., Santa-Cruz, P. A., & da Silva, E. F. (2000). Spectroscopic properties and design of highly luminescent lanthanide coordination complexes. *Coordination Chemistry Reviews, 196*, 165–195. DOI: 10.1016/S0010-8545(99)00152-7

14. Endo, A., Ogasawara, M., Takahashi, A., Yokoyama, D., Kato, Y., & Adachi, C. (2009). Thermally activated delayed fluorescence from Sn4+–porphyrin complexes and their application to organic light emitting diodes — A novel mechanism for electroluminescence. *Advanced Materials, 21*(45), 4802–4806. DOI: 10.1002/adma.200902276

15. Endo, A., Sato, K., Yoshimura, K., Kai, T., Kawada, A., Miyazaki, H., & Adachi, C. (2011). Efficient up-conversion of triplet excitons into a singlet state and its application for organic light emitting diodes. *Applied Physics Letters, 98*(8), 083302–083302. DOI: 10.1063/1.3551298

16. Frisch, M. J., Trucks, G. W., Schlegel, H. B., Scuseria, G. E., Robb, M. A., Cheeseman, J. R., Scalmani, G., Barone, V., Petersson, G. A., Nakatsuji, H., Li, X., Caricato, M., Marenich, A. V., Bloino, J., Janesko, B. G., Gomperts, R., Mennucci, B., Hratchian, H. P., Ortiz, J. V., Izmaylov, A. F., Sonnenberg, J. L., Williams-Young, D., Ding, F., Lipparini, F., Egidi, F., Goings, J., Peng, B., Petrone, A., Henderson, T., Ranasinghe, D., Zakrzewski, V. G., Gao, J., Rega, N., Zheng, G., Liang, W., Hada, M., Ehara, M., Toyota, K., Fukuda, R., Hasegawa, J., Ishida, M., Nakajima, T., Honda, Y., Kitao, O., Nakai, H., Vreven, T., Throssell, K.,

Montgomery, Jr., J. A., Peralta, J. E., Ogliaro, F., Bearpark, M. J., Heyd, J. J., Brothers, E. N., Kudin, K. N., Staroverov, V. N., Keith, T. A., Kobayashi, R., Normand, J., Raghavachari, K., Rendell, A. P., Burant, J. C., Iyengar, S. S., Tomasi, J., Cossi, M., Millam, J. M., Klene, M., Adamo, C., Cammi, R., Ochterski, J. W., Martin, R. L., Morokuma, K., Farkas, O., Foresman, J. B., & Fox, D. J. (2016). *Gaussian, Inc.*, Wallingford CT.

17. Fourassier, C. (1984). Luminescence. *Encyclopedia of Inorganic Chemistry*. Academic Press.

18. Förster, T., & Kasper, K. (1954). Ein Konzentrationsumschlag der Fluoreszenz. *Zeitschrift für Physikalische Chemie, 1*(5–6), 275–277. DOI: 10.1515/zpch-1954-0109

19. Ivanov, M. A., Puzyk, M. V., & Balashev, K. P. (2006). Spectroscopic and electrochemical properties of dichlorodiimine complexes of Au(III) and Pt(II) with 1,4-diazine derivatives of o-phenanthroline. *Russian Journal of General Chemistry, 76*(6), 843–848. DOI: 10.1134/S107036320606022X

20. Kalyani, N. T., Swart, H., & Dhoble, S. J. (2017). Principles and applications of organic light emitting diodes (OLEDs). *Woodhead Publishing.*

21. Kohn, W., & Sham, L. J. (1965). Self-consistent equations including exchange and correlation effects. *Physical Review, 140*(4A), 1133–1138. DOI: 10.1103/PhysRev.140.A1133

22. Karton, A., Tarnopolsky, A., Lamre, J. F., Schatz, G. C., & Martin, J. M. L. (2008). Highly accurate first-principles benchmark data sets for the parametrization and validation of density functional and other approximate methods. Derivation of a robust, generally applicable, double-hybrid functional for thermochemistry and thermochemical kinetics. *Journal of Physical Chemistry A, 112*(50), 12868–12886. DOI: 10.1021/jp805586g

23. Khodaee, Z., Yahyazadeh, A., Mahmoodi, N. O., Zanjanchi, M. A., & Azimi, V. (2012). One-pot synthesis and characterization of new cuprous pyrazinoporphyrazines containing peripherally functionalized units. *Journal of Molecular Structure, 1029*, 92–97. DOI: 10.1016/j.molstruc.2012.03.037

24. Lee, C., Yang, W., & Parr, R. G. (1988). Development of the Colle–Salvetti correlation energy formula into a functional of the electron density. *Physical Review B, 37*(2), 785–789. DOI: 10.1103/PhysRevB.37.785

25. Leitl, M. J., Küchle, F. R., Mayer, H. A., Wesemann, L., & Yersin, H. (2013). Brightly blue and green emitting Cu(I) dimers for singlet harvesting in OLEDs. *Journal of Physical Chemistry A, 117*(48), 11823–11836. DOI: 10.1021/jp407706u

26. Li, P., Cui, Y., Song, C., & Zhang, H. (2017). A systematic study of phenoxazine-based organic sensitizers for solar cells. *Dyes and Pigments, 137*, 12–23. DOI: 10.1016/j.dyepig.2016.09.023

27. Li, J., Zhang, Q., Nomura, H., Miyazaki, H., & Adachi, C. (2014). Thermally activated delayed fluorescence from nπ* to nπ* up-conversion and its application to organic light-emitting diodes. *Applied Physics Letters, 105*(1), 013301–013304. DOI: 10.1063/1.4891059

28. Lindsey, J., et al. (2014). Anthracene. *PhotochemCAD*. Retrieved February 20, 2014, from https://www.photochemcad.com

29. Liu, Y. F., Feng, J., Zhang, Y. F., Cui, H. F., Yin, D., Bi, Y. G., Song, J. F., Chen, Q. D., & Sun, H. B. (2014). Improved efficiency of indium-tin-oxide-free flexible organic light-emitting devices. *Organic Electronics, 15*, 478–483. DOI: 10.1016/j.orgel.2013.11.014

30. McKeever, S. W. (1985). *Thermoluminescence in Solids*. Cambridge University Press.

31. Meerholz, K., & Müller, D. C. (2001). Outsmarting waveguide losses in thin-film light-emitting diodes. *Advanced Functional Materials, 11*(4), 251–253. DOI: 10.1002/1616-301X(200103)11:4<251::AID-ADFM251>3.0.CO;2-H

32. Mehes, G., Nomura, H., Zhang, Q., Nakagawa, T., & Adachi, C. (2012). Enhanced electroluminescence efficiency in a spiro-acridine derivative through thermally activated delayed fluorescence. *Angewandte Chemie International Edition, 51*(47), 11311–11315. DOI: 10.1002/anie.201205398

33. Nakagawa, T., Ku, S. Y., Wong, K. T., & Adachi, C. (2012). Electroluminescence based on thermally activated delayed fluorescence generated by a spirobifluorene donor–acceptor structure. *Chemical Communications, 48*(52), 9580–9582. DOI: 10.1039/c2cc34898j

34. Nasu, K., Nakagawa, T., Nomura, H., Lin, C. J., Cheng, C. H., Tseng, M. R., Yasuda, T., & Adachi, C. (2013). A highly luminescent spiro-anthracenone-based organic light-emitting diode exhibiting thermally activated delayed fluorescence. *Chemical Communications, 49*(50), 10385–10387. DOI: 10.1039/c3cc45871f

35. Nishida, J. I., Murai, S., Fujiwara, E., Tada, H., Tomura, M., & Yamashita, Y. (2004). Preparation, characterization, and FET properties of novel dicyanopyrazinoquinoxaline derivatives. *Organic Letters, 6*(11), 2007–2010. DOI: 10.1021/ol0493039

CHAPTER 2

INVESTIGATION OF AROMATIC CHARACTHER OF TRIAZAANTHRACENES

Prof. Dr. Selçuk GÜMÜŞ[1]

[1] Bartin University, Engineering, Architecture and Design Faculty, Department of Basic Sciences, Bartın, Turkey, sgumus@bartin.edu.tr, 0000-0002-8628-8943

1. INTRODUCTION

Aromaticity is a chemical property of profound significance, denoting an exceptional degree of thermodynamic stability in certain organic molecules. The term, first coined in the 19th century, originally referred to the distinctive, often pleasing aroma of many of its compounds, such as those derived from resins and natural extracts—benzene and its derivatives being the primary examples. Today, however, the meaning is purely structural and electronic: aromaticity describes the unique enhancement in stability due to a continuous, cyclic system of delocalized pi electrons. This stabilization energy is far greater than the energy typically gained from simple conjugation, making these molecules chemically distinct from ordinary unsaturated compounds like alkenes.

The foundational example of this phenomenon is benzene C_6H_6. When first studied, chemists were perplexed by its formula, C_6H_6, which suggested a highly unsaturated and therefore highly reactive molecule, similar to an alkyne. Yet, benzene was found to be remarkably stable and unreactive, resisting the common addition reactions that would easily occur with simple alkenes. Its true nature was captured by August Kekulé, who proposed a cyclic structure with alternating single and double bonds. However, even Kekulé's oscillating structures—known as resonance structures—failed to fully explain the molecule's complete uniformity. X-ray crystallography later confirmed that all six carbon-carbon bonds in benzene are identical, possessing a length (1.39 Å) intermediate between a typical single bond (1.54 Å) and a typical double bond (1.34 Å). This is the physical evidence of electron delocalization. The six p orbitals on the sp2 hybridized carbon atoms overlap laterally and continuously around the entire ring, creating a doughnut-shaped cloud of electron density both above and below the plane of the ring. This system of shared electrons is the source of the immense stability.

To systematically predict this special stability, German physical chemist Erich Hückel developed a set of criteria in 1931 that form the cornerstone of modern understanding. A compound must satisfy four rigorous conditions to be classified as aromatic. Failure to meet even a single criterion will render the molecule either non-aromatic or, in a particularly dramatic case, antiaromatic.

The first two criteria define the necessary geometry: The molecule must be cyclic, forming a closed ring structure, and it must be planar, meaning all

atoms in the ring must lie in the same or nearly the same geometric plane. Planarity is critical because it ensures that all the p orbitals are parallel to each other, allowing for the continuous, uninterrupted overlap necessary for delocalization. If a molecule has a sufficient number of pi electrons but is forced into a non-planar "tub" or "boat" conformation, the conjugation is broken and aromaticity is lost, resulting in a non-aromatic compound.

The third condition requires the molecule to be fully conjugated. This means that every single atom in the ring must have an unhybridized p orbital available for overlap. These p orbitals can be part of a double bond (π electrons), an empty orbital (a carbocation), or an orbital containing a lone pair of electrons (a carbanion or a heteroatom like nitrogen or oxygen). In cases involving heteroatoms or charged species, only one lone pair is generally counted toward the π-system, as the atom will adopt sp^2 hybridization to participate in the cyclic conjugation, with the remaining lone pairs (if any) occupying an sp^2 orbital in the plane of the ring.

The fourth and most famous criterion is Hückel's Rule, which dictates the required number of pi electrons. The conjugated ring system must contain $(4n + 2)$ π electrons, where n is any non-negative integer (n = 0, 1, 2, 3, dots). This formula yields the "magic numbers" for aromaticity: 2, 6, 10, 14, 18, and so on. For benzene, with 6π electrons, n=1, satisfying the rule. Other simple aromatic examples include the cyclopropenyl cation (2π electrons, n=0) and the cyclopentadienyl anion (6π electrons, n=1), which owes its unusual stability and ease of formation directly to its aromatic character.

Hückel's $4n + 2$ rule is not an arbitrary number but a direct consequence of Molecular Orbital (MO) Theory, which explains the electronic structure of these ring systems. In cyclic conjugated systems, the relative energies of the p orbitals combine to form a specific pattern of molecular orbitals. When drawing the MO diagram for a cyclic system (often visualized using the Frost circle method), the orbitals are arranged such that a single, lowest-energy bonding orbital exists, followed by pairs of degenerate (equal energy) bonding orbitals. A system is electronically stable when all bonding molecular orbitals are completely filled with paired electrons, leaving the higher-energy non-bonding and antibonding orbitals empty. The $4n+2$ electron count perfectly fills this stable shell configuration: two electrons fill the lowest orbital, and 4n electrons fill the n subsequent pairs of degenerate bonding orbitals.

The absence of aromatic stability is just as important as its presence. Molecules that meet the first three criteria (cyclic, planar, fully conjugated) but instead contain $4n\pi$ electrons (e.g., 4, 8, 12, etc.) are known as antiaromatic. These compounds exhibit the opposite of enhanced stability; they are unusually unstable and highly reactive. In MO theory, a 4n electron count results in a partially filled pair of degenerate non-bonding or low-energy bonding orbitals, often leading to a triplet state (diradical character) according to Hund's rule. This electronic arrangement results in severe destabilization. The prototypical antiaromatic compound is cyclobutadiene (C_4H_4), which has 4π electrons (4n for n=1). Its instability is so profound that it cannot be isolated under normal conditions and quickly reacts with itself or distorts its geometry to avoid the antiaromatic state, transforming from a square to a non-planar rectangle.

A molecule that avoids antiaromaticity by adopting a non-planar conformation is classified as non-aromatic. For instance, cyclooctatetraene (C_8H_8) has 8π electrons, which fits the 4n rule (n=2). If it were planar, it would be highly unstable and antiaromatic. Instead, it adopts a non-planar tub conformation, which breaks the continuous p-orbital overlap. By sacrificing planarity, it loses the conjugation and thus avoids the energetic penalty of antiaromaticity, behaving simply as a reactive polyene, a fate much more stable than its potential antiaromatic state.

Aromaticity is the pinnacle of cyclic conjugated stability, conferring unique chemical properties, such as a strong preference for substitution over addition reactions. This concept extends beyond simple hydrocarbons to heterocyclic compounds (rings containing atoms like N, O, or S) such as pyridine and pyrrole, and is a cornerstone in biochemistry, where aromatic rings form the basis of all nucleic acids (DNA/RNA bases) and many amino acids, highlighting its essential role in life itself.
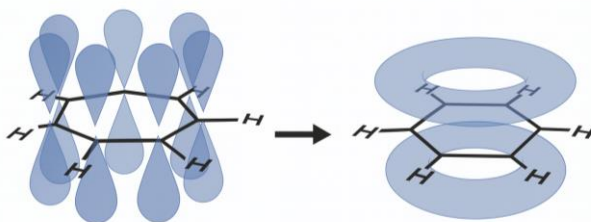

Figure 1. P orbital everlapping illustrating Benzene's aromaticity

Aromaticity in heteroaromatic compounds arises when a ring system containing at least one heteroatom—commonly nitrogen, oxygen, or sulfur—possesses a cyclic, planar, fully conjugated π-electron system that satisfies Hückel's rule, containing 4n+2π electrons. The presence of heteroatoms introduces unique electronic effects because their lone pairs can either participate in the aromatic π system or remain localized, depending on hybridization, electronegativity, and the structure of the ring. When a heteroatom contributes a lone pair to the π system, the overall electron distribution becomes more complex yet still delocalized, granting the ring aromatic stabilization comparable to or sometimes greater than that of benzene. Pyrrole, for example, incorporates a nitrogen lone pair into the aromatic sextet, resulting in an electron-rich aromatic system. In contrast, pyridine maintains its nitrogen lone pair in an sp^2 orbital orthogonal to the aromatic π cloud, so it does not contribute to aromaticity but instead increases the ring's electron-withdrawing character. Despite these differences, both structures remain aromatic because they each maintain a continuous cyclic overlap of p orbitals containing six π electrons.

The heteroatoms profoundly influence the reactivity of heteroaromatic systems. Electron-rich rings such as pyrrole, furan, and thiophene are more reactive toward electrophilic aromatic substitution than benzene, though their reactivity decreases in the order pyrrole > furan > thiophene because the heteroatom's electronegativity affects the stability of the aromatic system. In these rings, the involvement of the heteroatom's lone pair in aromaticity makes electrophilic attack more disruptive to aromatic stabilization, so reactions tend to occur under milder conditions and preferentially at positions that best preserve delocalization. Electron-poor heteroaromatics, such as pyridine, display the opposite behavior: they are relatively resistant to electrophiles but readily undergo nucleophilic aromatic substitution, often at positions dictated by the electron-deficient nature of the ring. Aromaticity also influences basicity, acidity, and coordination behavior. A heteroatom whose lone pair does not participate in aromaticity, as in pyridine, is available to act as a Lewis base, while heteroatoms whose lone pairs form part of the aromatic sextet, as in pyrrole, exhibit diminished basicity.

Overall, heteroaromatic compounds maintain the defining characteristics of aromaticity while displaying reactivity patterns distinct from carbocyclic

aromatics. The interplay between heteroatom lone pairs, conjugation, and ring structure creates a diverse class of aromatic molecules essential in natural products, pharmaceuticals, catalysts, and materials science, where their stability and tunable electronic properties make them chemically versatile and functionally significant. An example for heteroaromatic compounds may be pyridine (Figure 2). One should note that the lone pair electrons on nitrogen atom do not contribute aromaticity since they are directing on the same plane with the main ring. On the other hand, the p electrons of the aza unit are parallel with the other p orbitals forming a full conjugated system (thus, aromatic).

The current study presents theoretical findings on how introducing centrally located triaza units influences the aromaticity of the parent anthracene framework. It also examines how different substituent types and their positions affect the properties of triaza-derivatives, using NICS analysis and electronic energy calculations to evaluate these effects.
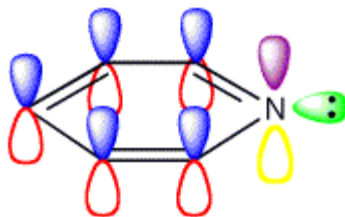
Figure 2. Pyridine's aromaticity

2. METHOD OF CALCULATION

All molecular structures were first subjected to preliminary geometry optimizations to locate energy minima using the semi-empirical PM3 self-consistent field molecular orbital (SCF MO) method at the restricted level. Subsequently, further geometry optimizations were carried out using density functional theory (DFT) with the B3LYP functional and the 6-31G(d,p) basis set, without imposing any symmetry restrictions. In the B3LYP approach, the exchange component combines hybrid Hartree–Fock and local spin density (LSD) exchange terms, supplemented by Becke's gradient correction to LSD exchange. Its correlation component incorporates the Vosko–Wilk–Nusair (VWN3) local correlation functional alongside the Lee–Yang–Parr (LYP)

correlation correction functional. Compared to SCF-HF calculations, the BLYP method provides a significant improvement, offering predictions that are in good qualitative agreement with experimental data.

Normal mode analyses of the optimized structures revealed no imaginary frequencies for the 3N–6 vibrational modes (where N represents the number of atoms), confirming that each optimized geometry corresponds to at least a local minimum on the potential energy surface. Absolute NMR shielding values were computed using the Gauge-Independent Atomic Orbital (GIAO) method within a restricted closed-shell framework, employing the 6-31G(d,p) basis set and based on geometries optimized at the B3LYP/6-31G(d,p) level. NICS values were obtained by calculating the absolute NMR shielding at the ring centers, NICS(0). All geometry optimizations and NICS computations for the studied systems were carried out using the Gaussian 16 software package.

3. RESULTS AND DISCUSSION

Nucleus-Independent Chemical Shift (NICS) has become one of the most influential and widely used computational tools for assessing aromaticity, offering a quantitative and conceptually intuitive measure of magnetic response in cyclic π-electron systems. Aromaticity itself is a multifaceted concept that goes beyond simple structural or energetic criteria. It encompasses the stabilization associated with cyclic electron delocalization, the ability of certain rings to sustain ring currents when placed in a magnetic field, and the characteristic magnetic shielding effects that arise from these currents. Traditional descriptors such as bond lengths, resonance energies, and reactivity trends have long been used to infer aromatic behavior, but each method captures only a single dimension of a phenomenon that is inherently multidimensional. NICS emerged as a powerful solution, providing both a magnetic and electronic signature that reflects the full extent of induced ring currents. Because it relies directly on magnetic shielding values computed at selected points near the ring of interest, NICS offers a simple yet sensitive parameter capable of distinguishing aromatic, antiaromatic, and nonaromatic systems with remarkable clarity.

The method is rooted in the magnetic response of a molecule to an external field. Aromatic rings, according to classical explanations such as the ring-current model, generate a diatropic (shielding) current under an applied

magnetic field. This results in negative magnetic shielding values at the center of the ring, which NICS measures computationally. Antiaromatic systems, by contrast, produce paratropic (deshielding) currents, yielding positive NICS readings. Nonaromatic rings, lacking delocalized π currents, typically show values near zero. Because these numerical results correspond directly to experimentally recognizable magnetic effects, such as those observed in NMR spectroscopy, NICS forms a strong conceptual bridge between theory and experiment. Its quantitative nature has made it indispensable for studying aromaticity across traditional aromatic hydrocarbons, heteroaromatics, metallacycles, inorganic rings, and even excited-state aromaticity, where magnetic criteria offer insight unavailable from purely energetic or structural approaches.

NICS analysis is especially valued for its versatility. The earliest implementations used NICS(0), calculated at the geometric center of a ring. However, later studies revealed that σ-electrons could contribute substantially to the shielding at this location, sometimes obscuring pure π-effects. This issue motivated the introduction of NICS(1), computed 1 Å above or below the ring plane, and eventually the refinement of tensor-based approaches that focus specifically on the out-of-plane component, NICS(1)_zz. These variations allow researchers to selectively probe π-electron delocalization while minimizing σ-interference, producing measurements that correlate strongly with aromatic stabilization. Likewise, grid-based NICS scans across a ring or along an axis perpendicular to it help visualize how magnetic response varies through space, enabling detailed mapping of aromatic and antiaromatic regions. Such improvements have transformed NICS from a single numerical index into a family of complementary tools that together provide a comprehensive magnetic description of aromaticity.

The conceptual strength of NICS also lies in its ability to compare aromaticity across structurally diverse systems on a consistent scale. While energetic and structural criteria may vary significantly with molecular size, substituent effects, or heteroatom identity, magnetic shielding values remain inherently comparable. This has facilitated systematic studies of how electron-withdrawing or electron-donating groups influence ring currents, how heteroatoms modulate delocalization, and how substitution patterns affect the distribution of aromaticity across polycyclic systems. NICS has been crucial in

interpreting aromaticity trends in aza- and triaza-derivatives of polycyclic aromatics, boron- and nitrogen-doped nanographenes, organometallic clusters, Möbius aromatic systems, and other frameworks where conventional aromaticity rules offer incomplete predictions. Its sensitivity to changes in electron density, hybridization, and molecular topology allows researchers to rationalize why certain rings within a fused system remain aromatic while others lose delocalization or become antiaromatic.

Although no single aromaticity descriptor is universally definitive, NICS is regarded as one of the most direct reflections of the physical consequences of aromatic electron delocalization. Its foundation in magnetic properties provides independence from geometric distortions or complex resonance structures. Moreover, because NICS calculations are computationally straightforward and compatible with density functional theory, the method is accessible for molecules of varying sizes and complexities. When interpreted carefully—especially through modern refinements such as $NICS(1)\_zz$ and NICS scans—its results consistently align with chemical intuition and experimental observations. As a result, NICS has become a standard tool in computational chemistry and molecular design, providing insights into aromatic behavior that influence synthetic strategies, stability predictions, and the design of functional materials.

In summary, NICS plays a central role in modern aromaticity analysis by offering a magnetic, quantitative, and conceptually coherent measure of cyclic electron delocalization. Through its evolution into a multifaceted suite of magnetic criteria, it allows researchers to dissect aromaticity in systems where classical approaches fall short. Its capacity to reveal subtle electronic effects, distinguish different types of aromaticity, and provide a consistent reference scale across diverse molecular families ensures its continued importance in theoretical and applied chemistry.

Together with NICS, The Harmonic Oscillator Model of Aromaticity (HOMA) is crucial for providing a quantitative and geometrically based measure of aromaticity. Unlike traditional methods that rely on electron count or resonance structures, HOMA directly correlates aromaticity with bond length deviations from an idealized aromatic structure, making it a more objective and reliable tool. Its ability to assess aromaticity in a wide range of systems, including non-planar or distorted molecules, has made it invaluable in

computational chemistry for studying the stability, reactivity, and properties of aromatic compounds, including transition metal complexes and polycyclic aromatic hydrocarbons.

Structures

In Figure 3, all possible triazaanthracene derivatives have been shown. The introduction of one or more heteroatoms into the rings of an aromatic system, or the replacement of ring hydrogen atoms with heteroatoms or heteroatomic groups, has long been a subject of interest in both theoretical and experimental research. In this study, all possible triazaanthracene isomers and their substituted derivatives (NO_2) were examined theoretically using the B3LYP/6-31G(d,p) level of theory to evaluate their stability and aromatic character. Mono- or dicyclic perturbations at ring-fusion positions were not considered, as such modifications lead to non-aromatic structures (Figure 3). In Figure 4 geometry optimized structures of 1,2,3-triazaanthracene and 1,2,4-triazaanthracene are given.
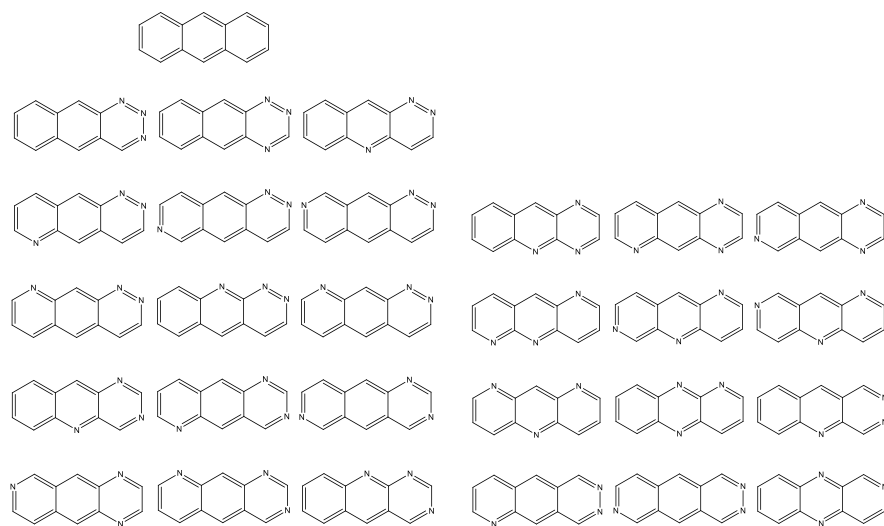
Figure 3. Structures of the triaza derivatives under study.
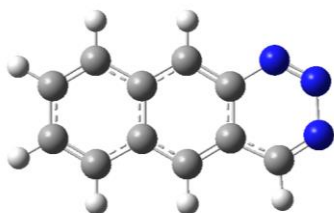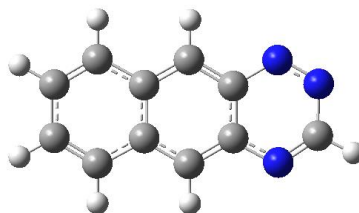
1,2,3-triazaanthracene   **1,2,4- triazaanthracene**

Figure 4. Geometry optimized structures of 1,2,3- triazaanthracene and 1,2,4-triazaanthracene

Energetics

The graph in Figure 6 illustrates the relative energies of all possible triazaanthracene derivatives, allowing comparison of their thermodynamic stabilities based on the positions of the three nitrogen atoms within the anthracene framework. Structures on the left side of the plot (such as the 1,2,3-type arrangements) display higher energies, indicating lower stability. As the substitution pattern progresses along the x-axis, there is a noticeable drop in energy, with several structures forming a cluster around the lowest energy region near –580.70. These minima correspond to the most stable triazaanthracene isomers, suggesting that certain nitrogen placement patterns—likely those that distribute electron density more evenly and minimize ring strain—are energetically favored. Toward the right side of the plot, the energies rise again, reflecting substitution patterns that destabilize the π-system. The overall trend indicates that the aromatic framework is highly sensitive to the specific arrangement of nitrogen atoms, and only a subset of triaza arrangements leads to significantly stabilized electronic structures.
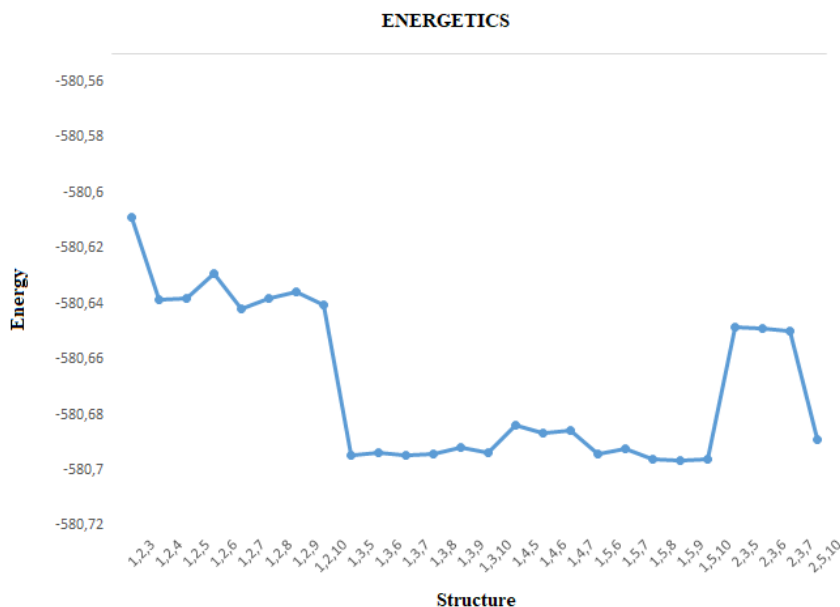
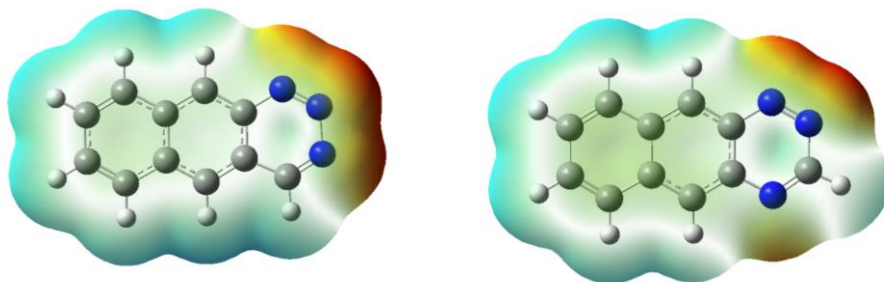**Figure 5.** Relative energies of compounds of the series

Figure 6. Three-Dimensional electrostatic maps of structures of 1,2,3-triazaanthracene and 1,2,4-triazaanthracene

Figure 6 presents a molecular electrostatic potential (MEP) maps of the heteroaromatic polycyclic systems in which three nitrogen atoms are incorporated into one of the rings. The colored surface surrounding the molecule visualizes the distribution of electron density, with red and orange regions indicating areas of higher electron density and negative potential, while blue and green areas represent more electron-deficient, positive potential regions. The presence of the three electronegative nitrogen atoms creates localized zones of increased electron density near their positions, influencing

the overall electronic structure of the aromatic framework. This distribution highlights how heteroatom substitution modifies the reactivity pattern of the molecule, signaling where electrophilic or nucleophilic interactions are most likely to occur due to shifts in electron delocalization within the aromatic system.

NICS

Stanger outlines the main conceptual frameworks used to define aromaticity and highlights the inconsistencies and paradoxes that arise both among these frameworks and among the various aromaticity indices used to evaluate them (42).

The ability of a ring to allow a specific number of π-electrons to delocalize smoothly contributes to its aromatic character and enhances its stability. NICS provides a way to assess this aromaticity by evaluating the magnetic response of the ring system.

Benzene is the classic example of an aromatic molecule, exhibiting complete delocalization of six π-electrons. When a heteroatom replaces a carbon at the center of an aromatic ring, the resulting electronegativity differences disrupt this delocalization and reduce the ring's aromaticity. Introducing a second or third heteroatom(s), as in the systems studied here, diminishes the aromatic character even further. The NICS values for unsubstituted anthracene and its triaza-substituted derivatives are presented in Table 1 and align with these expectations. A, B and C dinote the aromatic rings of the anthracene molecule (Table 1). Nitrogen substitution at the centric positions of the ring lowers its aromaticity, and in the triaza derivatives the ring's NICS values fall from −9.0 ppm to −1.7 ppm for the 1,2,3-isomer and −2.5 ppm for the 1,2,4-isomer. In comparison, the central ring of anthracene typically shows a NICS value of about −12.7 ppm, indicating greater aromaticity than the outer rings. After substitution, this value drops to −8.8 ppm for the one aza derivative and −7.8 ppm for the 5,10-diaza derivative.

Table 1. Calculated NICS data for the present systems.

Structures	A	B	C
Anthracene	9.0	12.7	9.0
1,2,3	1.7	12.4	9.0
1,2,4	2.5	12.5	9.0
1,2,5	6.3	9.1	9.0
1,2,6	6.2	11.4	7.2
1,2,7	6.3	11.5	7.1
1,2,8	6.4	11.9	7.1
1,2,9	6.2	11.8	7.2
1,2,10	6.3	8.8	9.1
1,3,5	6.0	8.8	9.1
1,3,6	6.1	12.4	7.0
1,3,7	6.0	12.4	7.1
1,3,8	6.0	12.5	7.2
1,3,9	6.1	12.4	7.1
1,3,10	6.1	8.9	9.1
1,4,5	5.7	8.9	9.0
1,4,6	5.8	12.3	7.2
1,4,7	5.7	12.4	7.1
1,5,6	7.2	8.8	7.1
1,5,7	7.2	8.7	7.0
1,5,8	7.3	8.7	7.1
1,5,9	7.2	8.8	7.1
1,5,10	7.2	7.8	9.1
2,3,5	4.4	9.0	9.1
2,3,6	4.4	12.0	7.0
2,3,7	4.4	12.3	6.9
2,5,10	7.1	7.9	9.0

However, this reduction in aromaticity can be partially restored by replacing ring hydrogens with an electronegative atom or group. A strongly electron-withdrawing substituent can draw electron density from the heteroatom on the central ring back toward the ring system, thereby enhancing its aromatic character.

HOMA

The Harmonic Oscillator Model of Aromaticity (HOMA) is a widely used computational approach to quantify aromaticity in cyclic conjugated molecules, offering a more objective and systematic measure of aromatic character compared to traditional methods based on electron count or resonance structures. The HOMA method, introduced by Kruszewski and Cyranó in 1993, is rooted in the concept that the delocalized π-electron system in an aromatic molecule behaves similarly to a harmonic oscillator, where the bond lengths in the conjugated ring exhibit specific oscillatory behavior in relation to the ideal bond length corresponding to a perfectly aromatic system. The HOMA index quantifies aromaticity by comparing the calculated bond lengths in a given molecule to those of a hypothetical perfectly aromatic molecule, assuming an idealized geometry with uniformly delocalized π-electrons. Specifically, the HOMA value is derived from the deviation of the bond lengths from this ideal geometry, with smaller deviations indicating stronger aromaticity and larger deviations signifying weaker aromaticity or antiaromaticity. The formula for HOMA is expressed as a weighted sum of these bond length deviations, which is then scaled to yield a value between 0 (for a completely non-aromatic system) and 1 (for a perfectly aromatic system). This bond-length-based measure is particularly advantageous because it directly correlates to the physical geometry of the molecule, which is inherently influenced by the delocalization of electrons, and thus reflects the structural consequences of aromaticity in a way that is not purely dependent on electron count or resonance effects alone. Moreover, HOMA is versatile and applicable to a wide range of molecules, including those that deviate from traditional aromaticity models, such as non-planar systems or polycyclic aromatic hydrocarbons (PAHs) with distorted geometries. Unlike some other aromaticity indices that focus on electronic properties such as electron density or molecular orbital theory, HOMA offers a more geometrically intuitive measure that can be easily integrated into

computational studies, making it a valuable tool in the exploration of aromaticity in complex organic and inorganic systems. The method has been particularly useful in assessing the aromaticity of transition metal complexes, large conjugated molecules, and systems where traditional criteria such as the Hückel rule may not be sufficient or applicable. Additionally, HOMA has been applied to study the impact of substituents or structural modifications on the aromatic character of molecules, providing insight into how perturbations to the conjugated system can affect the overall aromaticity. Overall, the HOMA index provides a robust, reliable, and computationally accessible approach to understanding aromaticity, offering a more nuanced and quantitative alternative to classical rules based on electron count and resonance stabilization. Its widespread use in both academic research and practical applications underscores its importance as a key tool in the modern chemist's toolkit for the study of aromatic compounds and their behavior in chemical reactions, materials science, and molecular design.

Table 2. Calculated HOMA data for the present systems.

Structures	A	B	C
Anthracene	0.950	0.982	0.950
1,2,3	0.127	0.981	0.952
1,2,4	0.225	0.981	0.952
1,2,5	0.783	0.950	0.950
1,2,6	0.782	0.965	0.863
1,2,7	0.783	0.965	0.864
1,2,8	0.781	0.965	0.864
1,2,9	0.781	0.965	0.863
1,2,10	0.782	0.950	0.950
1,3,5	0.783	0.950	0.951
1,3,6	0.782	0.981	0.862
1,3,7	0.783	0.981	0.864
1,3,8	0.783	0.981	0.864
1,3,9	0.783	0.981	0.862
1,3,10	0.782	0.950	0.950
1,4,5	0.761	0.950	0.951
1,4,6	0.760	0.981	0.863
1,4,7	0.761	0.982	0.864
1,5,6	0.864	0.950	0.866
1,5,7	0.863	0.952	0.862
1,5,8	0.861	0.950	0.864
1,5,9	0.864	0.950	0.864
1,5,10	0.864	0.897	0.952
2,3,5	0.551	0.950	0.950
2,3,6	0.550	0.981	0.864
2,3,7	0.551	0.981	0.852
2,5,10	0.864	0.898	0.950

According to the data obtained from HOMA aromaticity calculations we observed the disturbance of the aromaticity upon centric substitution of nitrogen atoms.

4. CONCLUSION

In conclusion, the substitution of a nitrogen atom into the anthracene molecule significantly impacts its aromaticity, as evidenced by both the Nuclear Independent Chemical Shift (NICS) and the Harmonic Oscillator Model of Aromaticity (HOMA) data. NICS calculations show a noticeable reduction in the aromatic character of the substituted anthracene, with the nitrogen atom disrupting the electron delocalization across the conjugated π-system, as reflected in a less negative NICS value compared to the parent molecule. This suggests a weakening of the aromatic stabilization due to the electron-withdrawing nature of nitrogen, which disturbs the idealized delocalized π-electron cloud. Similarly, the HOMA index also reveals a decrease in aromaticity, with bond length deviations from the ideal aromatic geometry becoming more pronounced in the nitrogen-substituted system. The increase in these deviations further supports the notion that nitrogen substitution reduces the planarity and delocalization of the π-electrons, weakening the overall aromaticity of the molecule. Thus, both NICS and HOMA data consistently demonstrate that nitrogen substitution on anthracene leads to a decrease in its aromatic stability, offering a more comprehensive understanding of how heteroatom incorporation affects the electronic properties of aromatic systems.

REFERENCES

1. Becke, A. D. (1988). Density-functional exchange-energy approximation with correct asymptotic behavior. *Physical Review A, 38*(6), 3098-3100. https://doi.org/10.1103/PhysRevA.38.3098

2. Brogli, F., Heilbronner, E., & Kobayashi, T. (1972). Photoelectron spectra of azabenzenes and azanaphthalenes, II. A reinvestigation of azanaphthalenes by high-resolution photoelectron spectroscopy. *Helvetica Chimica Acta, 55*, 274-288. https://doi.org/10.1002/hlca.19720550131

3. Cyranski, M. K., Krygowski, T. M., Katritzky, A. R., & Schleyer, P. R. (2002). To what extent can aromaticity be defined uniquely? *Journal of Organic Chemistry, 67*(4), 1333-1338. https://doi.org/10.1021/jo016255s

4. Frisch, M. J., Trucks, G. W., Schlegel, H. B., Scuseria, G. E., Robb, M. A., Cheeseman, J. R., Scalmani, G., Barone, V., Petersson, G. A., Nakatsuji, H., Li, X., Caricato, M., Marenich, A. V., Bloino, J., Janesko, B. G., Gomperts, R., Mennucci, B., Hratchian, H. P., Ortiz, J. V., Izmaylov, A. F., Sonnenberg, J. L., Williams-Young, D., Ding, F., Lipparini, F., Egidi, F., Goings, J., Peng, B., Petrone, A., Henderson, T., Ranasinghe, D., Zakrzewski, V. G., Gao, J., Rega, N., Zheng, G., Liang, W., Hada, M., Ehara, M., Toyota, K., Fukuda, R., Hasegawa, J., Ishida, M., Nakajima, T., Honda, Y., Kitao, O., Nakai, H., Vreven, T., Throssell, K., Montgomery, Jr., J. A., Peralta, J. E., Ogliaro, F., Bearpark, M. J., Heyd, J. J., Brothers, E. N., Kudin, K. N., Staroverov, V. N., Keith, T. A., Kobayashi, R., Normand, J., Raghavachari, K., Rendell, A. P., Burant, J. C., Iyengar, S. S., Tomasi, J., Cossi, M., Millam, J. M., Klene, M., Adamo, C., Cammi, R., Ochterski, J. W., Martin, R. L., Morokuma, K., Farkas, O., Foresman, J. B., & Fox, D.J. (2016) Gaussian, Inc., Wallingford CT.

5. Ghiasi, R. (2005). The mono- and di-silanaphthalene: Structure, properties, and aromaticity. *Journal of Molecular Structure (Theochem), 718*, 225-233. https://doi.org/10.1016/j.theochem.2004.11.038

6. Glukhovtsev, M. N. (1997). Aromaticity today: Energetic and structural criteria. *Journal of Chemical Education, 74*(2), 132-136. https://doi.org/10.1021/ed074p132

7. Gümüş, S. (2011). The aromaticity of substituted diazanaphthalenes. *Computational Theoretical Chemistry, 963*, 263-267. https://doi.org/10.1016/j.comptc.2010.10.026

8. Gümüş, S. (2011). A computational study on substituted diazabenzenes. *Turkish Journal of Chemistry, 35*(6), 803-808.

9. Hehre, W. J., Radom, L., Schleyer, P. R., & Pople, J. A. (1986). *Ab Initio Molecular Orbital Theory.* Wiley, New York.

10. Heinis, T., Chowdhury, S., & Kebarle, P. (1993). Electron affinities of naphthalene, anthracene, and substituted naphthalenes and anthracenes. *Organomass Spectrometry, 28*(4), 358-365. https://doi.org/10.1002/oms.1210280416

11. Jiao, H., & Schleyer, P. R. (1998). Aromaticity of pericyclic reaction transition structures: Magnetic evidence. *Journal of Physical Organic Chemistry, 111*(8-9), 655-662. https://doi.org/10.1002/(SICI)1099-1395(199808/09)11:8/9<655::AID-POC66>3.3.CO;2-

12. Kaim, W., Tesmann, H., & Bock, H. (1980). Me3C-, Me3Si-, Me3Ge-, Me3Sn- and Me3Pb-substituted benzol- and naphthalene derivatives and their radical anions. *Chemische Berichte, 113*, 3221-3234. https://doi.org/10.1002/cber.19801131010

13. Kitagawa, T. (1968). Stark spectroscopy of molecular crystals. *Journal of Molecular Spectroscopy, 26*, 1-23. https://doi.org/10.1016/0022-2852(68)90139-2

14. Klasinc, L., Kovac, B., & Gusten, H. (1983). Photoelectron spectra of acenes. Electronic structure and substituent effects. *Pure and Applied Chemistry, 55*(2), 289-298. https://doi.org/10.1351/pac198855020289

15. Kohn, W., & Sham, L. J. (1965). Self-consistent equations including exchange and correlation effects. *Physical Review, 140*(A1133-A1138). https://doi.org/10.1103/PhysRev.140.A1133

16. Krygowski, T. M., Cyranski, M. K., Czarnocki, Z., Hafelinger, G., & Katritzky, A. R. (2000). Aromaticity: A theoretical concept of immense practical importance. *Tetrahedron, 56*(10), 1783-1796. https://doi.org/10.1016/S0040-4020(99)00979-5

17. Lardin, H. A., Squires, R. R., & Wenthold, P. G. (2001). Determination of the electron affinities of alpha- and beta-naphthyl radicals using the kinetic method with full entropy analysis. *Journal of Mass Spectrometry, 36*(7), 607-615. https://doi.org/10.1002/jms.159

18. Lee, C., Yang, W., & Parr, R. G. (1988). Development of the Colle-Salvetti correlation-energy formula into a functional of the electron density. *Physical Review B, 37*, 785-789. https://doi.org/10.1103/PhysRevB.37.785

19. Meot-Ner, M., Liebman, J. F., & Kafafi, S. A. (1988). Ionic probes of aromaticity in annelated rings. *Journal of the American Chemical Society, 110*(16), 5937-5941. https://doi.org/10.1021/ja00226a001

20. Minkin, V. I., Glukhovtsev, M. N., & Simkin, B. Y. (1994). *Aromaticity and Antiaromaticity: Electronic and Structural Aspects.* Wiley, New York.

21. Parr, R. G., & Yang, W. (1989). *Density Functional Theory of Atoms and Molecules.* Oxford University Press, London.

22. Patchkovskii, S., & Thiel, W. (2002). Nucleus-independent chemical shifts from semiempirical calculations. *Journal of Molecular Modeling, 6*, 67-75. https://doi.org/10.1007/PL00010736

23. Pulay, P., Hinton, J. F., & Wolinski, K. (1993). Nuclear magnetic shieldings and molecular structure. In J. A. Tossel (Ed.), *NATO ASI Series C, vol. 386* (pp. 243-268). Kluwer, The Netherlands.

24. Quinonero, D., Garau, C., Frontera, A., Ballester, P., Costa, A., Deya, P. M. (2002). Quantification of aromaticity in oxocarbons: The problem of the fictitious "nonaromatic" reference system. *Chemistry - A European Journal, 8*(2), 433-438. https://doi.org/10.1002/1521-3765(20020118)8:2<433::AID-CHEM433>3.3.CO;2-K

25. Schafer, W., Schweig, A., Markl, G., & Heier, K. H. (1973). Zur elektronenstruktur der λ3- und λ5-phosphanaphthaline - ungewöhnlich grosse Modestabilisierungen. *Tetrahedron Letters, 3743-3746*. https://doi.org/10.1016/S0040-4039(01)87025-8

26. Schafer, W., Schweig, A., Vermeer, H., Bickelhaupt, F., & Graaf, H. D. (1975). On the nature of the "free electron pair" on phosphorus in aromatic phosphorus compounds: The photoelectron spectrum of 2-

phosphanaphthalene. *Journal of Electron Spectroscopy and Related Phenomena, 6*, 91-98. https://doi.org/10.1016/0368-2048(75)80001-6

27. Schiedt, J., Knott, W. J., Barbu, K. L., Schlag, E. W., & Weinkauf, R. (2000). Microsolvation of similar-sized aromatic molecules: Photoelectron spectroscopy of bithiophene, azulene, and naphthalene-water anion clusters. *Journal of Chemical Physics, 113*, 9470-9478. https://doi.org/10.1063/1.1319874

28. Schleyer, P. R. (2001). Introduction: Aromaticity. *Chemical Reviews, 101*(4), 1115-1118. https://doi.org/10.1021/cr0103221

29. Schleyer, P. R., & Jiao, H. (1996). What is aromaticity? *Pure and Applied Chemistry, 68*(2), 209-218. https://doi.org/10.1351/pac199668020209

CHAPTER 3

THE ROLE OF PALEOCLIMATE RECONSTRUCTIONS IN ASSESSING CLIMATE MODEL ACCURACY

Assist. Prof. Dr. Ayşegül Feray GÖKDERE[1]

[1] Van Yüzüncü Yıl University, Faculty of Engineering, Department of Geological Engineering, Van, Turkey.ORCID: 0000-0002-3842-1711

INTRODUCTION

Numerical climate models are the primary tools used to simulate past, present and future climate and to inform mitigation and adaptation policy. Their credibility depends on how well they reproduce the observed behaviour of the climate system at a range of spatial and temporal scales. Traditionally, model evaluation has relied heavily on the instrumental era, roughly the last 150 years, for which relatively dense global observations of surface temperature, precipitation and circulation exist (Flato et al., 2013; IPCC, 2013). Although indispensable, this time window is short compared with many key components of the climate system and samples only a limited range of external forcing and climate states (IPCC, 2021).

Earth's climate history, by contrast, includes large natural perturbations such as glacial–interglacial cycles, orbitally driven monsoon changes and past warm periods with atmospheric CO_2 concentrations comparable to or higher than those expected in coming centuries. These episodes provide natural experiments to test models under boundary conditions very different from the present. Information about such climates comes from paleoclimate reconstructions based on indirect "proxy" indicators preserved in archives such as ice cores, marine and lake sediments, corals, tree rings and speleothems (Jansen et al., 2007; IPCC, 2013).

Over the past two decades, the climate modelling and paleoclimate communities have increasingly worked together to exploit these records for model evaluation. Coordinated intercomparison projects, particularly the Paleoclimate Modelling Intercomparison Project (PMIP), have produced standardized simulations of past key intervals with the same models that are used in the Coupled Model Intercomparison Projects (CMIP) for future projections (Braconnot et al., 2012; Kageyama et al., 2018). At the same time, large multi proxy syntheses and advanced reconstruction methods, including proxy system modelling and paleoclimate data assimilation, have generated gridded reconstructions of past climate fields that can be compared directly with model output (Steiger et al., 2017; Tierney et al., 2023).

This chapter examines why paleoclimate reconstructions are essential for assessing climate model accuracy. It outlines the limitations of relying solely on the instrumental record, describes the main paleoclimate archives and reconstruction approaches, reviews frameworks for model–data comparison,

and highlights how specific paleoclimate intervals have been used to test and refine models. Particular emphasis is placed on the role of paleoclimate constraints in narrowing estimates of climate sensitivity and improving the physical realism of models used for future projections (Tierney et al., 2020a; IPCC, 2021; Lunt et al., 2024).

2. CLIMATE MODELS AND THE LIMITS OF THE INSTRUMENTAL RECORD

State of the art global climate models solve the fundamental equations of fluid dynamics and thermodynamics on a rotating sphere, coupled to parameterizations of clouds, convection, radiation, land–surface processes and sea ice (Flato et al., 2013). Earth System Models extend this framework by including interactive biogeochemical cycles and aerosols. Despite their complexity, these models must represent processes occurring on scales smaller than the model grid through parameterizations that involve uncertain empirical coefficients. Such parameters are tuned so that the model reproduces selected features of the observed climate, such as global mean temperature, large scale circulation patterns and top of atmosphere radiation balance (Flato et al., 2013; IPCC, 2013).

As a consequence, model performance is often judged by how well simulations reproduce the mean state and variability over the twentieth and early twenty first centuries. However, this period samples a relatively modest radiative forcing: the observed global mean surface warming of about 1.1 °C since the late nineteenth century is associated with an anthropogenic radiative forcing that is smaller than the forcing expected under many future emission scenarios (IPCC, 2021). Feedbacks that operate more strongly under larger perturbations, such as some cloud and ice sheet feedbacks, cannot be fully constrained from the historical record alone. Moreover, internal climate variability on multidecadal to centennial timescales can mask or amplify the forced response in the instrumental record, complicating attempts to infer climate sensitivity from recent observations (IPCC, 2021).

The instrumental record is also too short to fully test slow components of the climate system, such as large ice sheets, deep ocean circulation and long term carbon cycle feedbacks. These components may strongly influence the long term response to sustained greenhouse gas forcing, but their adjustment

timescales are centuries to millennia. Testing model representations of such processes therefore requires information from earlier climates that approached quasi equilibrium under very different boundary conditions. Paleoclimate reconstructions provide exactly this information, and thus offer an indispensable complement to instrumental era model evaluation (Jansen et al., 2007; IPCC, 2013; Tierney et al., 2020a).

3. PALEOCLIMATE ARCHIVES AND RECONSTRUCTION METHODS

Paleoclimate information is derived from proxy indicators, which are measurable physical, chemical or biological properties that respond in a systematic way to climate variables. Different archives sample different parts of the climate system and span different temporal and spatial scales. Ice cores from Greenland and Antarctica, for example, contain stratified layers of snow and firn that preserve stable isotope ratios, trapped greenhouse gases and aerosol concentrations, providing high resolution records of temperature, atmospheric composition and radiative forcing over hundreds of thousands of years (Jansen et al., 2007; IPCC, 2013).

Tree rings offer annual to seasonal resolution over centuries to millennia, particularly in mid latitude regions. Ring width, density and stable isotopes reflect combinations of temperature, moisture and growing season length, and can be calibrated against modern observations to reconstruct past climate variability (IPCC, 2013; Mann et al., 2008; PAGES 2k Consortium, 2013). Corals, especially massive tropical corals, record sea surface temperature and salinity through the geochemistry of their skeletons, allowing reconstructions of past variability in phenomena such as the El Niño–Southern Oscillation. Marine and lacustrine sediments contain microfossil assemblages, biomarker compositions and geochemical ratios that can be translated into sea surface or deep water temperatures, sea ice cover, and hydrological changes on timescales from millennia to millions of years (Jansen et al., 2007; Tierney et al., 2020a). Speleothems (cave carbonates) provide precisely dated records of hydrological changes and, in some settings, temperature through stable isotopes and trace elements, which have been widely used to reconstruct past monsoon variability (IPCC, 2013).

Translating these proxy measurements into quantitative climate reconstructions involves a range of methods. A traditional approach is empirical calibration, in which statistical relationships between proxy values and instrumental climate data are derived for a calibration period and then applied to the older part of the record. This approach underpins many multi proxy temperature reconstructions of the last two millennia, such as those developed by Mann et al. (2008) and the PAGES 2k Consortium (2013), which combine many individual proxy records into hemispheric or global composites. While empirical methods are powerful, they assume that proxy–climate relationships are stationary and often treat proxies as direct measurements of climate variables, neglecting the processes that intervene between climate forcing and proxy formation.

More recently, proxy system modelling (PSM) has sought to address these limitations by explicitly representing the forward chain from climate to proxy, including environmental, biological and geochemical processes (Steiger et al., 2017; Tierney et al., 2023). PSMs simulate proxy values from modelled climate fields, allowing comparisons to be made consistently in proxy space and reducing ambiguities when the proxy does not respond linearly to the target variable. PSMs have been developed for a variety of archives, including tree rings, corals, speleothems and marine microfossils, and are increasingly integrated into model evaluation frameworks (Steiger et al., 2017; Tierney et al., 2023).

In parallel, paleoclimate data assimilation has emerged as a powerful way to merge proxy information with climate model dynamics. In this framework, proxy observations are combined with prior ensembles of climate model simulations using statistical techniques adapted from numerical weather prediction, such as Ensemble Kalman filtering or particle filters (Steiger et al., 2017; Tierney et al., 2023). The result is a time evolving, spatially complete reconstruction that is consistent with both the physics of the model and the information contained in the proxies. Paleoclimate data assimilation has been used, for example, to produce global temperature fields for the Last Glacial Maximum (LGM) and the last deglaciation (Osman et al., 2021; Annan & Hargreaves, 2022), and to reconstruct regional patterns of temperature and circulation from networks of water isotope records (Steiger et al., 2017). These products are particularly well suited for evaluating climate models because they

are expressed in the same variables and spatial grids as model output and come with explicit uncertainty estimates.

4. FRAMEWORKS FOR MODEL–PALEODATA COMPARISON

Paleoclimate reconstructions become especially valuable for model evaluation when combined with coordinated modelling efforts and standardized experimental designs. The Paleoclimate Modelling Intercomparison Project has been central in this regard. Since the 1990s, successive PMIP phases have organized multi model experiments for key intervals such as the LGM (~21 thousand years before present), the mid Holocene (~6 ka), and the last millennium, among others (Braconnot et al., 2012; Kageyama et al., 2018). PMIP4, which is part of CMIP6, explicitly connects paleoclimate simulations with the same models used for historical and future projections, using shared protocols for boundary conditions and forcings (Kageyama et al., 2018).

Model–paleodata comparison in this context goes beyond qualitative checks of whether simulated anomalies "look like" reconstructions. A suite of quantitative metrics is used to evaluate performance. These include pattern correlations and root mean square error between simulated and reconstructed spatial fields, such as sea surface temperature at the LGM or mid Holocene precipitation anomalies in monsoon regions (Braconnot et al., 2012; Brierley et al., 2020). Regional indices, for example monsoon rainfall intensity, sea ice extent or land–sea temperature contrast, offer targeted tests of specific processes. Global mean metrics, such as the magnitude of LGM cooling relative to preindustrial, provide constraints on climate sensitivity and the representation of feedback (Tierney et al., 2020b; Osman et al., 2021; Annan & Hargreaves, 2022).

Paleoclimate experiments have also been used to derive emergent constraints, in which inter model relationships between a simulated quantity and equilibrium climate sensitivity (ECS) or other properties are confronted with paleoclimate data. For example, the relationship between LGM tropical cooling and ECS can be examined across a model ensemble; if proxy based reconstructions favour a particular range of tropical cooling, then the associated range of ECS values can be inferred (Tierney et al., 2020b; IPCC, 2021; Lunt et al., 2024). Similarly, relationships between mid Holocene monsoon changes

and model parameters governing convection or land–atmosphere coupling can be exploited to constrain those parameters using paleodata (Braconnot et al., 2012; Brierley et al., 2020). Such approaches tightly link paleoclimate reconstructions to model calibration.

5. CASE STUDIES: PAST CLIMATES AS TESTS OF MODEL ACCURACY

5.1 The Last Glacial Maximum

The LGM is a cornerstone interval for testing climate models because it is relatively well constrained in terms of radiative forcing and climate response. At this time extensive Northern Hemisphere ice sheets, reduced greenhouse gas concentrations and altered dust and vegetation patterns produced a substantially colder climate than today. Proxy syntheses such as MARGO and more recent compilations of marine and terrestrial data provide global reconstructions of LGM sea surface and surface air temperature, as well as sea ice extent (Tierney et al., 2020b; Osman et al., 2021; Annan & Hargreaves, 2022).

Paleoclimate data assimilation has recently combined these proxy datasets with ensembles of climate model simulations to produce spatially complete temperature fields and probabilistic estimates of global mean cooling. Osman et al. (2021) and Annan and Hargreaves (2022) inferred a global mean LGM cooling of roughly 6 °C relative to preindustrial, larger than many earlier estimates. When LGM simulations from CMIP class models are compared with these reconstructions, they show that some models reproduce the global and regional cooling reasonably well, while others substantially underestimate or overestimate the amplitude of glacial cooling, particularly in the tropics (Tierney et al., 2020b; Osman et al., 2021).

These mismatches have direct implications for model physics and climate sensitivity. For example, early versions of some CMIP6 models with high ECS values simulate very strong LGM cooling that is incompatible with proxy based reconstructions, indicating excessively strong cloud feedbacks (Tierney et al., 2020b; IPCC, 2021). Zhu et al. (2022) used LGM paleoclimate constraints to tune cloud microphysics parameters in CESM2, yielding a "paleoclimate calibrated" configuration with reduced ECS and improved agreement with both LGM and historical climate. This case demonstrates how

paleoclimate reconstructions can guide model development in a physically interpretable way, directly improving the credibility of future projections.

5.2 The Mid Holocene and Monsoon Systems

The mid Holocene, about 6 ka, provides a complementary test of model accuracy, particularly for tropical rainfall and land–atmosphere feedbacks. This interval was characterized by changes in Earth's orbital configuration that enhanced Northern Hemisphere summer insolation, strengthening summer monsoons and shifting tropical rain belts. A wide range of paleohydrological proxies, including lake level records, pollen assemblages and speleothem isotopes, indicate substantially wetter conditions in large parts of North Africa and West Asia, often referred to as the "Green Sahara" (Jansen et al., 2007; IPCC, 2013).

PMIP simulations of the mid Holocene generally reproduce some increase in monsoon rainfall but have historically underestimated both the magnitude and the northward reach of the African monsoon, a discrepancy known as the "monsoon mismatch" (Braconnot et al., 2012; Brierley et al., 2020). Brierley et al. (2020) showed that in PMIP4–CMIP6 simulations some models exhibit improved monsoon responses, but many still fail to match the extent of reconstructed wet conditions, suggesting that vegetation feedbacks, land surface processes and regional circulation changes remain imperfectly represented.

From the perspective of model evaluation, the mid Holocene highlights processes that are also critical for future projections: the sensitivity of tropical rainfall to changes in insolation and sea surface temperature gradients, the role of land surface feedbacks in amplifying or damping monsoon anomalies, and the representation of shifts in the Intertropical Convergence Zone. Improving model performance for the mid Holocene monsoon regime therefore enhances confidence in projections of future monsoon changes under anthropogenic forcing, which have major implications for water resources and food security (IPCC, 2013; IPCC, 2021).

5.3 Common Era and Last Millennium Variability

High resolution reconstructions for the last two millennia offer another rich testbed for climate models. Multiproxy temperature reconstructions, such

as those by Mann et al. (2008) and the PAGES 2k Consortium (2013), document hemispheric scale temperature variations including the Medieval Climate Anomaly, the Little Ice Age and the strong warming of the twentieth century. These reconstructions reveal that preindustrial temperature variability at hemispheric scale was generally smaller in amplitude than recent warming, but with significant regional structure and low frequency variability.

Last millennium simulations conducted within PMIP incorporate estimates of natural external forcing from volcanic eruptions and solar variability, along with reconstructions of land use change and, in some cases, early anthropogenic greenhouse gas emissions (Kageyama et al., 2018; IPCC, 2021). When compared with reconstructions, these simulations generally reproduce the broad features of hemispheric scale temperature evolution, including cooling associated with major volcanic eruptions and the transition from the Little Ice Age to modern warming (Mann et al., 2008; PAGES 2k Consortium, 2013; IPCC, 2021).

However, some analyses suggest that models may underestimate low frequency variability in certain regions or over certain timescales, raising questions about the representation of internal variability and the fidelity of proxy records at those timescales (PAGES 2k Consortium, 2013; IPCC, 2021). Last millennium comparisons have also been used to constrain transient climate response and ECS using energy balance frameworks and detection and attribution methods. For example, Hegerl et al. (2006) combined reconstructions of Northern Hemisphere temperatures for the past seven centuries with forcing estimates to infer that very low climate sensitivity is inconsistent with the amplitude of preindustrial variability. Such studies demonstrate how paleoclimate reconstructions intimately complement instrumental era constraints.

5.4 Warm Climates and Future Analogs

Several past intervals were significantly warmer than the present and thus provide analogs—albeit imperfect ones—for future high CO_2 climates. The mid Pliocene Warm Period (~3–3.3 Ma) is particularly important because atmospheric CO_2 concentrations were similar to those expected later this century under intermediate emission scenarios, and yet the climate system had reached near equilibrium with much smaller ice sheets and higher sea level

(Tierney et al., 2020a; Lunt et al., 2024). Reconstructions indicate strong polar amplification and reduced equator to pole temperature gradients, as well as major changes in precipitation patterns.

When Pliocene climate is simulated with modern ESMs, many models capture the sign of high latitude warming but underestimate its magnitude, hinting at missing or underestimated feedbacks in the model physics, particularly related to clouds and sea ice (Tierney et al., 2020a; Lunt et al., 2024). Comparisons between Pliocene reconstructions and simulations also show that the spatial pattern of warming differs from that in idealized CO_2 doubling experiments, suggesting that "pattern effects" may influence estimates of ECS inferred from paleoclimate data (Tierney et al., 2020a; IPCC, 2021). Deep time greenhouse climates of the early Cenozoic, although more uncertain, also indicate very warm polar regions under high CO_2, reinforcing the conclusion that Earth system sensitivity—including slow feedbacks—may be larger in warm climates than in cooler ones (Tierney et al., 2020a; Lunt et al., 2024).

6. PALEOCLIMATE CONSTRAINTS ON CLIMATE SENSITIVITY

Equilibrium climate sensitivity is a central quantity in climate science because it links radiative forcing to long term global warming. ECS cannot be measured directly; instead, it is inferred from multiple lines of evidence: physical process understanding, emergent constraints within model ensembles, historical observations and paleoclimate data (IPCC, 2021). Paleoclimate intervals with well constrained forcings and temperature responses provide crucial tests because they extend the range of climate states beyond the modern and sample feedbacks that only become active under large perturbations.

The LGM has long been used to constrain ECS by comparing global mean cooling with estimates of combined radiative forcing from lower greenhouse gas concentrations, larger ice sheets and changes in dust and vegetation. Early studies were limited by uncertainties in both temperature reconstructions and forcings, leading to a wide range of inferred sensitivities. Recent reconstructions by Tierney et al. (2020b), Osman et al. (2021) and Annan and Hargreaves (2022) have substantially reduced these uncertainties, converging on a relatively robust estimate of LGM cooling. By combining these

reconstructions with updated forcing estimates, Tierney et al. (2020b) inferred an ECS of about 3.4 °C, with uncertainty ranges that are broadly consistent with, but somewhat narrower than, earlier LGM based estimates. IPCC AR6 used these results, along with other lines of evidence, to argue that ECS values above about 5 °C are unlikely, in part because such high sensitivity models yield glacial climates inconsistent with reconstructions (IPCC, 2021).

Warm periods such as the Pliocene, in turn, provide constraints on sensitivity in warmer climate states. Analyses of reconstructed global and regional temperatures together with CO_2 estimates suggest that the Earth system, including slow feedbacks such as vegetation and ice sheets, may exhibit higher effective sensitivity under warm conditions (Tierney et al., 2020a; Lunt et al., 2024). While uncertainties remain large, these studies caution against assuming that sensitivity inferred from the instrumental era alone applies unchanged under substantially higher CO_2 levels.

Over the last millennium, reconstructions of hemispheric temperature have been combined with estimates of volcanic, solar and greenhouse gas forcing in detection and attribution frameworks. Hegerl et al. (2006) showed that climate sensitivity values that are too low cannot reproduce the amplitude of reconstructed preindustrial variability when forced with realistic external forcing, thereby setting a lower bound on ECS. Subsequent work with larger proxy networks, including PAGES 2k, has reinforced the conclusion that very low sensitivities are inconsistent with both instrumental and paleoclimate evidence (PAGES 2k Consortium, 2013; IPCC, 2021).

Taken together, paleoclimate constraints at cold, intermediate and warm climate states play a central role in narrowing the plausible range of ECS and in ruling out models with implausibly high or low sensitivity. In this sense, paleoclimate reconstructions are not merely qualitative context but quantitative benchmarks for model accuracy in the dimension that matters most for long term projections.

7. METHODOLOGICAL ADVANCES AND THEIR IMPLICATIONS FOR MODEL EVALUATION

The increasing integration of PSMs and paleoclimate data assimilation into climate science has important consequences for how model accuracy is assessed. PSMs reduce conceptual mismatches between model output and

proxy data by making comparisons in proxy space and by enabling systematic tests of how uncertainties in proxy formation processes affect reconstructions and model–data misfits (Steiger et al., 2017; Tierney et al., 2023). For example, PSMs can be used to examine how changes in seasonality, growth thresholds or water availability influence tree ring proxies, thereby clarifying whether model biases in reconstructed tree ring widths reflect errors in simulated climate or misinterpretation of the proxy.

Paleoclimate data assimilation extends this approach by incorporating proxy information directly into model ensembles. The resulting reconstructions provide spatially complete fields with explicit uncertainty estimates, which can be compared to both independent proxies and to simulations performed with the same or different models (Steiger et al., 2017; Osman et al., 2021; Annan & Hargreaves, 2022; Tierney et al., 2023). Importantly, data assimilation frameworks can also be used in calibration mode, where model parameters are adjusted to improve the fit to paleodata while maintaining consistency with physical constraints and present day observations. The LGM constrained tuning of CESM2 cloud parameters by Zhu et al. (2022) is one example; similar approaches could be applied to other parameters and climate states.

These methodological advances shift paleoclimate reconstructions from being loosely interpreted "targets" to being integral components of the model development cycle. Accurate representation of past climates becomes not only a test of model fidelity but also a source of information used to reduce parametric and structural uncertainties in climate models.

8. UNCERTAINTIES, LIMITATIONS AND BEST PRACTICES

Despite their value, paleoclimate reconstructions are subject to substantial uncertainties that must be considered when using them to evaluate models. Proxy–climate relationships may be nonlinear and may change over time as ecological communities adapt or as background conditions shift. Chronological uncertainties, such as dating errors in sediments or age model uncertainties in speleothems, can blur the temporal alignment between proxies and model-simulated events, particularly for abrupt changes (Jansen et al., 2007; IPCC, 2013). Spatial coverage remains uneven, with relatively dense networks in some regions (e.g. mid latitude land areas) but sparse data in others,

such as the Southern Ocean and parts of Africa, which can limit the robustness of global or regional syntheses (PAGES 2k Consortium, 2013; Tierney et al., 2020a). Forward models of proxy formation also involve simplifying assumptions and uncertain parameters (Steiger et al., 2017; Tierney et al., 2023).

Climate models themselves possess significant uncertainties. Parameterizations of cloud microphysics, boundary layer turbulence and aerosol–cloud interactions remain major sources of inter model spread in climate sensitivity and regional climate responses (Flato et al., 2013; IPCC, 2021). Long term processes, including dynamic ice sheets and some biogeochemical feedbacks, are represented only in a subset of models or in a simplified manner. Reconstructions of past forcings, particularly CO_2 and other greenhouse gases, ice sheet extent and aerosol loading, also carry uncertainties that propagate into simulated climates (Jansen et al., 2007; IPCC, 2013).

Given these limitations, best practice in using paleoclimate reconstructions to assess model accuracy involves several elements. First, model–data comparison should employ multiple metrics, including global mean changes, spatial patterns and regional indices, rather than relying on a single diagnostic (Braconnot et al., 2012; Brierley et al., 2020; Tierney et al., 2020b). Second, comparisons should be formulated in a probabilistic framework that accounts explicitly for uncertainties in both reconstructions and simulations, for example by using ensembles of reconstructions and model realizations. Third, where possible, comparisons should make use of PSMs or data assimilation products so that model–data misfits are interpreted in the correct variable space and with consistent temporal and spatial averaging (Steiger et al., 2017; Tierney et al., 2023). Finally, paleoclimate evidence should be integrated with instrumental era and process based constraints, as in the assessment framework used by IPCC AR6 to infer ECS (IPCC, 2021; Lunt et al., 2024).

9. CONCLUSIONS

Paleoclimate reconstructions play a critical role in assessing the accuracy of climate models. By extending the evaluation domain beyond the short instrumental record, they allow models to be tested under a wide range of boundary conditions and climate states, including climates substantially colder

and warmer than today. Case studies from the LGM, mid Holocene, the last millennium and past warm periods demonstrate that many models can reproduce key features of past climate change, lending confidence to their physical foundations, but also reveal important biases in the simulation of tropical sea surface temperatures, monsoon rainfall and polar amplification (Braconnot et al., 2012; Brierley et al., 2020; Tierney et al., 2020a, 2020b; Osman et al., 2021).

Paleoclimate constraints have become central to narrowing the plausible range of climate sensitivity. LGM and last millennium reconstructions have been used to rule out models with very low or very high sensitivity, while warm climate reconstructions suggest that feedbacks may be state dependent and that Earth system sensitivity in greenhouse climates may exceed that inferred from recent observations alone (Tierney et al., 2020a, 2020b; Hegerl et al., 2006; IPCC, 2021; Lunt et al., 2024). Methodological advances in proxy system modelling and data assimilation further strengthen the link between paleoclimate data and climate models, enabling rigorous probabilistic tests of model performance and direct use of paleodata to calibrate uncertain model parameters (Steiger et al., 2017; Zhu et al., 2022; Tierney et al., 2023).

Looking ahead, deeper integration of paleoclimate reconstructions into model development and evaluation frameworks will be essential. As new proxy records are obtained from under sampled regions, as reconstructions become more spatially complete and as next generation Earth System Models incorporate more processes, paleoclimate evidence will continue to refine our understanding of climate feedbacks and sensitivity. In this sense, paleoclimate reconstructions are not simply historical curiosities; they are fundamental benchmarks that determine how much trust we can place in projections of future climate change and thus in the decisions that depend on them.

REFERENCES

Annan, J. D., & Hargreaves, J. C. (2022). A new global surface temperature reconstruction for the Last Glacial Maximum. *Climate of the Past*, 18, 1883–1901.

Braconnot, P., Harrison, S. P., Kageyama, M., et al. (2012). Evaluation of climate models using palaeoclimatic data. *Nature Climate Change*, 2, 417–424.

Brierley, C. M., Zhao, A., Harrison, S. P., et al. (2020). Large scale features and evaluation of the PMIP4 CMIP6 mid Holocene simulations. *Climate of the Past*, 16, 1847–1872.

Flato, G., Marotzke, J., Abiodun, B., et al. (2013). Evaluation of Climate Models. In T. F. Stocker et al. (Eds.), Climate Change 2013: The Physical Science Basis. Contribution of Working Group I to the Fifth Assessment Report of the IPCC (Chapter 9). Cambridge University Press.

Hegerl, G. C., Crowley, T. J., Hyde, W. T., & Frame, D. J. (2006). Climate sensitivity constrained by temperature reconstructions over the past seven centuries. *Nature*, 440, 1029–1032.

IPCC. (2007). Climate Change 2007: The Physical Science Basis. Contribution of Working Group I to the Fourth Assessment Report of the IPCC (Chapter 6: Palaeoclimate). Cambridge University Press.

IPCC. (2013). Climate Change 2013: The Physical Science Basis. Contribution of Working Group I to the Fifth Assessment Report of the IPCC (Chapter 5: Information from Paleoclimate Archives). Cambridge University Press.

IPCC. (2021). Climate Change 2021: The Physical Science Basis. Contribution of Working Group I to the Sixth Assessment Report of the IPCC (especially Chapter 7: The Earth's Energy Budget, Climate Feedbacks, and Climate Sensitivity). Cambridge University Press.

Jansen, E., Overpeck, J., Briffa, K. R., et al. (2007). Palaeoclimate. In S. Solomon et al. (Eds.), Climate Change 2007: The Physical Science Basis. Contribution of Working Group I to the Fourth Assessment Report of the IPCC (Chapter 6). Cambridge University Press.

Kageyama, M., Braconnot, P., Harrison, S. P., et al. (2018). The PMIP4 contribution to CMIP6 – Part 1: Overview and over arching analysis plan. *Geoscientific Model Development*, 11, 1033–1057.

Ludwig, P., Schaffernicht, E. J., Shao, Y., & Pinto, J. G. (2018). Regional climate modelling of the last glacial maximum and the Holocene over Europe: Perspectives and limitations. *Climate of the Past*, 14, 613–630.

Lunt, D. J., Hargreaves, J. C., Annan, J. D., et al. (2024). Paleoclimate data provide constraints on climate models' large scale response to past CO_2 changes. *Communications Earth & Environment.*

Mann, M. E., Zhang, Z., Hughes, M. K., et al. (2008). Proxy based reconstructions of hemispheric and global surface temperature variations over the past two millennia. *Proceedings of the National Academy of Sciences*, 105, 13252–13257.

Osman, M. B., Tierney, J. E., Zhu, J., et al. (2021). Globally resolved surface temperatures since the Last Glacial Maximum. *Nature,* 599, 239–244.

PAGES 2k Consortium. (2013). Continental scale temperature variability during the past two millennia. *Nature Geoscience*, 6, 339–346.

Steiger, N. J., Smerdon, J. E., Cook, E. R., & Cook, B. I. (2017). A reconstruction of global hydroclimate and dynamical modes over the Common Era. *Journal of Climate*, 30, 6097–6124.

Tierney, J. E., Haywood, A. M., Feng, R., Bhattacharya, T., & Otto Bliesner, B. L. (2020a). Past climates inform our future. *Science*, 370, eaay3701.

Tierney, J. E., Zhu, J., King, J., Malevich, S. B., Hakim, G. J., & Poulsen, C. J. (2020b). Glacial cooling and climate sensitivity revisited. *Nature*, 584, 569–573.

Tierney, J. E., Tingley, M. P., & Anchukaitis, K. J. (2023). Advances in paleoclimate data assimilation. *Annual Review of Earth and Planetary Sciences*, 51, 71–100.

Zhu, J., Poulsen, C. J., Otto Bliesner, B. L., et al. (2022). LGM paleoclimate constraints inform cloud parameterizations and equilibrium climate sensitivity in CESM2. *Journal of Advances in Modeling Earth Systems*, 14, 1-18.

CHAPTER 4

ASSESSING HUMAN IMPACT IN LAKE SEDİMENTS USING PALYNOLOGICAL EVIDENCE: CASE STUDIES FROM TÜRKİYE

MSc (PhD Student) Renas Ali ROSTM[1],

Assist. Prof. Dr. Ayşegül Feray GÖKDERE[2],

Assoc. Prof. Dr. Nurdan YAVUZ[3]

---

[1] Van Yüzüncü Yıl University, Institute of Nature and Applied Science, Van, Türkiye.ORCID: 0000-0001-9137-3397

[2] Van Yüzüncü Yıl University, Faculty of Engineering, Department of Geological Engineering, Van, Türkiye.ORCID: 0000-0002-3842-1711

[3] General Directorate of Mineral Research and Exploration, Department of Geological Research, Ankara, Türkiye.ORCID: 0000-0002-1141-401X

1. INTRODUCTION

Palynology, the study of pollen, spores and other palynomorphs in sediments is now widely recognized as one of the most useful tools for reconstructing past vegetation, past climate and human–environment interactions (e.g.Faegri and Iversen, 1989; Moore et al., 1991; Beug, 2004). Since pollen grains are produced in large numbers with chemically resistant walls of exine made from a coating of sporopollenin, they are commonly preserved in lake, peat and deltaic sediments (Traverse, 2007). Because each plant taxon has distinct pollen morphologies, the assemblages in specific sedimentary units can be interpreted to represent discrete but closely spaced local vegetation communities. As a consequence, palynology is a key proxy for monitoring local-scale ecological development, climate oscillations and anthropogenic impact at the Quaternary timescale (Birks and Birks, 1980; Seppä & Bennett, 2003).

In palaeoenvironmental studies, lake sediments are one of the most continuous and datable archives in nature. Lakes preserve autochthonous and allochthonous deposits such as pollen, charcoal, diatom, and geochemical evidence to integrate the climatic signal with vegetation response overlying human influence (Roberts et al., 2001; Battarbee et al., 2005). Unlike fluvio-deltaic deposits, lacustrine successions are generally less disturbed by extraneous disturbances and tend to be accurate in their chronostratigraphy, for example when dated using radiocarbon and varve or tephrochronology. Thus lake-sediment pollen provides very detailed information on vegetation and land-use histories, often extending through the entire Holocene (Litt et al., 2012; Dean et al., 2015).

At a global scale, palynological records have been able to detail Holocene histories of climate and human land use across Europe to the Near East (Roberts et al., 2011). Anatolia is a key biogeographic connector between Europe, Asia and the Middle East; as a climatic and ecological edge zone this land has been very sensitive to small changes in temperature but particularly precipitation (Atalay, 1994; Litt et al., 2012). However, in despite of the growing regional studies, large-scale syntheses including multiple lake pollen records from throughout Türkiye are rare, so that an evaluation at country scale becomes particularly scientific relevant.

In Türkiye, which is situated at the crossroad of Mediterranean, Irano–Turanian and Euro-Siberian phytogeographic regions, pollen records are particularly important for reconstruction of biogeographical and climatic evolution (Atalay, 1994; Roberts et al., 2011). The country has topographic gradients ranging from humid coasts to semi-arid plateaus in the interior, which creates a variety of ecosystems that are highly responsive to climate variability. Anatolian lakes (e.g., Van, Beyşehir, Gölhisar, Nar Gölü and Eski Acıgöl) exhibit very thick and complete sediment sequences that are well suited to reconstructing the timing and scale of vegetation change, hydrological variability and anthropogenic impacts (Eastwood et al., 1999; Wick et al., 2003; Dean et al., 2015).

Multi-proxy investigations of the past 50,000 years utilizing palynology, geochemistry, isotopic measurements and sedimentology led to detailed reconstructions of Holocene forest expansion-deforestation-regeneration transitions (Wick et al., 2003; Roberts et al., 2011; Litt et al., 2012). These findings indicate that intensive human activity associated with crop cultivation, grazing and settlement has been a major force driving landscape transformation for the last 8 000 years, overlaying natural climatic variability.

Thus, this chapter presents the principles and use of palynological indicators of human impact, and a synthesis of available published pollen records from lake sediments in Türkiye. Compartmentalization of material by major geographical regions western, central, northwestern and eastern Anatolia is intended to draw attention to regional consistency/inconsistency in Holocene vegetation dynamics and land-use history. In combination these sources present an integrated structure in which to assess the spatial and temporal development of human modification of the Anatolian environment.

2. POLLEN AS AN INDICATOR OF HUMAN IMPACT
2.1. Principles of Pollen Analysis in Lacustrine Environments

Pollen analysis is a method of interpretation that involves the recognition and counting of well-preserved pollen grains from stratified sediments, most effectively in lakes with continuous input of sediment under stable hydrological conditions (Faegri and Iversen, 1989; Moore et al., 1991). Different species of plants all produce different pollen grain shapes, which can be used to reconstruct the type of vegetation that existed in an area at different times (Beug

2004). In lake basins the pollen is carried not only by air but also in surface inflow, and the pollen spectrum thus mirrors a complex of the local vegetation from the catchment area as well as regional bioclimatic conditions (Traverse, 2007).

Spores and pollen retain the wall of sporopollenin that is highly resistant to chemical degradation and may be preserved for tens of thousands years in anoxic sediments. The composition of the surrounding vegetation, this is an indirect consequence of the environmental and climatic conditions (Birks and Birks, 1980; Seppä and Bennett, 2003), can be inferred from the relative proportions of different types of pollen in a section. With accurate chronological control (e.g. radiocarbon or varve dating), pollen analysis furnishes a continuous and datable record of vegetational change and human activity.

2.2. Anthropogenic Indicators in Pollen Assemblages

Human activity has a characteristic and quantifiable signature in the pollen record, as can be seen in both the appearance of cultivated taxa and increase of disturbance-tolerant plants (Behre, 1986; Roberts et al., 2011).

Cultivated pollen types such as *Olea europaea, Juglans regia, Castanea sativa, Vitis vinifera* and cerealtype Poaceae represent typical projective signs of agro-forestry practices (Bottema and Woldring 1990; Eastwood et al., 1999). The synchronous appearance of these taxa in southwestern Anatolia marks the Beyşehir Occupation Phase, a well-documented episode of agricultural expansion and forest clearance (van Zeist et al., 1975; Eastwood et al., 1999).

The presence and spread of ruderal and weedy taxa such as *Plantago lanceolata, Rumex, Urtica, Chenopodiaceae* or *Polygonum/Persicaria* is indicative of soil disturbance, grazing and higher nutrient levels in the environment around settlements (Bottema & Woldring, 1990; Roberts et al., 2011). These taxa are quick to react to clearing or trampling and act as sensitive indicators of the human impact.

Instead, pastoralism is inferred from rises in non-arboreal pollen (NAP), particularly steppe taxa including *Artemisia* and Amaranthaceae often together with coprophilous fungal spores (*Sporormiella, Podospora*) developed on herbivore dung (Davis and Shafer, 2006; Raper and Bush, 2009). The presence

of both of these proxies together provides powerful evidence for livestock grazing and landscape openness.

2.3. Interpretation of AP/NAP Ratios and Charcoal Co-Variation

One important quantitative proxy for deforestation and woodland opening is the ratio of arboreal pollen (AP) to non-arboreal pollen (NAP) in the pollen target area (Roberts et al., 2011). A reduction in AP compared to NAP is usually interpreted as forest destruction whereas the return of arboreal pollen may be related to reforestation or land abandonment. When low AP/NAP ratios are concurrent with high values of microscopic charcoal, this trend is generally interpreted as anthropogenic burning related to agriculture or pastoral (Tinner et al., 1998).

Therefore, the combined charcoal–pollen approach allows us to discriminate natural from anthropic fires. This co-variation has been recorded in a number of Anatolian Lake records (e.g., Lakes Beyşehir and Van) where charcoal maxima generally correspond to periods of intensive human activity and cultivation (Eastwood et al., 1999; Wick et al., 2003).

2.4. Strengths and Limitations of Pollen Records for Reconstructing Human Impact

Thus, palynological information represents one of the most continuous, datable and regionally integrative sources of records on vegetation and human impact. The great advantage of this method is the fact that both climate and human impact is recorded in the same sediment sequence (Faegri and Iversen, 1989). Pollen data, however, are subjected to constraints due to taphonomy, production and transportation as well.

Some taxa, including *Pinus*, are high pollen producers and over-represented whereas others that are insect-pollinated such as *Juglans* and *Vitis* are often underrepresented (Moore et al., 1991). Furthermore, local land-use impacts may be subtended by larger regional pollen rain and preservation of pollen in an oxidized sediment can also bias assemblages (Traverse, 2007). It is for these reasons that strong interpretations of human impact are in need of correlation with archaeological, charcoal, geochemical and sedimentological evidence (Roberts et al., 2011; Dean et al., 2015). Nevertheless, the analysis of

pollen grains continues to be one of the most accurate methods and is used most extensively method for reconstruction of human–environment interaction.

3. OVERVIEW OF PALYNOLOGICAL RECORDS FROM TÜRKİYE

3.1. Western and Southwestern Anatolia

Western and Southwestern Anatolia has many of the most extensively studied Holocene lake records in Türkiye such as at Lake Beyşehir, Lake Gölhisar and Gravgaz Marsh. Together, these records provide evidence for one of the most prominent episodes of anthropogenic landscape impact in Anatolian palynology: The Beyşehir Occupation Phase (BOP). The BOP was originally introduced by van Zeist et al. (1975) and later updated by Bottema and Woldring (1990) and Eastwood et al. (1999).

During the period from ~ 3500 to 1300 cal BP, the pollen spectra of these sites are characterized by arboreal, cultivated taxa including *Olea europaea* and *Juglans regia*, with *Castanea sativa* being the most dominant species together with *Vitis vinifera* and cereal-type Poaceae. These agroiforms correspond to a significant reduction of forest taxa, particularly *Quercus, Pinus* and *Juniperus* which reflect the high degree of deforestation (Eastwood et al., 1999). Enhanced ratio of ruderal herbs *Plantago lanceolata, Rumex* and *Urtica* reflects human disturbances in the proximity of settlement areas and soil enrichment.

The age of these vegetational transitions overlaps with archaeological indications of an agricultural intensification and population increase in the Late Bronze Age, Hellenistic and Roman times. Multi-proxy studies from these basins indicate increased charcoal input, accelerated rates of sedimentation, and elevated carbonate concentrations, which are considered as signs or symptom associated with land clearance and cultivation-induced erosion (Eastwood et al., 1999; England et al., 2008; Roberts et al., 2011). After ca. 1300 cal BP, the pollen record show a partly re-forestation with restored *Quercus* and *Pinus* and indicates land abandonment or decreased agricultural activity during Early Medieval times. The BOP therefore provides an important regional palynological signal for agricultural expansion in the Mediterranean and correlates with contemporary periods of human intensification within Greece and the Levant (Roberts et al., 2011).

3.2. Central Anatolia

There are dozens of closed-basin lakes in Central Anatolia, some with thick Holocene deposits (e.g., Nar Gölü, Eski Acıgöl and Akgöl) that have well-preserved pollen records and geochemical signatures. These records show phases of cultivation, pasturage and recovery over the last six thousand years (Jones et al., 2006; Dean et al., 2015).

It can be inferred on the bases of pollen types such as cereals, *Plantago, Rumex* and Chenopodiaceae from the late Holocene part of Nar Gölü sequence that several stages of agricultural activities were followed. Microcharcoal maxima show a good correspondence with minimum arboreal pollen as well, suggesting controlled burning for clearance (Dean et al., 2015). Stable isotope and sedimentological analyses show that climate alone cannot account for these changes, but instead seem to relate to shifts in land-use intensity that correspond with socio-economic transitions from Byzantine through Ottoman times (England et al., 2008; Dean et al., 2015).

A similar trend in the pollen assemblages is observed at Eski Acıgöl. Pattern of "oscillating" increases and decreases between Poaceae, steppe taxa (*Artemisia)* and *Artemisia* derived taxon (Amaranthaceae) vs. *Quercus, Pinus* indicate cycles of clearance and partial reforestation in the area (Jones et al., 2006). These oscillations are confirmed by archaeological and sedimentary data that indicated discontinue occupation and grazing. Taken together, records from the Central Anatolian Lakes prove that over the last two millennia, human activities, rather than climate change, have been the key factor controlling vegetation dynamics.

3.3. Northwestern Anatolia

Palynological studies in Lake İznik and surrounding marshes of northwestern Anatolia represent one of the longest Holocene vegetation records in Türkiye (Miebach et al., 2016). The early Holocene is characterized by mixed deciduous forests with *Fagus, Carpinus, Quercus*, and *Ulmus* indicating relatively humid conditions. Around 4800 cal BP a heavy drop in AP abundance is registered, correlating with the earliest continuous presence of cereal and weedy species such as *Plantago, Polygonum/Persicaria* and Chenopodiaceae indicating the start of systematic cultivation activities and clearance (Miebach et al., 2016).

From the Hellenistic to Roman access, agriculture is stepped up, reflected in high cereal pollen frequencies and abundant charcoal indicative of fire events. *Juglans* and *Castanea* among them soon indicate the practice of arboriculture. This transformation corresponds with archaeological indicators of densely settled networks and intensive farming infrastructures in the İznik basin and within the Marmara region. Subsequent to the Byzantine Period, pollen evidence indicates a slow rise in some forest taxa indicating partial woodland recovery.

3.4. Eastern Anatolia

The most extensive palaeoenvironmental records from Eastern Anatolia come from Lake Van, one of the largest endorheic basins in the Near East. The ICDP PALEOVAN Project yielded more than 200m of sediment and an unprecedentedly long, in parts continuous sequence for ∼500 kyr (Litt et al., 2012; Stockhecke et al., 2014) that was accomplished in 2010. More generally, the long-term pollen record of Lake Van broadly follows glacial–interglacial climate oscillations, with the prevalence of steppe taxa (*Artemisia*, Chenopodiaceae) during cold–dry periods and expansion of temperate forest elements (*Quercus, Pistacia, Pinus*) in warm–humid intervals (Wick et al., 2003; Litt et al., 2009).

In the late Holocene anthropogenic signs are more prominent. Early evidence of human impact dates back to about 3800 cal BP, limited to very discrete rises of *Plantago lanceolata*, *Rumex* and *Juglans regia* (Wick et al., 2003). This increase worsens between AD 1250 and 850, a period that is characterized by an increase in charcoal concentrations and with the documented enlargement of settlements around the Van Basin (Litt et al., 2009; Çağatay et al., 2014). Integrating palynological, geochemical and isotopic proxies reveals that climatic variability was consistently the dominant driver of vegetation development albeit with human activities -- particularly agriculture and grazing -- assuming increasing importance across the late Holocene.

Other than Lake Van, palynological and geochemical various studies have recently conducted in lakes such as Erçek and Hazar (Rostm, 2018; Biltekin et al. 2018). These small tectonically controlled basins afford more

precise Holocene palaeoenvironmental reconstructions, showing how regional climatic forcing interacted with human activities at a local level.

4. REGIONAL SYNTHESIS

4.1. General Patterns of Human Impact in Türkiye

The palynological and multi-proxy investigations carried out in Anatolian Lake basins offer a unique overview of Holocene vegetation dynamics and human–environment interactions. When aggregated across all macroregions, they show a consistent pattern for the evolution of the environment controlled by climatic variability as well as human impact.

During the Early Holocene (ca. 11,700–8,000 cal BP), the construction of the vegetation was predominated by natural climatic improvement that occurred after Late Glacial times in Türkiye. The pollen from lakes such as Van, Beyşehir and Nar Gölü are indicative of the dominance of arboreal taxa in particular *Quercus, Pinus, Juniperus* and *Pistacia* suggesting an expansion of closed-candopied forest vegetation under warmer/wetter conditions (Wick et al., 2003; Litt et al., 2009; Roberts et al., 2011). Human impact during this time was relatively low, as reflected by the archaeological record with a technologically simple population and small scale modest activities of hunters-gatherers. This can be interpreted as a period of natural forest regeneration and ecosystem stabilization (early Holocene), forming the reference scenario for further anthropogenic intervention.

The Mid-Holocene (ca. 8,000 to 4,000 cal BP [calibrated before present] that marks the first substantial human transformation of the Anatolian environment. Palynological data from southwestern and inland parts of Türkiye provide evidence for forest clearance, low-level cultivation, and the early spread of disturbance-tolerant herbs including *Plantago lanceolata, Rumex* and *Urtica* (Eastwood et al., 1999; Jones et al., 2006). These shifts are contemporary to early agropastoral communities of the Neolithic and Chalcolithic. Decrease in *Quercus* and *Pinus* pollen observed in several records, along with high values of cereal-type Poaceae shows localized clearance and primitive cultivation. Episodic climate variability during the Mid-Holocene, such as the 8.2 ka BP cooling and other aridification events (North Greenland Ice Core Project members, 2004), may have increased ecosystem sensitivity of these systems

(Roberts et al., 2011). The pollen data indicate an increasing human impact that remains local in character, the area of settlements.

The Late Holocene (after ca. 4,000 cal BP) is a time that coincides with profound increase of human impact on and more or less permanent changes in the vegetation cover. The most dramatic and spatially coherent manifestation of this change is the Beyşehir Occupation Phase (BOP), recorded in several lakes in south-west Anatolia (van Zeist et al., 1975; Eastwood et al., 1999). The BOP, dated between ca 3,500-1,300 cal BP is characterised by the prevalence of cultivated pollen types as *Olea europa, Juglans regia, Castanea sativa,Vitis vinifera* as well as poaceas cereal-type and a sharp contraction in forest species. Charcoal peaks and high sedimentation rates are also consistent with significant burning and soil erosion (Bottema and Woldring, 1990). These trends are comparable to those of the Late Bronze Age-Roman assemblages where rapid population growth, urbanization and organized agriculture is known throughout southwestern Türkiye.

Further evidence of massive deforestation and intensive cultivation and ruderal taxa during this period has also been reported in Central and NW Anatolia (Miebach et al., 2016; Dean et al., 2015). However, the extent of these changes depended on local environmental limitations. By contrast, Eastern Anatolia (and primarily the Lake Van Basin) has a stronger climatic signal that responses to anthropogenic disturbance appear later and less pronounced on this site as compared to the rims in general after ca. 3,800 cal BP (Wick et al., 2003; Litt et al., 2009). The late Holocene *Plantago-Rumex-Juglans* subzone displays a small-amplitude change that may be interpreted as the optimal responses to pastoral and agricultural practices in around lake sites.

After the post-BOP period (c. 1,300 cal yr BP), pollen diagrams from multiple Anatolian basins demonstrate the progressive reforestation and a short-term decrease of anthropogenic pressure on land-use. This tends to be interpreted as a reflection of lowered settlement density and political reorganization in the EMA (Eastwood et al., 1999; Litt et al., 2009). Then, in the late Ottoman and modern periods, expansion agriculture was reactivated with increased measures of deforestation around settlement areas and spreads of cultivated species as found in late Holocene deposits from Nar Gölü, İznik and Van (Dean et al., 2015; Miebach et al., 2016; Wick et al., 2003).

The combined palynological data from Türkiye thus indicate a cyclic pattern of forest expansion, deforestation, agroecosystem development and partial reforestation reflecting the confounding effects of climate change and human socioeconomic evolution.

4.2. Comparative Perspective with Other Mediterranean Regions

Strong similarities as well as regional differences are evident when the Anatolian pollen record is considered in comparison to those from other areas of the Mediterranean. Broadly comparable patterns of Late Holocene intensification of agropastoral activity, particularly the Beyşehir Occupation Phase, are recorded in Greece, Crete, southern Italy and the Levant (Roberts et al., 2011). Throughout the eastern Mediterranean region, associated *Olea, Juglans, Castanea* and cereal pollen in assemblages sites indicate that this form of arboriculture and field cultivation together probably evolved within a relatively clement climate during Late Bronze to Classical times.

The Anatolian peninsula has a high degree of topographic and climatic variability compared to west Mediterranean sites, however. While the ancestors of the latter were planting olives and vines in climates around the Mediterranean, their compatriots in the continental interior inhabited semi-arid steppe struggling for agriculture on a large scale. As a consequence, anthropogenic signals measured in pollen time series are weaker and less continuous in Central (and eastern) Anatolia than the dense commercial indicators which are observed for Greece or Italy (Eastwood et al., 1999; Wick et al., 2003).

Another important difference is associated with the age of first pronounced human impact. From ca 3,500 BP in western Anatolia and the Aegean most lands were put under intensification processes that occurred about a millennium later than those in the Levant and southern Mediterranean (BOP, Roberts et al., 2011). These disparities in time frames primarily respond to the imbalance between rates of cultural growth, trade networks and political centralisation rather than merely being a product of disparities in productive potential. But despite this diversity, all areas share a basic correlation between the appearance of complex societies and the spread of settled agriculture, as preserved in pollen sequences

4.3. Integration of Archaeological and Historical Evidence

Palynological evidence alone cannot fully answer the questions of why and how passive vegetation change occurred in a certain area; therefore, integration with human records (e.g. archaeological or historical archives) is important for the interpretation of palaeovegetation change. Data from site surveys and excavations across the Pisidian Highlands, Lycia, and the Konya Plain show settlement patterns cluster in time with terrace building activity, extensification of agricultural land-use over naturally wooded areas in coincidence with inferred periods of forest loss and crop-pollen increase observed within lake sediments (Eastwood et al., 1999; England et al., 2008).

Higher *Plantago* and *Juglans* pollen in the Lake Van Basin between AD 1250 and 850 corresponds with known expansion of medieval, early Ottoman settlements etc., (Wick et al., 2003). Analogous relationships among charcoal peaks, anthropogenic pollen and archaeological activity are demonstrated at other sites in the vicinity of İznik and Nar Gölü (Dean et al., 2015).

Palaeoecological evidence is supported by historical records with Byzantine tax to Ottoman cadastral information revealing episodes of agro-pastoral intensification and deintensification (Haldon et al., 2014). The integration of both archaeobotany and palaeoecological data thereby improves the temporal precision and interpretative context, so that past cultural events causing vegetation change can be pinpointed. This interdisciplinary strategy is essential for identifying anthropogenic landscape effects in a region characterized by climate variability and developing detailed reconstructions of the Holocene environmental history in Anatolia.

5. CONCLUSIONS

Palynological investigations conducted on lacustrine series throughout Türkiye have resulted in a detailed and well-supported reconstruction of Holocene environmental change and human–landscape interaction. Once the regional records are combined, they display a coherent story of vegetation change linked to the interaction between natural climate variability and increasing human impact.

In the Early Holocene, a forest process prevailed across Anatolia with the post-glacial warming / increased humidity. Mid Holocene palynological

sequences document the earliest local clearances and small scale cultivation coterminous with early farming societies. By the Late Holocene, human impact was so high that entire ecosystems were transformed. The Beyşehir Occupation Phase, as it is well reflected in western and southwestern Anatolia, represents a time when arboculture, cereal cultivation and grazing were regionally widespread business and forest pollen decreased extremely. Successive centuries alternated periods of agricultural intensification, land abandonment and partial reforestation corresponding to socio-economic and political oscillations that are noticeable both in archaeological and historical texts.

In spite of significant spatial variation, all of the main lake archives from Van and Erçek in the east to Beyşehir, Nar Gölü and İznik in the west report broadly contemporaneous phases of deforestation, cultivation and subsequent reforestation. Anthropogenic pollen taxa such as *Plantago lanceolata, Rumex, Juglans regia*, and cereal-type Poaceae indicate the continued importance of people as a selective ecological factor over at least several millennia. The natural hydrological and vegetational fluctuations were certainly affected by climatic oscillations, but the overall palaeoecological evidence demonstrates a steadily growing human impact on natural trends in the later Holocene.

Subsequent research should focus on tying the available pollen sequences to high-resolution geochemical, isotopic and archaeological datasets in order to build spatially specific quantitative models of land use change across Anatolia. Comparative study of contrasting physiographic provinces like (i) Mediterranean, (ii) Central Anatolian and the (iii) Eastern Anatolian will provide better understanding for regional sensibilities to climate forcing/landscape response together with human pressure. In addition, the alignment of chronologies with Bayesian age modelling and the development of a national palynological database are likely to improve temporal resolution and data availability.

To conclude, the lake sediments of Türkiye are one of the richest natural archives for studying Holocene climate–culture links in the eastern Mediterranean. Identifying with greater precision what kind of human actions affected the history of these lakes will constitute a further substantive step toward an empirically based understanding how regional and local environmental systems have responded to past human impact, as well as being

essential resources for evaluating future ecological changes under persistent anthropogenic pressure.

REFERENCES

Atalay, İ. (1994). *Türkiye vejetasyon coğrafyası*. Ege Üniversitesi Basımevi.

Battarbee, R. W., John Anderson, N., Jeppesen, E. R. I. K., & Leavitt, P. R. (2005). Combining palaeolimnological and limnological approaches in assessing lake ecosystem response to nutrient reduction. Freshwater Biology, 50(10), 1772-1780.

Behre, K. E. (Ed.). (1986). *Anthropogenic indicators in pollen diagrams* (p. 232). Rotterdam: AA Balkema.

Beug, H. J., 2004. *Leitfaden der Pollenbestim- mung*. Germany, 542 s

Biltekin, D., Eriş, K. K., Çağatay, M. N., Ön, S. A., & Akkoca, D. B. (2018). Late Pleistocene–Holocene environmental change in eastern Turkey: multi-proxy palaeoecological data of vegetation and lake-catchment changes. *Journal of Quaternary Science*, *33*(5), 575-585.

Birks, H. J. B., & Birks, H. H. (1980). *Quaternary palaeoecology* (p. 289). London: Edward Arnold.

Bottema, S., Woldring, H. (1990). Anthropogenic indicators in the pollen record of the Eastern Mediterranean. In Bottema, S., Entjes-Nieborg, G., van Zeist, W. (Eds.), Man's Role in the Shaping of the Eastern Mediterranean Landscape (231264). Rotterdam: Balkema.

Davis, O. K., & Shafer, D. S. (2006). Sporormiella fungal spores, a palynological means of detecting herbivore density. *Palaeogeography, Palaeoclimatology, Palaeoecology*, *237*(1), 40-50.

Dean, J. R., Jones, M. D., Leng, M. J., Noble, S. R., Metcalfe, S. E., Sloane, H. J., ... & Roberts, C. N. (2015). Eastern Mediterranean hydroclimate over the late glacial and Holocene, reconstructed from the sediments of Nar lake, central Turkey, using stable isotopes and carbonate mineralogy. *Quaternary Science Reviews*, *124*, 162-174.

Eastwood, W. J., Roberts, N., Lamb, H.F., Tibby, J.C. (1999). Holocene environmental change in southwest Turkey: a palaeoecological record of lake and catchment-related changes. Quaternary Science Reviews 18: 671–695.

Faegri, K., Iversen, J., 1989. *Textbook of Pollen Analysis* (4th edn by Faegri, K., Kaland, PE and Krzywinski, K.).

Haldon, J., Roberts, N., Izdebski, A., Fleitmann, D., McCormick, M., Cassis, M., ... & Xoplaki, E. (2014). The climate and environment of Byzantine Anatolia: Integrating science, history, and archaeology. *Journal of Interdisciplinary History*, *45*(2), 113-161.

Jones, M. D., Roberts, C. N., Leng, M. J., & Türkeş, M. (2006). A high-resolution late Holocene lake isotope record from Turkey and links to North Atlantic and monsoon climate. *Geology*, *34*(5), 361-364.

Litt, T., Anselmetti, F. S., Baumgarten, H., Beer, J., Cagatay, N., Cukur, D., ... & PALEOVAN Scientific Team. (2012). 500,000 Years of environmental history in eastern Anatolia: the PALEOVAN drilling project. *Scientific Drilling*, *14*, 18-29.

Litt, T., Krastel, S., Sturm, M., Kipfer, R., Örcen, S., Heumann, G., ... & Niessen, F. (2009). 'PALEOVAN', International Continental Scientific Drilling Program (ICDP): site survey results and perspectives. *Quaternary Science Reviews*, *28*(15-16), 1555-1567.

Miebach, A., Niestrath, P., Roeser, P., & Litt, T. (2016). Impacts of climate and humans on the vegetation in northwestern Turkey: palynological insights from Lake Iznik since the Last Glacial. *Climate of the Past*, *12*(2), 575-593.

Moore, P. D., Webb, J. A., & Collison, M. E. (1991). *Pollen analysis* (pp 216).

Raper, D., & Bush, M. (2009). A test of Sporormiella representation as a predictor of megaherbivore presence and abundance. *Quaternary Research*, *71*(3), 490-496.Roberts, N., Eastwood, W. J., Lamb, H. F., Fiorentino, G., Caracuta, V., 2011. Climatic, vegetation and cultural change in the eastern Mediterranean during the mid-Holocene transition. *The Holocene*, 21 (1): 147–162.

Roberts, N., Eastwood, W. J., Lamb, H. F., Fiorentino, G., Caracuta, V. (2011). Climatic, vegetation and cultural change in the eastern Mediterranean during the mid-Holocene transition. *The Holocene*, 21 (1): 147–162.

Roberts, N., Reed, J.M., Leng, M.J., Kuzucuoğlu, C., Fontugne, M., Bertaux, J., Woldring, H., Bottema, S., Black, S., Hunt, E., Karabıyıkoğlu, M. (2001). The tempo of Holocene climatic change in the eastern Mediterranean region: new high-resolution crater-lake sediment data from central Turkey. The Holocene 11: 721–736.

Rostm, R.A. (2018). *Quantitative Analysis of Paleoclimate Paleoenvironment and Paleovegetation Of Lake Erçek Bottom Sediments*, Yüksek lisans tezi. Van Yüzüncü Yıl Üniversitesi Fen Bilimleri Enstitüsü, Van, Türkiye.

Seppä, H., & Bennett, K. D. (2003). Quaternary pollen analysis: recent progress in palaeoecology and palaeoclimatology. *Progress in Physical Geography*, *27*(4), 548-579.

Stockhecke, M., Kwiecien, O., Vigliotti, L., Anselmetti, F. S., Beer, J., Çağatay, M. N., ... & Sturm, M. (2014). Chronostratigraphy of the 600,000 year old continental record of Lake Van (Turkey). *Quaternary Science Reviews*, *104*, 8-17.

Tinner, W., Conedera, M., Ammann, B., Gaggeler, H. W., Gedye, S., Jones, R., & Sagesser, B. (1998). Pollen and charcoal in lake sediments compared with historically documented forest fires in southern Switzerland since AD 1920. *The Holocene*, *8*(1), 31-42.

Traverse, A. (2007). *Paleopalynology* (Vol. 28). Springer Science & Business Media.

Van Zeist, W., Woldring, H., & Stapert, D. (1975). Late Quaternary vegetation and climate of southwestern Turkey. *Palaeohistoria*, 53-143.

Wick, L., Lemcke, G., Sturm, M. (2003). Evidence of Lateglacial and Holocene climatic change and human impact in eastern Anatolia: high-resolution pollen, charcoal, isotopic and geochemical records from the laminated sediments of Lake Van, Turkey. *The Holocene*, 13(5): 665-675.

CHAPTER 5

STRUCTURAL DESIGN AND ELECTRONIC PROPERTIES INVESTIGATION OF PYRIDOQUINOLYSIS DERIVATIVE OLED MATERIALS

Assist. Prof. Dr. Erhan ÖZTÜRK[1],

Assoc. Prof. Dr. Zeynep Şilan TURHAN[2],

Prof. Dr. Selçuk GÜMÜŞ[3]

[1] Igdir University, Research Laboratory Practice and Research Center (ALUM), 76000 Igdir, Turkey.ORCID: 0000-0003-4006-2428

[2] Igdir University, Faculty of Science and Literature, Department of Biochemistry, 76000 Igdir, Turkey.ORCID: 0000-0002-3587-2576

[3] Bartin University, Faculty of Engineering, Architecture and Design, Department of Basic Sciences, 74000 Bartin, Turkey.ORCID: 0000-0002-8628-8943

1. INTRODUCTION

The current global energy crisis is one of the biggest issues facing humanity [1, 2]. A large part of people's quality of life depends on energy. As fossil fuels are gradually running out, their dependence on these energy sources is increasing day by day. To address this problem, scientists are focused on two areas: (I) developing new materials and (II) improving the functionality of existing materials. The primary goal of this study is to develop novel optoelectronic materials for photonics, processing data, contemporary communications, and light harvesting [1, 3, 4]. Growing concern exists regarding the technological obstacles that solid state technology will ultimately have to overcome. The ability to transport electrons is one of the main requirements for a potential OLED candidate [5-7].

Since Tang and Van Slyke's first invention in 1987, organic light-emitting diodes (OLEDs) have achieved high efficiency in both display lighting technologies and imaging. It has become a focus of great interest for researchers aiming at this efficiency. To compete with the first device, many researchers took into account the transport ability and energy levels of the materials, as well as the thickness of the different layers [8]. OLEDs have recently gained popularity because to its low-temperature approach, great performance, and possibility to include increasingly complicated devices [9]. Compared to Liquid Crystal Display (LCD) technology, it offers a faster image contrast quality, better response time, and refresh rate. OLEDs are thinner and lighter, as well as providing a wider viewing angle. In addition, the biggest advantage of OLED is that it is very energy efficient, as it does not need an additional backlight system. Considering that lighting alone accounts for about 20% of the world's energy consumption, significant energy savings can be achieved if more OLEDs are used in lighting technology. What makes this technology even more impressive is that these devices have a flexible substrate. This marked the beginning of OLED development. Following this groundbreaking breakthrough, there was a surge of interest and effort from both the academic and industrial worlds. These developments have led to the eventual mass commercialization of OLEDs, especially for applications in displays [10]. In fact, given the demands for light, flexible devices and environmentally friendly technologies, it has spurred the rapid development of device technologies with organic-based optoelectronic materials [11].

OLEDs are more potential energy-efficient solutions for future lighting applications. This lighting technology produces flexible, large-area, very light, and economical light sources. Recently, there has been a lot of research on material development and efficiency improvement [12]. OLED technology is not only thin and efficient but also delivers the highest image quality ever. On the other hand, it is foreseen that it will be a lighter, transparent, stretchable, foldable, and even rollable technology for future technologies. OLEDs are aimed at being used more in technological fields such as mobile phones, cars, computers, tablets, laptops, and televisions. This technology is expected to benefit from transparent OLEDs on all windows or non-flat vehicle windshields. This means that it represents the future of technology. OLEDs are devices that consist of an array of organic thin films placed between two electrodes. Each organic layer in the device has a function, and when an external voltage is applied to these devices, they emit light. This phenomenon, known as electroluminescence (EL), is described as the injection of electron charge carriers and electrodes that form electron holes (excitons) in organic semiconductors that move under an electric field [13-15].

There have been several attempts to further improve the internal efficiency of ordinary OLEDs. One example was the creation of a new generation of OLEDs known as phosphor organic light-emitting diodes (PhOLEDs) that contained transition metals. Singlet excitons as well as triplet excitons can be harvested with the aid of increased spin-orbit coupling in PhoLEDs [16-18]. A major breakthrough in high-performance OLEDs began with the discovery of phosphorescent structures containing some heavy transition elements such as Platinum (II) and Iridium (III) [19, 20]. However, the rare availability of heavy metals limits the commercial use of phoLEDs and makes them expensive. Aside from its scarcity and expensive cost, heavy metal waste is poisonous, which causes environmental problems. Due to these disadvantages of organometallic phoLEDs, the third generation of pure organic OLEDs using TADF principles has become more popular [17]. The TADF technique is produced by the low energy difference between the excited states of the first singlet and first triplet (S1-T1). The low singlet and triplet energy gap, the convertibility of triplet excitons to singlet excitons, and the propagation back to the ground state via delayed fluorescence make the transition between inverse systems easy (RISC). Since it is possible to collect singlet and triplet

excitons with the TADF method, an inner quantum efficiency close to 100% can be achieved. As mentioned above, ΔEST acts as an important TADF descriptor as it has a direct impact on the RISC process [21, 22]. In the last decade, intensive research and development has been done to achieve highly efficient devices. As a consequence, approximately 100% internal quantum efficiency has been achieved using phosphorescence and thermally activated delayed fluorescence emitters. OLEDs have dominated electronics' most important current display technology for consumers. Self-emitting, transparent states, effective dark tones, and flexibility are the main features of OLED design screens. It provides superior performance compared to LCD screens. In addition to being used in displays, it is also a very strong candidate for use in lighting [23-25]. OLEDs' long-term viability makes them attractive examples of organic electronics for future environmental problems [26]. To address these issues, an alternate exciton production method known as TADF was found [17, 27].
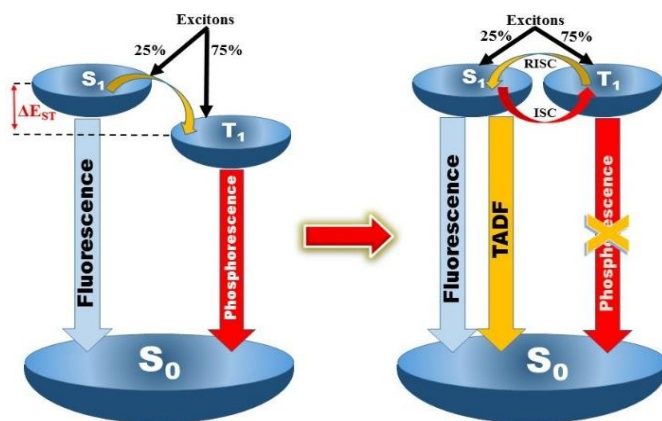
Figure 1.1. The exciton dynamics of a typical TADF emitter in an OLED are shown. Singlet and triplet excitons are generated in a ratio of 1:3. The ratio depends on spin degeneracy.

The next generation of emissive materials is thought to be TADF materials without precious metals. TADF emitters, like phosphorescent emitters, attain 100% internal quantum efficiency (IQE) by converting triplet to singlet excitons via RISC. Disadvantages such as the high cost, use of rare materials, and environmental impact of phosphorescent emitters can also be

easily overcome by them [28-34]. TADF molecules are generally made up of an electron donor (D) and an electron acceptor (A) in a highly twisted shape allowing triplet excitons to undergo fast reverse intersystem crossing (RISC) [10, 35-38]. Numerous extremely effective TADF emitters and corresponding OLEDs have been created based on this design principle [35, 39-42]. Considering Boltzmann statistical values, the lower the ΔEST value, the more easy it is to acquire RISC. Furthermore, a low value of EST indicates that there is a tiny overlap integral between the wave functions of a luminous molecule's ground and excited states. As a result, the electron-electron repulsion force between electron orbitals in the triplet state is minimized [17, 43]. Minimizing the overlap between wave functions is a very efficient strategy for localizing the electron densities of the HOMO-LUMO states included in the donor and acceptor groups [44]. This effect is aided by additional steric separation by including a spiro linkage or a substituted group that acts as an electron bridge between the donor and acceptor groups [17, 45].

2. EXPERIMENTAL

The structures of the compounds investigated were optimized using DFT computations. The G09 program was used for the calculations [46-52]. Frequency calculations were done after optimization to verify the potential energy surface's minimal energy structure. TD-DFT computations were used to obtain the electronic absorption spectra for the twenty-five lowest singlet vertical excitations [46, 53]. Numerous studies have demonstrated that different functionals can accurately predict the organic compounds absorption spectra [46, 54-56].

All computations in this work were performed using Gaussian 09W, one of the most extensively used package programs in computational chemistry, and GaussView 05, a graphical interface software in molecular modeling. During the assignment method, the vibrational movements evaluated using GaussView were also taken into account [57].

The DFT was used to perform shape optimization and frequency calculations on molecules in their ground states (S0). The frequency analysis revealed that the optimized structures were real minima. The equilibrium geometries of the molecules were optimized using the TD-DFT technique in the first excited singlet state. Based on the optimized structures in S0 and S1,

the TD-DFT approach was used to model the absorption and fluorescence spectra. Various functionals were utilized to optimize the geometry of compound in S0 and S1, with the objective of finding a suitable technique. B3LYP, CAM-B3LYP and WB97XD were just a few of the functionals that were present. [50, 58-61].

All structures were first optimized using hybrid functional methods (DFT/B3LYP, CAM-B3LYP, and WB97XD). Frequency calculations of the optimized structures were performed. The ground states, which should not occur with negative frequency, were tested. 6-311+G(d,p) was calculated in basic basis sets for the hybrid functional methods used for all structures. Pyridoquinolizine, which has π-groups, and different bridging groups that facilitate conjugation, such as ethene, benzene, furane, thiophene, and their derivatives, have been used.

PQ
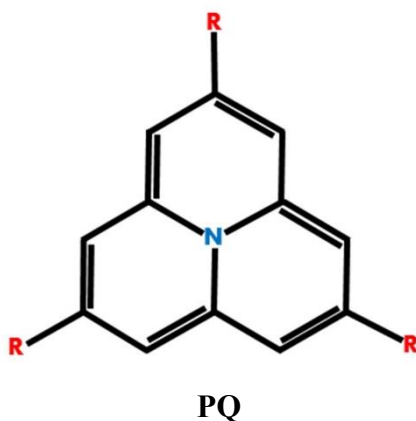
Figure 2.1. OLED-based donor group molecular structure designed based on pyridoquinolizine (PQ).
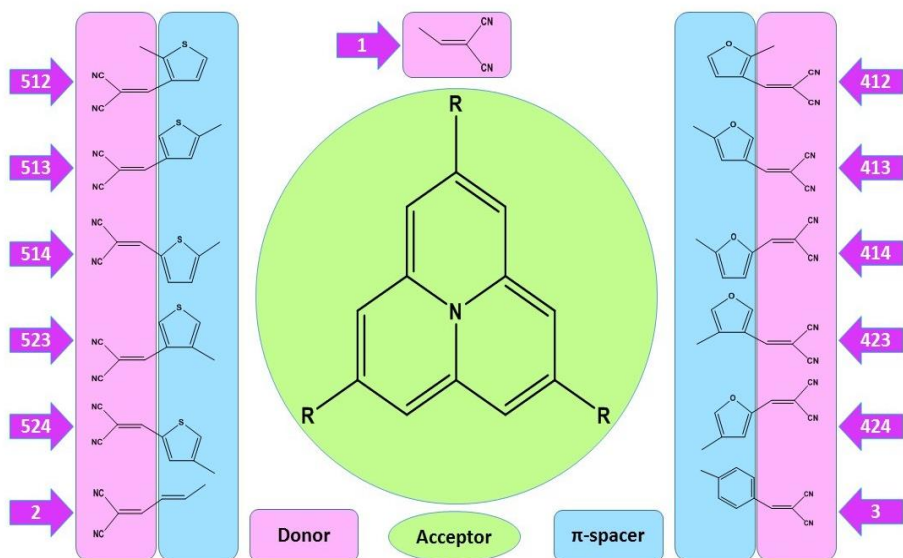
Figure 2.2. Functional group structures of various electron withdrawing groups based on 1, 2, 3, 412, 413, 414, 423, 424, 512, 513, 514, 523, and 524 Ethene, Benzene, Furan, and Thiophene derivatives. The acceptor group was selected to be the electron withdrawing cyano group.

3. RESULTS AND DISCUSSION

3.1. Molecular design and characterization

Using pyrazine and quinoxaline acceptors, a number of innovative D-A and D-π-A push-pull systems are compared. Different electron-donating triphenylamine and carbazole moieties are present in these complexes. The electrochemical and photophysical characteristics differed significantly depending on the molecule structure. D-π-A structures can help in the creation of high-efficiency emitters since these push-pull systems often display strong intramolecular charge-transfer (ICT) emission and their optoelectronic characteristics are easily changeable by modifying the electron donor and/or acceptor strengths. [5, 62, 63]. The computational analysis, which was carried out using the DFT method, will present new data. Through the application of the 6-31G+(d) basis set and the B3LYP theory level, quantum chemical descriptors were established [64]. Using the 6-31G(d,p) basis set and a hybrid functional approach called B3LYP, the structures of both compounds were optimized, and a number of structural parameters were investigated [65].

Density functional theory calculations of molecular orbitals (B3LYP, B2PLYP, CAM-B3LYP, and WB97XD), which also provided energetic and electron density characterization, were compared to the measured rotational parameters. The dimer is a useful case study for comparing dispersion-corrected computational techniques with conformational search strategies due to its narrow potential energy surface [66]. Designing and synthesizing donor-acceptor molecular systems using a bridged framework is currently one of the most effective methods for optoelectronic materials [50, 67, 68].

A complete conformational research was conducted to the ground states of all the structures analyzed in the study. Optimizations of the ground state were carried out at 6-311+G(d,p) [69]. For calculations of excited states, different functions were tested by combining the 6-311+G(d,p) basis set, including B3LYP, CAM-B3LYP, and WB97XD. This is important in terms of structural and electronic properties for highly conjugated systems. The investigation of both its electronic and structural properties has been studied theoretically at the DFT level. The unit of pyridoquinolizine acts as a donor. The acceptor part has been formed by strong electron-withdrawing cyanides. Furthermore, an ethene-based π system, benzene, furan, thiophene derivatives, and various electron-withdrawing bridge groups, pyridoquinolizine, connected to different positions, was formed. The donor and acceptor formed in the structure were connected to each other. The compounds exhibit a high electron conjugation overall. Organic compounds designed as D-π-A exhibit important optical and photophysical properties. D-π-A molecules are often utilized in molecular electronics, and it is interesting how their properties can be used and investigated. The -electronic characteristics of molecular D-π-A molecules have piqued the interest of solid-state scientists, as have their prospective technological improvements in organic electronics. Potential TADF emitters in this work of the D-π-A type were obtained by combining some π-bridged acceptor donors. Structural and electronic properties of all molecule, three different hybrid functionals; DFT/B3LYP/6-311+G(d,p), DFT/CAM-B3LYP/6-311+G(d,p), and DFT/WB97XD/6-311+G(d,p). It is calculated theoretically at the DFT and TD-DFT levels by applying +G(d,p).

In addition, chemical modification of the acceptor, donor, and bridge parts can effectively influence electronic energy levels, absorption and emission spectra, intermolecular stacking, and film shape. [50, 70, 71].

A number of theoretically studied TADF structures based on pyridoquinolizine were computationally examined in terms of structural and photophysical characteristics in this work. A number of descriptors, such as singlet-triplet energy gaps, have been identified to evaluate TADF activities: HOMO-LUMO energy difference, and HOMO-LUMO energy level structures and orbital distributions are optimised [72]. Literature data showed that the system is in the semiconductor band gap between $\Delta E = 0.5$ and 4 eV [73]. HOMO-LUMO overlap and π delocalization are caused by the molecular structure's flexibility and free rotation. The locally segregated donor and acceptor groups disrupted π-conjugation, leading to segregated HOMO and LUMO energy levels, which resulted in the formation of ICT. As a result, ICT has facilitated the reverse intersystem crossover (RISC) process necessary for effective TADF emission. ΔEST is directly related to HOMO-LUMO overlap, so in almost all cases, compounds exhibiting HOMO-LUMO overlap were also obtained with high ΔEST values.

3.2. Energy gap (Δ*E*)

The calculations revealed that the energy values for pyridoquinolizine's cross-border energy gap fit within the semiconductor group. The addition of strong electron-drawing cyanide acceptor groups and junctions between D-π-A contributed in a broadening of the π-electrons conjugation. This resulted in a reduction of the band gaps in the HOMO-LUMO energy levels observed in all results. Therefore, compounds resulting from band narrowing at HOMO-LUMO energy levels have become semiconductors. The highest ΔE values for pyridoquinolizine were obtained at 1.8653 eV, and the lowest energy values for pyridoquinolizine were obtained at 1.0888 eV in Table 3.1.

Table 3.2.1. Calculation results of designed molecules based on PQ

Molecule No.	DFT B3LYP/6-311+G(d,p)			
	Energy(au)	$E_{HOMO(eV)}$	$E_{LUMO(eV)}$	$\Delta E_{(eV)}$
PQ	**-517.5450**	**-4.0384**	**-1.8049**	**2.2335**
PQ_1	-1303.3566	-5.6415	-4.3982	1.2433
PQ_2	-1535.6425	-5.4156	-4.1625	1.2530
PQ_3	-1996.7013	-4.9731	-3.6545	1.3186
PQ_412	-1990.0491	-5.2752	-3.8156	1.4596
PQ_413	-1990.0542	-4.9740	-3.2874	1.6865
PQ_414	-1990.0805	-4.7876	-3.6988	1.0888
PQ_423	-1990.0322	-5.1783	-3.3130	1.8653
PQ_424	-1990.0491	-5.1489	-3.4120	1.7369
PQ_512	-2958.9891	-5.3247	-3.6852	1.6395
PQ_513	-2958.9927	-5.0861	-3.4205	1.6656
PQ_514	-2959.0032	-5.0921	-3.8439	1.2482
PQ_523	-2958.9852	-5.1274	-3.2958	1.8316
PQ_524	-2958.9953	-5.0746	-3.4572	1.6174

Thus, in terms of HOMO-LUMO energy difference ($\Delta E = E_{LUMO} - E_{HOMO}$), the structures with D-π-A architectures (PQ_1, PQ_2, PQ_3, PQ_412, PQ_413, PQ_414, PQ_223, and PQ_524) were determined to be suitable for OLED.

3.3. HOMO and LUMO energy levels

Using DFT and TD-DFT methodologies, the effects of changing two fixing groups and five donor groups on the geometries and optoelectronic characteristics of twelve organic dyes with D-A structures are explored. [46]. For calculations involving quantum chemistry, the parameters HOMO and LUMO are crucial. The molecules' interactions with one another can be determined. They are therefore referred to as the frontier orbitals. The outermost orbital that contains electrons, known as HOMO, has a tendency to give these electrons away by acting as an electron donor. However, LUMO can be considered the innermost orbital that is prepared to receive electrons [74, 75].

The primary strategy to achieve higher efficiency may be to adjust the energy levels of HOMO and LUMO through chemical adaptation. The computed difference between the HOMO and LUMO energy levels dictates the light absorption sites in this technique. The HOMO and LUMO energy diagrams give critical information on reactivity as well as the planned structure. Therefore, it is very important to investigate boundary molecular orbitals. Knowing the atoms and atomic groups that contribute to the boundary molecular orbitals makes significant contributions to the elucidation of the structures. Reactivity centers are determined with the help of these visuals. For structures to be potential OLED candidates for TADF, separate HOMO and LUMO images must be obtained. This requires the energy of change and is critically important. The steric hindrance that causes bending between the donor and acceptor groups underscores this critical importance. In Table 3.2.2., the HOMOs of the pyridoquinolizine-based components are predominantly dispersed on the pyridoquinolizine structures. LUMOs are generally located on the acceptor nucleus. This is one of the main criteria to be achieved for OLED structures. In addition, LUMOs consist of cyano groups that attract attention with their electron-withdrawing properties. Therefore, mostly HOMO and LUMO-LUMO+1 orbitals are clearly distributed in the D-π-A parts of the structures in Tables 3.2.2, 3.2.3, and 3.2.4.

Table 3.2.2. Molecule no., GSG, HOMO, and LUMO diagrams of designed OLEDs
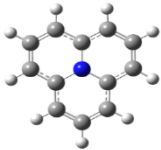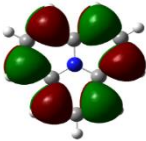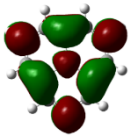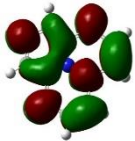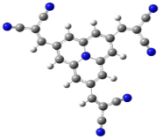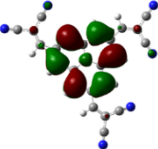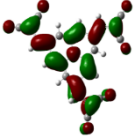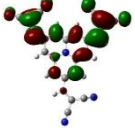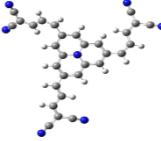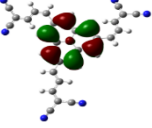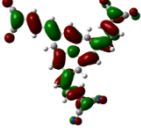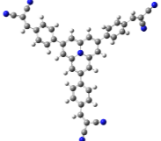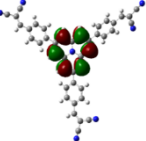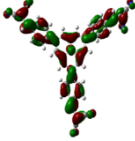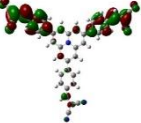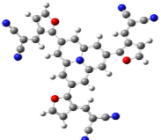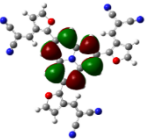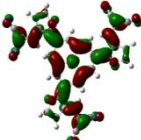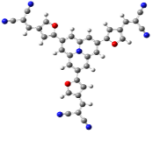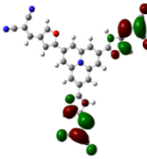
Molecule No.	GSG	HOMO	LUMO	LUMO+1
PQ				
PQ_1				
PQ_2				
PQ_3				
PQ_412				
PQ_413				

Table 3.2.3. Molecule no., GSG, HOMO, and LUMO diagrams of designed OLEDs (continuete)
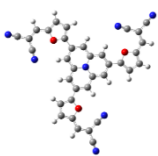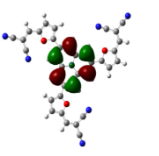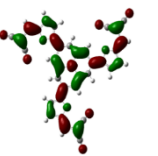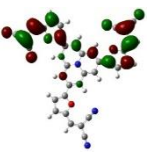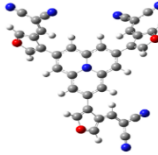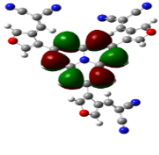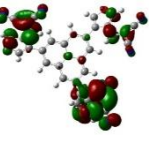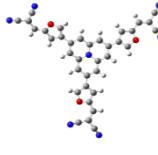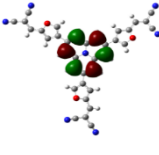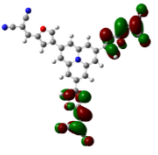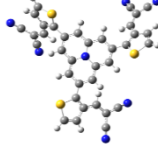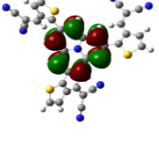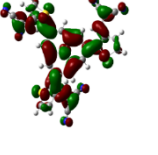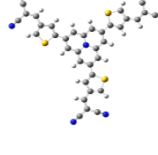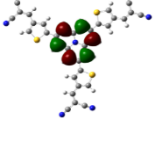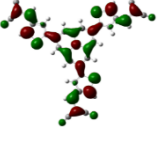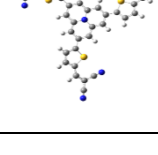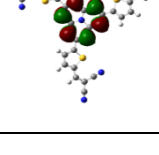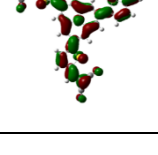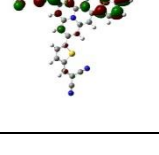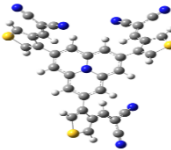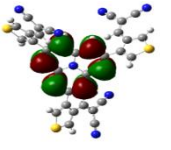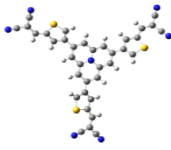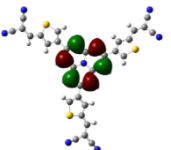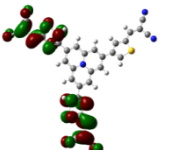
Molecule No.	GSG	HOMO	LUMO	LUMO+1
PQ_414				
PQ_423				
PQ_424				
PQ_512				
PQ_513				
PQ_514				

Table 3.2.3. Molecule no., GSG, HOMO, and LUMO diagrams of designed OLEDs (continuete)

Molecule No.	GSG	HOMO	LUMO	LUMO+1
PQ_523				
PQ_524				

For all designed compounds, the acceptor group remained unchanged as cyano, while the π system and the donor group were modified to investigate the effect on the electronic structure. Extended conjugation was provided for all compounds. Bends in planarity are predicted in some circumstances due to the steric barrier of the acceptor units. The structures are intended as organic systems of the D-π-A type. It was determined that all structures have a clear distribution of donor-acceptor parts in terms of HOMO and LUMO-LUMO+1 orbitals in Tables 3.2, 3.3, and 3.4. It has been determined that π groups between D-π-A play an important role, especially for HOMO and LUMO energy levels.

3.4. Singlet and triplet states (ΔE_{ST})

The process of upconverting excitons from triplets to singlets is facilitated by a smaller ΔE_{ST}. This could improve device efficiency [28, 76-78]. For TADF OLEDs, emitter selection determines key device characteristics such as efficiency, lifetime, and color purity [28]. In general, if ΔE_{ST} is above 0.3 eV, the likelihood of RISC occurs is lower. [79-81].

TADF emitters have typically been observed to have a small ΔE_{ST} below 0.2 eV between singlet and triplet excited states to reach RISC. The lowest or equal energy difference between the singlet and triplet states is one of the first and most essential aims for the design of TADF molecules for OLEDs. The

clear separation of the HOMO and LUMO boundary molecular orbitals resulted in narrower ΔE_{ST} values. This method was also used, together with the calculated ΔE_{ST} values, to determine the best-performing DFT function for excited-state calculations. The singlet and triplet states of the structures made with three different hybrid functionals, B3LYP, CAM-B3LYP, and WB97XD, are in good accord with the published data. Table 3. 5 shows that according to B3LYP, PQ_2, PQ_3, PQ_413, PQ_423, PQ_424, PQ_512, PQ_513, PQ_514, PQ_523, and PQ_524, there are 10 structures in total; according to CAM-B3LYP, PQ_1, PQ_3, PQ_412, PQ_412, PQ_423, PQ_424, PQ_512, PQ_513, PQ_514, PQ_523, and according to WB97XD, PQ_2, PQ_3, PQ_412, PQ_423, PQ_424, PQ_512, PQ_513, PQ_513, PQ_514, PQ_523, and PQ_524, a total of 10 D-π-A type potential OLED structures.

Table 3.4.1. ΔE_{ST} calculation results of designed molecules based on PQ

Molecule No.	TD-DFT (ΔE_{ST}) 6-311+G(d,p)		
	B3LYP (eV)	**CAM-B3LYP** (eV)	**WB97XD** (eV)
PQ	**0.1917**	**0.2433**	**0.2237**
PQ_1	0.3421	0.2740	0.3595
PQ_2	0.2963	0.4066	0.2925
PQ_3	0.1421	0.2346	0.2245
PQ_412	0.4388	0.2721	0.2573
PQ_413	0.2100	0.3603	0.3224
PQ_414	0.3056	0.3551	0.3308
PQ_423	0.0212	0.2433	0.2269
PQ_424	0.1864	0.2516	0.2288
PQ_512	0.1921	0.2744	0.2586
PQ_513	0.1769	0.2904	0.2655
PQ_514	0.1585	0.2409	0.2300
PQ_523	0.0101	0.2447	0.2286
PQ_524	0.1780	0.6559	0.2240

The D-π-A type potential OLED structure and the structures that do not meet the ΔEST literature values are determined as 3 structures in total as PQ_1, 412, and PQ_414 according to B3LYP, 4 structures in total as PQ_2, PQ_413, PQ_414, and PQ_524 according to CAM-B3LYP, and 3 structures in total as PQ_1, PQ_413, and PQ_414 according to WB97XD.
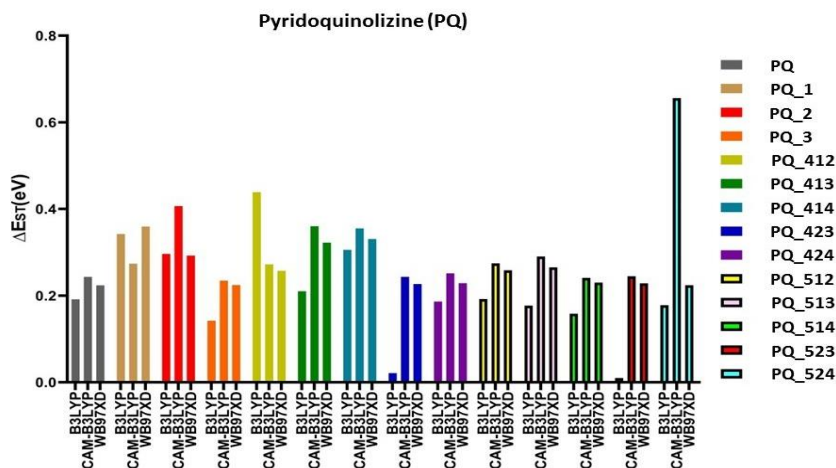

Figure 3.4.1. Table of ΔEST programming results of PQ designed molecules in B3LYP, CAM-B3LYP, and WB97XD (GraphPad Prism 8).

Common overlapping structures in ΔEST literature data of three different hybrid functionals, B3LYP, CAM-B3LYP, and WB97XD; a total of seven D-π-A type potential OLED structures were evaluated as PQ_3, PQ_423, PQ_424, PQ_512, PQ_513, PQ_514, and PQ_523. If the three different hybrid functionals B3LYP, CAM-B3LYP, and WB97XD are not compatible with the ΔEST literature data; a total of 1 D-π-A type potential OLED structure, PQ_414, is not considered.

4. CONCLUSION

In conclusion, before applying the theoretical procedures, fluorescent organic materials or molecules with the potential to be candidates for organic light-emitting diodes are identified. In addition, it is expected to shed light on and contribute to theoretical chemistry studies in the field. The molecules

designed in this study have a very small energy gap between the singlet-triplet states and have been shown to have the potential to be OLED structures. This method, together with the calculated ΔEST values, was used to determine the best-performing DFT function for excited state calculations. While determining the most suitable OLED compounds according to the theoretical data, the relationship between TADF activity was investigated based on pyridoquinolizine derivatives.

As a result, it has been observed that molecular structures largely govern TADF activity, and this study has shown that high TADF yields can be achieved by using donor structures such as pyridoquinolizine in molecular design. The theoretical results of the computational methods applied in this study showed that they obtained a good yield. These findings are predicted to shed light on the design modifications of more suitable and new TADF structures to be used in OLEDs, and with the help of the computational methods used, new and efficient TADF emitter OLEDs can be proposed. Subsequently, the structure-specific relationship of these new molecules will be investigated to provide more comprehensive information for synthesizing higher-efficiency OLED materials.

ACKNOWLEDGMENTS

REFERENCES

1. Bella, A. P., Panneerselvam, M., Vedha, S. A., Jaccob, M., Solomon, R. V., & Merlin, J. P. (2019). *Computational Materials Science, 162*, 359-369.

2. Zhang, J., Xu, L., & Wong, W.-Y. (2018). *Coordination Chemistry Reviews, 355*, 180-198.

3. Solomon, R. V., Jagadeesan, R., Vedha, S. A., & Venuvanalingam, P. (2014). *Dyes and Pigments, 100*, 261-268.

4. Ganesan, P., Yella, A., Holcombe, T. W., Gao, P., Rajalingam, R., Al-Muhtaseb, S. A., Grätzel, M., & Nazeeruddin, M. K. (2015). *ACS Sustainable Chemistry & Engineering, 3*, 2389-2396.

5. Verbitskiy, E. V., Kvashnin, Y. A., Bogdanov, P. I., Medvedeva, M. V., Svalova, T. S., Kozitsina, A. N., Samsonova, L. G., Degtyarenko, K. M., Grigoryev, D. V., & Kurtcevich, A. E. (2021). *Dyes and Pigments, 187*, 109124.

6. Nosova, E. V., Achelle, S., Lipunova, G. N., Charushin, V. N., & Chupakhin, O. N. (2019). *Russian Chemical Reviews, 88*, 1128.

7. Mortimer, R. J. (1997). *Chemical Society Reviews, 26*, 147-156.

8. Ha, T. H., Bin, J.-K., & Lee, C. W. (2022). *Organic Electronics, 102*, 106450.

9. Ho, S., Liu, S., Chen, Y., & So, F. (2015). *Journal of Photonics for Energy, 5*, 057611-057611.

10. Wong, M. Y., & Zysman-Colman, E. (2017). *Advanced Materials, 29*, 1605444.

11. Karzazi, Y. (2014). *Journal of Materials and Environmental Science, 5*, 1-12.

12. Raupp, S., Merklein, L., Pathak, M., Scharfer, P., & Schabel, W. (2017). *Chemical Engineering Science, 160*, 113-120.

13. Liu, Y.-F., Feng, J., Zhang, Y.-F., Cui, H.-F., Yin, D., Bi, Y.-G., Song, J.-F., Chen, Q.-D., & Sun, H.-B. (2014). *Organic Electronics, 15*, 478-483.

14. Wu, X., Li, F., Wu, W., & Guo, T. (2014). *Applied Surface Science, 295*, 214-218.

15. Irak, Z. T., Gümüs, A., & Gümüs, S. (2019). *Journal of the Chilean Chemical Society, 64*, 4303-4309.

16. Xiao, L., Chen, Z., Qu, B., Luo, J., Kong, S., Gong, Q., & Kido, J. (2011). *Advanced Materials, 23*, 926-952.

17. Endo, A., Sato, K., Yoshimura, K., Kai, T., Kawada, A., Miyazaki, H., & Adachi, C. (2011). *Applied Physics Letters, 98*.

18. Zhang, D., Duan, L., Zhang, D., & Qiu, Y. (2014). *Journal of Materials Chemistry C, 2*, 8983-8989.

19. Brooks, J., Babayan, Y., Lamansky, S., Djurovich, P. I., Tsyba, I., Bau, R., & Thompson, M. E. (2002). *Inorganic Chemistry, 41*, 3055-3066.

20. Lamansky, S., Djurovich, P., Murphy, D., Abdel-Razzaq, F., Lee, H.-E., Adachi, C., Burrows, P. E., Forrest, S. R., & Thompson, M. E. (2001). *Journal of the American Chemical Society, 123*, 4304-4312.

21. Uoyama, H., Goushi, K., Shizu, K., Nomura, H., & Adachi, C. (2012). *Nature, 492*, 234-238.

22. Masui, K., Nakanotani, H., & Adachi, C. (2013). *Organic Electronics, 14*, 2721-2726.

23. Adachi, C., Baldo, M. A., Thompson, M. E., & Forrest, S. R. (2001). *Journal of Applied Physics, 90*, 5048-5051.

24. Adachi, C. (2014). *Japanese Journal of Applied Physics, 53*, 060101.

25. Salehi, A., Fu, X., Shin, D. H., & So, F. (2019). *Advanced Functional Materials, 29*, 1808803.

26. Huang, Y., Hsiang, E.-L., Deng, M.-Y., & Wu, S.-T. (2020). *Light: Science & Applications, 9*, 105.

27. Nakagawa, T., Ku, S.-Y., Wong, K.-T., & Adachi, C. (2012). *Chemical Communications, 48*, 9580-9582.

28. Li, S., Li, M., Hua, L., Zhang, T., & Ren, Z. (2023). *Dyes and Pigments, 220*, 111671.

29. Levy, D. H. (1980). *Annual Review of Physical Chemistry, 31*, 197-225.

30. Schermann, J.-P. (2007). *Spectroscopy and Modeling of Biomolecular Building Blocks*. Elsevier.

31. Jeffrey, G. A., & Jeffrey, G. A. (1997). *An Introduction to Hydrogen Bonding*. Oxford University Press.

32. Gilli, G., & Gilli, P. (2009). *The Nature of the Hydrogen Bond: Outline of a Comprehensive Hydrogen Bond Theory*. Oxford University Press.

33. Del Bene, J., Alkorta, I., Elguero, J., & Scheiner, S. (2015). *Springer: New York, 19*, 191-263.

34. Scheiner, S. (1997). *Hydrogen Bonding: A Theoretical Perspective*, Topics in Physical Chemistry.

35. Liu, Y., Du, B., Han, X., Wu, X., Tong, H., & Wang, L. (2022). *Chemical Engineering Journal, 446*, 137372.

36. Huang, T., Jiang, W., & Duan, L. (2018). *Journal of Materials Chemistry C, 6*, 5577-5596.

37. Im, Y., Kim, M., Cho, Y. J., Seo, J.-A., Yook, K. S., & Lee, J. Y. (2017). *Chemistry of Materials, 29*, 1946-1963.

38. Yang, Z., Mao, Z., Xie, Z., Zhang, Y., Liu, S., Zhao, J., Xu, J., Chi, Z., & Aldred, M. P. (2017). *Chemical Society Reviews, 46*, 915-1016.

39. Wu, T.-L., Huang, M.-J., Lin, C.-C., Huang, P.-Y., Chou, T.-Y., Cheng, R.-W., Lin, H.-W., Liu, R.-S., & Cheng, C.-H. (2018). *Nature Photonics, 12*, 235-240.

40. Ahn, D. H., Kim, S. W., Lee, H., Ko, I. J., Karthik, D., Lee, J. Y., & Kwon, J. H. (2019). *Nature Photonics, 13*, 540-546.

41. Cai, Z., Wu, X., Liu, H., Guo, J., Yang, D., Ma, D., Zhao, Z., & Tang, B. Z. (2021). *Angewandte Chemie, 133*, 23827-23832.

42. Ding, D., Wang, Z., Li, C., Zhang, J., Duan, C., Wei, Y., & Xu, H. (2020). *Advanced Materials, 32*, 1906950.

43. Gather, M. C., Köhnen, A., & Meerholz, K. (2011). *Advanced Materials, 23*, 233-248.

44. Saadh, M. J., Jasim, S. A., Dhiaa,

CHAPTER 6

COUMARIN–TRIAZOLE HYBRIDS AS EMERGING ANTICHOLINERGIC AGENTS

Prof. Dr. Ayşegül GÜMÜŞ[1]

---

[1] Bartin University, Faculty of Science, Department of Biotechnology, Bartın, Turkey, agumus@bartin.edu.tr, 0000-0002-1613-7074

1. INTRODUCTION

Molecular hybridization is a modern and effective strategy in drug design that combines two or more pharmacophoric units into a single hybrid molecule [1]. By merging bioactive fragments from natural or synthetic sources, this approach aims to produce new compounds with improved affinity, selectivity, and therapeutic efficacy compared with the parent drugs [2].

Hybrid molecules can be created by directly linking pharmacophores, merging overlapping structural features, or connecting them with cleavable or non-cleavable linkers [3]. These different designs allow researchers to tailor the biological activity, safety, and pharmacokinetic properties of the resulting compounds [4].

The main advantage of molecular hybridization is its ability to generate multi-target drug candidates. Such hybrid compounds may reduce side effects, overcome drug resistance, and offer dual or enhanced modes of action [5]. Because of these benefits, molecular hybridization has become an attractive tool in modern medicinal chemistry and an important approach for developing new drug prototypes.

Coumarins constitute an important class of oxygen-containing heterocyclic compounds characterized by a benzopyran-2-one core, and they occur widely in plants, microorganisms, and various natural sources [6]. Over the past decades, these scaffolds have gained significant attention due to their remarkable structural versatility and broad spectrum of biological activities. Numerous natural and synthetic coumarin derivatives have demonstrated potent pharmacological properties, including antimicrobial, antioxidant, anti-inflammatory, anticoagulant, anticancer, antiviral, and anti-HIV effects [7-10].

1,2,3-Triazoles have emerged as highly valuable nitrogen-rich heterocycles in modern medicinal chemistry, owing to their structural stability, versatile reactivity, and remarkable pharmacological potential [11]. Their unique five-membered ring system, which exists in distinct tautomeric forms, enables diverse patterns of interaction with biological targets and contributes to a broad spectrum of bioactivities, including antimicrobial, anticancer, antiviral, anti-inflammatory, antitubercular, antidiabetic, antimalarial, antileishmanial, and neuroprotective effects [12-13]. Advances in synthetic methodologies particularly the advent of copper-catalyzed azide–alkyne cycloaddition (CuAAC) and other click-chemistry-based strategies—have greatly facilitated

the efficient, high-yield, and sustainable construction of 1,2,3-triazole scaffolds, leading to an expanding library of hybrid molecules and conjugates with enhanced biological performance. The ability of the triazole ring to function as a robust, metabolically stable linker further broadens its utility in the design of multifunctional drug candidates. Additionally, the presence of multiple nitrogen atoms provides opportunities for diverse derivatization through N-amination, N-alkylation, and related functionalizations, enabling fine-tuning of physicochemical and pharmacodynamic properties [14]. These features have positioned 1,2,3-triazoles as a cornerstone of contemporary drug discovery, fostering interdisciplinary research efforts aimed at elucidating their structure–activity relationships and harnessing their therapeutic potential across numerous disease domains.

Alzheimer's disease (AD) is a progressive neurodegenerative disorder that poses a growing health challenge worldwide, particularly among the elderly [15]. Memory impairment is typically the earliest symptom, followed by language deficits, cognitive decline, disorientation, and loss of independence in daily activities. The pathogenesis of AD is multifactorial, involving cholinergic neuron degeneration, amyloid-beta (Aβ) aggregation, tau-mediated neurofibrillary tangles, oxidative stress, mitochondrial dysfunction, and imbalances in metal ions and neurotransmitters [16-17].

Current FDA-approved treatments, including acetylcholinesterase inhibitors such as donepezil, galantamine, and rivastigmine, provide only symptomatic relief and are limited by side effects and reduced long-term efficacy [18-20]. Consequently, the search for novel compounds with enhanced potency, selectivity, and safety remains a priority. Heterocyclic scaffolds have emerged as promising frameworks in this context, and hybrid molecules combining coumarin and 1,2,3-triazole motifs have attracted attention due to their structural versatility and potential anticholinergic activity [21-22]. These hybrids offer the possibility of multi-target interactions, making them attractive candidates for the development of next-generation AD therapeutics. Certain coumarin-based compounds incorporating a triazole ring have shown potential in the development of new derivatives with acetylcholinesterase inhibitory (AChEI) activity.

2. Synthesis and Anticholinesterase Activity of Coumarin-Triazole Hybrids

Dar et al. (2025) synthesized several ether-linked 3-acetyl triazole-substituted coumarin derivatives and evaluated their potentials as AChE inhibitors [23]. The synthetic route began with the preparation of 3-acetyl-7-hydroxycoumarin **2** via the condensation of 2,4-dihydroxybenzaldehyde **1** with ethyl acetoacetate (Scheme 1). After alkylation of the phenolic hydroxyl group, the resulting acetylated 7-hydroxycoumarin substrate **3** was subjected to a 1,3-dipolar (Huisgen) cycloaddition with various aromatic azides under Sharpless click-chemistry conditions, affording sixteen novel coumarin-tethered 1,2,3-triazole derivatives **4a-p**.
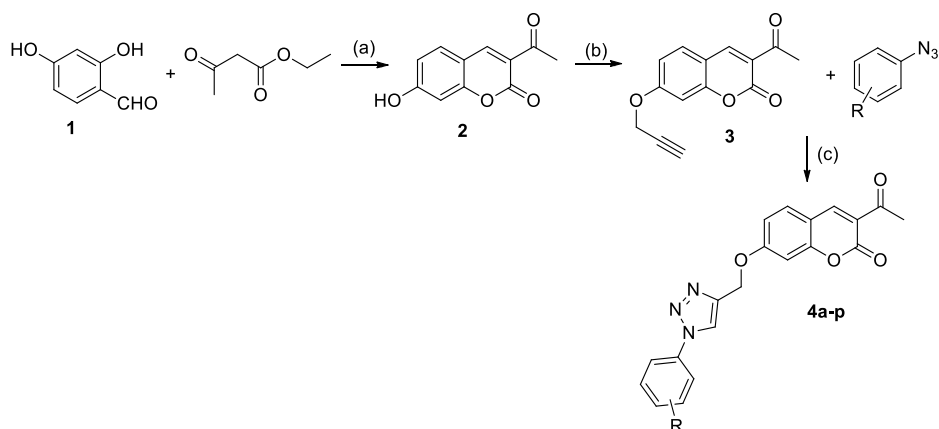
Scheme 1. Synthesis of coumarin-triazole-benzene derivatives [23]. a) piperidine, reflux; b) propargyl bromide, K_2CO_3, acetonitrile; c) $CuSO_4$, sodium ascorbate, t-BuOH:water (1:1).

Among the synthesized coumarin derivatives, compound **4i** demonstrated the strongest inhibitory effect (IC_{50} = 2.18 µM) and exhibited mixed-type inhibition kinetics (K_i = 8.13 ± 0.18 µM), indicating its capacity to interact with both the free enzyme and the enzyme–substrate complex [23] (Figure 1).
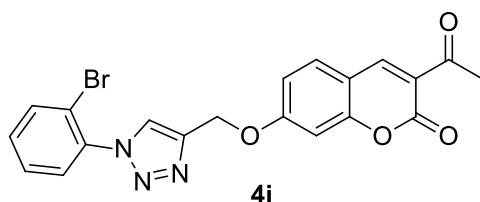
Figure 1. Coumarin-triazole derivative exhibiting most potent inhibition.

Pourabdi et al. (2022) synthesized a series of coumarin derivatives incorporating an N-benzyl-substituted 1,2,3-triazole moiety and demonstrated their potential as promising multifunctional candidates for Alzheimer's disease therapy [24]. Intermediate **8** was obtained by hydrolyzing compound **7**, which had been synthesized through the Perkin condensation of substituted 2-hydroxybenzaldehydes (**5**) with 2-(4-hydroxyphenyl)acetic acid (**6**) (Scheme 2). Subsequent alkylation of the resulting 3-(4-hydroxyphenyl)-2H-chromen-2-one derivatives (**8**) with propargyl bromide afforded the propargylated coumarins (**9**). Finally, copper-catalyzed azide–alkyne cycloaddition (CuAAC) using in situ–generated benzyl azides enabled the regioselective construction of the coumarin-linked 1,2,3-triazoles (**10a-w**).
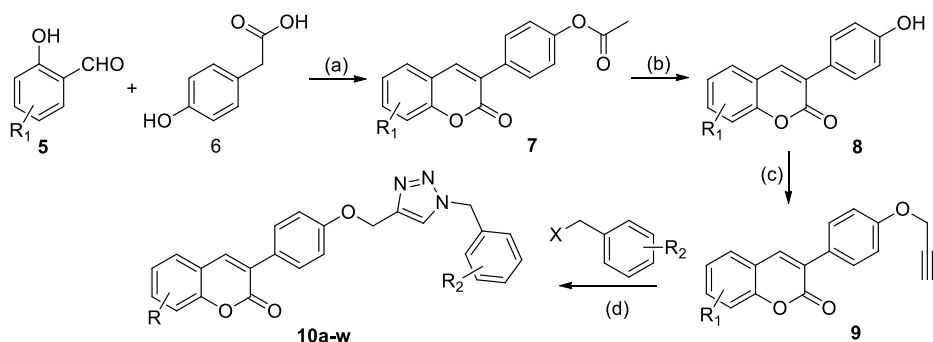
Scheme 2. Synthesis of arylcoumarin-N-benzyltriazole derivatives [24]. Reagents and conditions: (a) KOAc, Ac$_2$O, reflux, 4 h; (b) HCl (2N), MeOH, reflux, 3 h; (c) Propargyl bromide, K$_2$CO$_3$, DMF, 60–65°C, 4 h; and (d) sodium ascorbate (NaAs), CuSO$_4$, t-BuOH:water (1:1), rt, 4 h.

In vitro cholinesterase inhibition studies demonstrated that the synthesized 3-arylcoumarin-based triazole derivatives exhibit higher affinity toward BuChE than AChE. The nature and position of substituents on the coumarin scaffold

played a decisive role in modulating activity, with compounds **10r** and **10v** emerging as the most potent BuChE inhibitors (Figure 2).
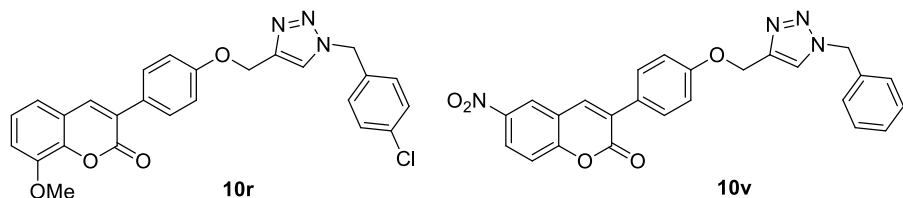

Figure 2. Arylcoumarin-N-benzyltriazole derivatives exhibiting most potent inhibition.

Dimkovski et al. (2025) reported the design and synthesis of a series of 21 coumarin–triazole–isatin hybrid molecules, developed as potential multitarget agents for Alzheimer's disease [25]. In this library, structural diversity was introduced through variations in the alkyl linker length between the coumarin and triazole moieties, as well as through different substituents at the 5-position of the isatin ring. The synthetic route commenced with the formation of O-bromoalkyl coumarin intermediates **12** via the reaction of 4-hydroxycoumarin with dibromoalkanes (Scheme3). These intermediates subsequently underwent S_N2 substitution with sodium azide to generate the corresponding O-azidoalkyl coumarins **13**. In a parallel step, isatin derivatives **14** were propargylated through an SN2 alkylation, affording the required N-propargyl isatins **15**. The final coumarin–triazole–isatin hybrids **16a-v** were assembled through a copper(I)-catalyzed azide–alkyne cycloaddition (CuAAC).
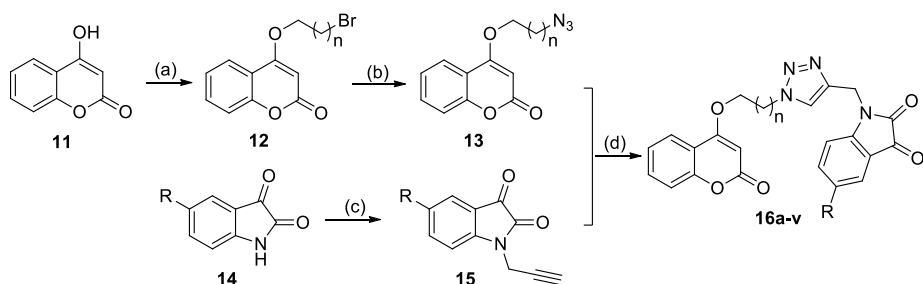
Scheme 3. Synthesis of coumarin–triazole–isatin hybrid molecules [25]. Reagents and conditions: (a) propargyl bromide, K_2CO_3, DMF, 4 h, rt; (b) dibromo alkane, K_2CO_3,

DMF, 6 h, rt; (c) NaN_3, DMF, 4 h, rt; (d) $CuSO_4$, sodium ascorbate, DMF, distilled water, 0.5–2 h, rt.

Biological evaluation showed that several hybrids exhibited strong inhibitory activity against BChE with clear selectivity over AChE. Among them, compound **16o** proved to be the most potent BChE inhibitor ($IC_{50} = 1.74$ µM), surpassing the activity of the reference drug donepezil (Figure 3).
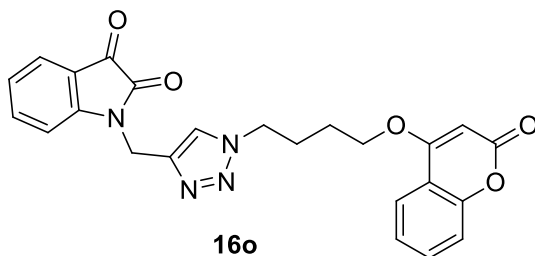

Figure 3. Coumarin–triazole–isatin hybrid molecule showing the highest activity.

Najafi et al. (2019) reported the design and synthesis of a novel series of tacrine–coumarin hybrids incorporating a 1,2,3-triazole linker, which were evaluated as potent dual-binding site cholinesterase inhibitors (ChEIs) for potential therapeutic application in Alzheimer's disease [26]. The target acridine–coumarin hybrids **24a–r** were synthesized through a multistep route (Scheme 4). Initially, 1,2,3,4-tetrahydroacridine derivatives **19** were prepared from anthranilic acid derivatives and cyclohexanone, followed by propargylation to yield **20**. Separately, 4-methyl-7-hydroxycoumarin and its analogs were converted into azido-functionalized intermediates **23** via alkylation and azidation. The final hybrids were obtained through a copper(I)-catalyzed azide–alkyne cycloaddition (CuAAC) between the propargylated acridines and azido-coumarin derivatives.
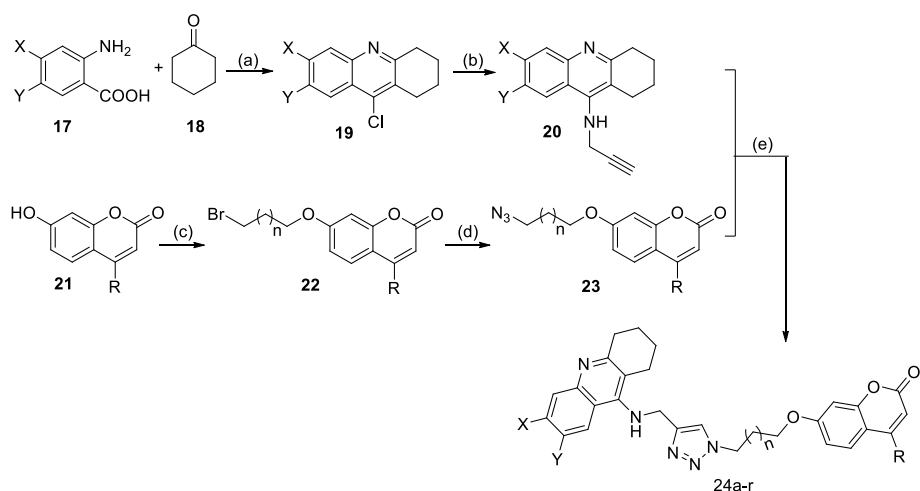
Scheme 4. Synthesis of tacrine-coumarin hybrids [26]. Reagents and conditions: (a) POCl$_3$, reflux, 3 h; (b) Propagylamine, PhOH, 100 °C, 2 h; (c) dibromoalkanes, K$_2$CO$_3$, acetonitrile, reflux, 3–4 h; (d) NaN$_3$, ethanol, reflux, 3–4 h; (e) CuI, H$_2$O/t-BuOH, NEt$_3$, 12–24 h.

Among the synthesized tacrine–coumarin hybrids, compound **24e** exhibited the most potent anti-AChE activity (IC$_{50}$ = 27 nM), while compound **24m** showed the strongest anti-BChE activity (IC$_{50}$ = 6 nM), both surpassing the efficacy of the reference drugs tacrine and donepezil (Figure 4).
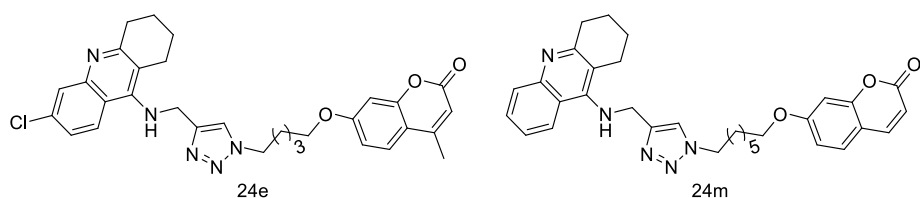

Figure 4. Tacrine–triazole–coumarin hybrid molecules exhibiting the highest activities.

Sharma ve Bharate (2023) synthesized a series of coumarin−triazole hybrids as potential multitargeted drug ligands (MTDLs) with better activity profiles [27]. The first series of coumarin–triazole (connected to A ring) hybrid **26a-p** was efficiently constructed starting from 4-hydroxycoumarin **11**, whose propargylation afforded the key intermediate 4-O-propargylated coumarin **25**.

Subsequent Cu(I)-catalyzed azide–alkyne cycloaddition with benzyl bromide derivatives provided a diverse set of triazole conjugates **26b-p** (Scheme 5).
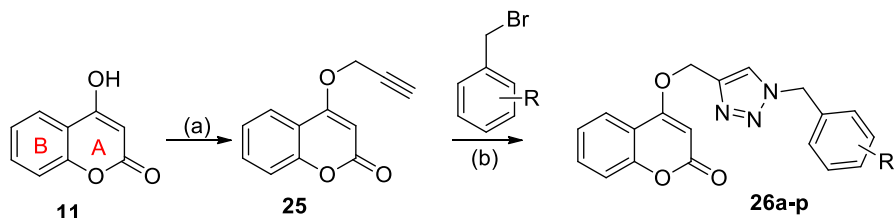
Scheme 5. Synthesis of coumarin A-ring connected triazole hybrids [7]. Reagents and conditions: (a) propargyl bromide, K_2CO_3, dimethylformamide (DMF), 70 °C, 24 h, reflux; (b) TEA, sodium ascorbate, $CuSO_4 \cdot 5H_2O$, rt, 24 h.

All synthesized coumarin triazoles **26a−p** were screened for inhibition of ChEs. The 3,5-dimethoxy-substituted analogue, **26o**, is the most active, with IC50 values of 2.76 for AChE and 3.30 for BChE (Figure 5). These findings clearly demonstrate that substituents on the triazole-benzyl ring are key structural determinants that decisively influence the inhibition profile of both enzymes.
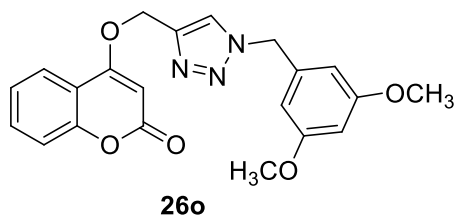

Figure 5. Coumarin-triazole hybrid molecule exhibiting the highest activities.

Sharma ve Bharate (2023) synthesized also a series of coumarin−triazole hybrids with triazole connected via the B-ring of coumarin (Scheme 6) [27]. Propargylation of 4-hydroxycoumarin **27** afforded the 4-O-propargylated coumarin **28**, which subsequently underwent a CuAAC 'click' reaction with various substituted benzyl bromides in the presence of sodium azide to furnish the corresponding triazole derivatives **28a–d**.
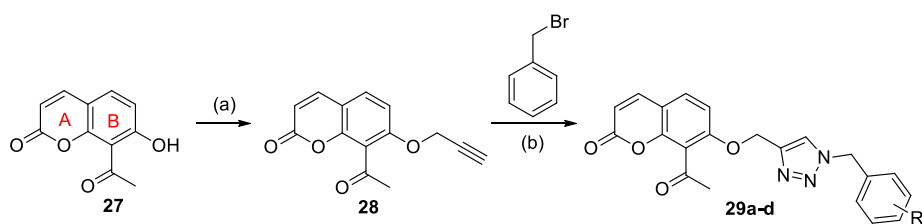
Scheme 6. Synthesis of coumarin B-ring connected triazole hybrids [27]. Reagents and conditions: (a) propargyl bromide, K_2CO_3, DMF, 70 °C, 24 h, reflux; (b) TEA, NaN_3, sodium ascorbate, $CuSO_4 \cdot 5H_2O$, rt, 24 h; (c) methyl iodide, NaH, DMF, 0 °C.

The biological evaluation demonstrated that B-ring–connected triazole hybrid **29b** bearing methoxy substituents exhibited markedly enhanced cholinesterase inhibition, achieving IC_{50} values of 2.57 ± 0.31 µM for AChE and 3.26 ± 0.13 µM for BuChE (Figure 6).
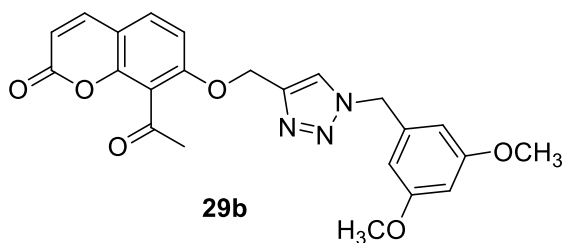
Figure 6. Coumarin-triazole hybrid molecule exhibiting the highest activities.

Bhagat et al. (2021) reported the synthesis of coumarin–triazole hybrids through a concise multistep sequence in which 4- and 7-hydroxycoumarin (**11** and **30**) were first propargylated, Substituted phenacyl bromides **32** were converted to their corresponding azides **33** and the resulting intermediates were finally coupled via a copper-catalyzed azide–alkyne cycloaddition to afford the desired triazole-linked coumarin derivatives **35a-e** and **36a-e** (Scheme 7) [28].
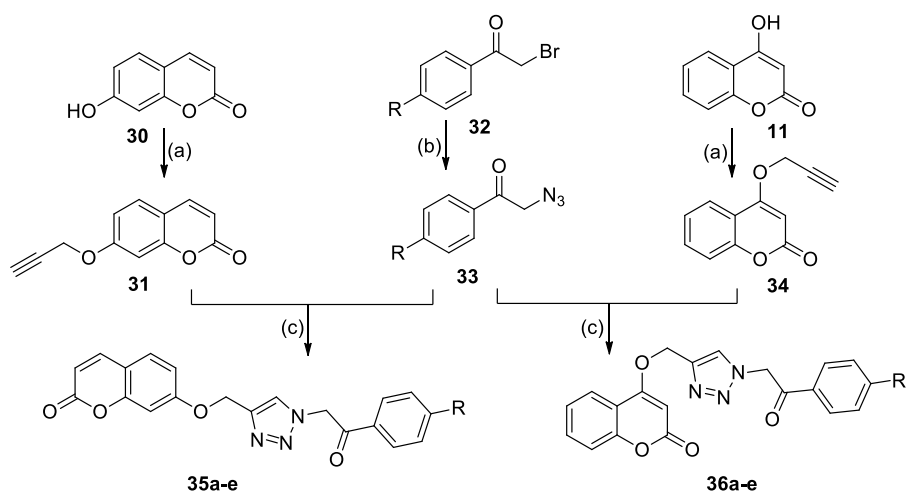
Scheme 7. Synthesis of coumarin–triazole–isatin hybrid molecules [28]. Reagents and conditions: (a) Propargyl bromide, K_2CO_3, DMF, 1-2 h, stir, rt; (b) NaN_3, DMF, 0.5-2 h, stir, rt; (c) sodium ascorbate, $CuSO_4$, DMF, 0.5-2 h, rt.

Compound **36a** showed most potent AChE inhibition against the enzyme that showed 96% inhibition at 1 μM concentration and exhibited IC50 value of 110 nM, which was found comparable to that of standard drug donepezil (Figure 7). The placement of electron-withdrawing substituents on the terminal benzoyl phenyl ring (F, Cl) resulted in notably stronger inhibitory activity compared to electron-donating groups (OCH_3, CH_3), indicating that substituent electronegativity plays a critical role in activity enhancement, following the order H < F < Cl < Br < CH_3 < OCH_3.

36a

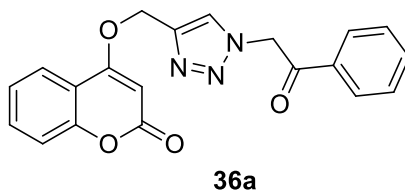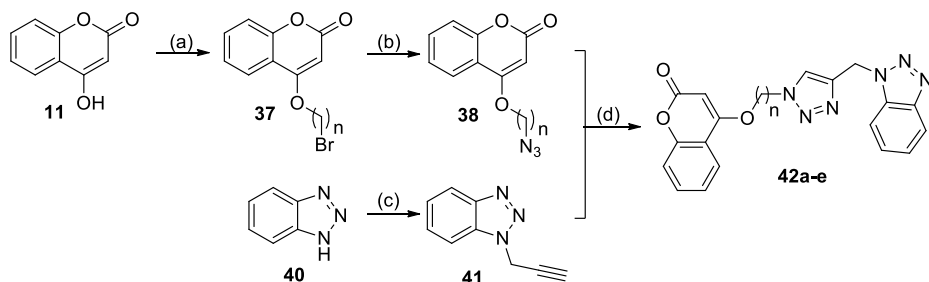**Figure 7.** Coumarin-triazole hybrid molecule exhibiting the highest AChE inhibition.

Singh et al. (2020) [29]. 7-Hydroxycoumarin **11** was first alkylated with various dibromoalkanes to afford alkylated coumarins **37**, which were subsequently converted to N-azidoalkyl coumarins **38** via substitution with sodium azide. In parallel, 1H-benzotriazole **40** was propargylated, and the

resulting propargylated derivative **41** was coupled with the prepared N-azidoalkyl coumarins through a click reaction to furnish a series of triazole-linked coumarin–benzotriazole hybrids **42a-e**.

Scheme 8. Synthesis of coumarin–benzotriazole hybrid molecules [29].

Among the AChE inhibitory compounds **13a-e**, compound **13b** (n = 3) exhibited the most potent AChE inhibition, with an IC_{50} value of 0.059 μM, which is comparable to that of donepezil (IC_{50} = 0.039 μM) (Figure 8).

42b
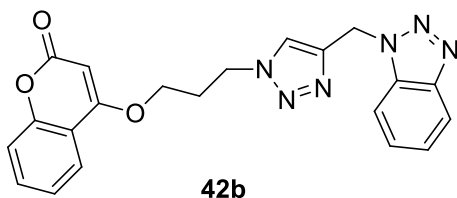
Figure 8. Coumarin-benzotriazole hybrid molecule exhibiting the highest AChE inhibition.

Nadur et al. (2025) synthesized a new series of 7-alkoxyamino-3-(1,2,3-triazole)- coumarins **48a-q** [30]. The synthesis began with the O-alkylation of 7-hydroxycoumarin (30) using a series of dibromoalkanes of varying chain lengths (Scheme 9) . Subsequent bromination at the 3-position of the coumarin core with Br_2 in a sodium acetate/acetic acid buffer proceeded via electrophilic substitution. Introduction of the acetylene moiety was achieved through a Sonogashira cross-coupling between intermediate **44** and trimethylsilyl acetylene, followed by base-mediated deprotection to afford alkynes **45**. These alkynes **46** then underwent Cu(I)-catalyzed 1,3-dipolar cycloaddition with phenyl or benzyl azides (R'N₃), yielding the corresponding 1,2,3-triazole

derivatives **47**. Finally, amination of the alkyl side chain with various cyclic amines afforded the target compounds **48a–q**.
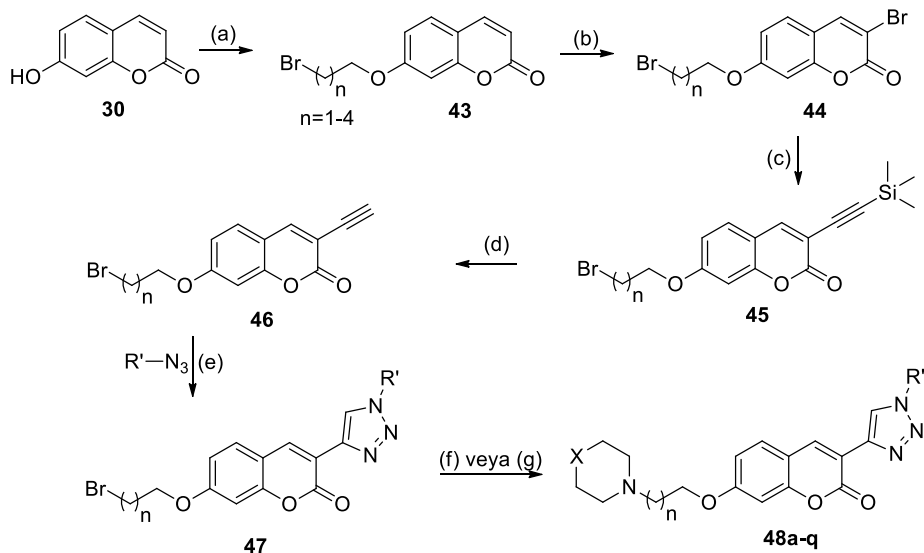
Scheme 9. Synthesis of 7-alkoxyamino-3-(1,2,3-triazole)- coumarin derivatives [30]. Reagents and conditions: (a) Br(CH$_2$)nBr (n=2–5), K$_2$CO$_3$, acetone, 60 °C, 6–12 h; (b) Br$_2$, AcOH, NaOAc, rt, 2 h; (c) trimethylsilylacetylene, PdCl$_2$ (PPh$_3$)$_2$, CuI, Et$_3$N, acetonitrile, 60 °C, 2 h; (d) K$_2$CO$_3$ methanol, rt, 1 h; (e) CuSO$_4$.5H$_2$O, ascorbic acid, rt, 24 h; (f) piperidine or methyl piperidine or methyl piperazine, acetonitrile, 60 °C, 4 h or (g) 1. piperazine-Boc, acetonitrile, 60 °C, 4 h, 83%; 2. TFA, dichloromethane, rt, 24 h.

According to activity results, the strong inhibitory profiles of compounds 1h (AChE IC$_{50}$ = 6.03 nM; H$_3$R K$_i$ = 558 nM), 1q (H$_3$R K$_i$ = 151 nM; AChE IC$_{50}$ = 1950 nM; MAO-B IC$_{50}$ = 1688 nM), and 1b (H$_3$R K$_i$ = 32 nM; AChE IC$_{50}$ = 1330 nM), together with their absence of neurotoxicity and noted neuroprotective effects, highlight this series as a promising model for developing new Multitarget-directed ligands MTDL candidates for Alzheimer's disease (Figure 9).

48b

48h

48q
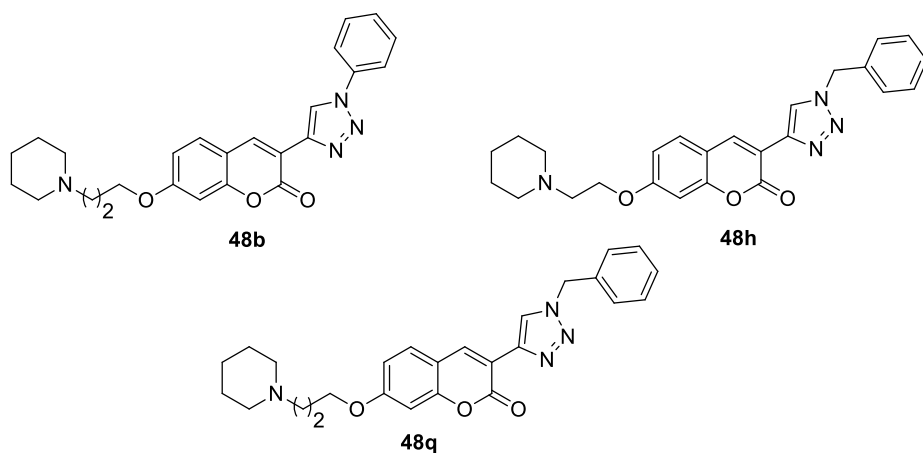
Figure 9. Alkoxyamino-triazole- coumarin hybrids exhibiting the highest inhibition.

3. CONCLUSION

In summary, coumarin represents a privileged and highly adaptable scaffold whose broad pharmacological profile and synthetic accessibility have supported the development of diverse molecular architectures, particularly coumarin–triazole hybrids.

The efficient construction of these hybrids has been largely driven by robust and reliable transformations including S_N2 substitution, bromination, Sonogashira coupling, and Cu(I)-catalyzed azide–alkyne cycloaddition which collectively enable precise functionalization at multiple positions of the coumarin nucleus. Strategic incorporation of electron-donating or electron-withdrawing substituents, variation of linker length, and the fusion of heterocyclic rings have proven essential for fine-tuning electronic distribution, reactivity, and structure–activity relationships. The resulting libraries of coumarin-based hybrids exhibit significant chemical diversity with generally high yields, operational simplicity, and broad applicability across synthetic schemes. Notably, many of these hybrids also demonstrated potent anti-cholinergic activity particularly AChE and BChE inhibition highlighting their strong potential as promising chemical templates for the development of future therapeutics targeting neurodegenerative disorders.

REFERENCES

1. de Sena Murteira Pinheiro, P.; Franco, L. S.; Montagnoli, T. L.; Fraga, C. A. M. Molecular Hybridization: A Powerful Tool for Multitarget Drug Discovery. *Expert Opin. Drug Discov.* **2024**, *19* (4), 451–470.

2. Ryad, N.; Elmaaty, A. A.; Ibrahim, I. M.; Ahmed Maghrabi, A. H.; Yahya Alahdal, M. A.; Saleem, R. M.; et al. Harnessing Molecular Hybridization Approach to Discover Novel Quinoline EGFR-TK Inhibitors for Cancer Treatment. *Future Med. Chem.* **2024**, *16* (11), 1087–1107.

3. Marchesi, E.; Perrone, D.; Navacchia, M. L. Molecular Hybridization as a Strategy for Developing Artemisinin-Derived Anticancer Candidates. *Pharmaceutics* **2023**, *15*, 2185.

4. Zimmermann, G. R.; Lehár, J.; Keith, C. T. Multi-Target Therapeutics: When the Whole Is Greater than the Sum of the Parts. *Drug Discov. Today* **2007**, *12*, 34–42.

5. Wang, H.; Pan, X.; Zhang, Y.; Wang, X.; Xiao, X.; Ji, C. MolHyb: A Web Server for Structure-Based Drug Design by Molecular Hybridization. *J. Chem. Inf. Model.* **2022**, *62* (12), 2916–2922.

6. Cao, D.; Liu, Z.; Verwilst, P.; Koo, S.; Jangjili, P.; Kim, J. S.; et al. Coumarin-Based Small-Molecule Fluorescent Chemosensors. *Chem. Rev.* **2019**, *119* (18), 10403–10519.

7. Widelski, J.; Luca, S.; Skiba, A.; et al. Isolation and Antimicrobial Activity of Coumarin Derivatives from Fruits of *Peucedanum luxurians* Tamamsch. *Molecules* **2018**, *23*, 1222.

8. Bisi, A.; Cappadone, C.; Rampa, A.; et al. Coumarin Derivatives as Potential Antitumor Agents: Growth Inhibition, Apoptosis Induction and Multidrug Resistance Reverting Activity. *Eur. J. Med. Chem.* **2017**, *127*, 577–585.

9. Yang, G.; Jin, Q.; Xu, C.; Fan, S.; Wang, C.; Xie, P. Synthesis, Characterization and Antifungal Activity of Coumarin-Functionalized Chitosan Derivatives. *Int. J. Biol. Macromol.* **2018**, *106*, 179–184.

10. Kumar, K. A.; Kalluraya, B.; Kumar, S. M. Synthesis and In Vitro Antioxidant Activities of Some Coumarin Derivatives Containing 1,2,3-

Triazole Ring. *Phosphorus Sulfur Silicon Relat. Elem.* **2018**, *193*, 294–299.

11. Rani, S.; Teotia, S.; Nain, S. Recent Advancements and Biological Activities of Triazole Derivatives: A Short Review. *Pharm. Chem. J.* **2024**, *57*, 1909–1917.

12. Bonandi, E.; Christodoulou, M. S.; Fumagalli, G.; Perdicchia, D.; Rastelli, G.; Passarella, D. The 1,2,3-Triazole Ring as a Bioisostere in Medicinal Chemistry. *Drug Discov. Today* **2017**, *22*, 1572–1581.

13. Marzi, M.; Zarenezhad, E. Triazole Compounds as Anti–Lung Cancer Agents: Focusing on Structure–Activity Relationship (SAR). *J. Mol. Struct.* **2025**, *1347*, 143221.

14. Opsomer, T.; Dehaen, W. Metal-Free Syntheses of N-Functionalized and NH-1,2,3-Triazoles: An Update on Recent Developments. *Chem. Commun.* **2021**, *57*, 1568–1590.

15. Alzheimer's Association. Alzheimer's Disease Facts and Figures. *Alzheimer's Dement.* **2019**, *15*, 321–387.

16. Ashrafian, H.; Zadeh, E. H.; Khan, R. H. Review on Alzheimer's Disease: Inhibition of Amyloid Beta and Tau Tangle Formation. *Int. J. Biol. Macromol.* **2021**, *167*, 382–394.

17. Huang, W. J.; Zhang, X.; Chen, W. W. Role of Oxidative Stress in Alzheimer's Disease. *Biomed. Rep.* **2016**, *4*, 519–522.

18. Riverol, M.; Slachevsky, A.; López, O. L. Efficacy and Tolerability of a Combination Treatment of Memantine and Donepezil for Alzheimer's Disease. *Eur. Neurol. J.* **2011**, *3*, 15–19.

19. Cummings, J. L.; Osse, A. M. L.; Kinney, J. W. Alzheimer's Disease: Novel Targets and Investigational Drugs for Disease Modification. *Drugs* **2023**, *83* (15), 1387–1408.

20. Se, T. E.; Fauzi, A.; Tang, Y. Q.; et al. A Review on Advances of Treatment Modalities for Alzheimer's Disease. *Life Sci.* **2021**, *276*, 119129.

21. Rohman, N.; Ardiansah, B.; Wukirsari, T.; Judeh, Z. Recent Trends in the Synthesis and Bioactivity of Coumarin, Coumarin–Chalcone, and Coumarin–Triazole Molecular Hybrids. *Molecules* **2024**, *29*, 1026.

22. Liu, W.; et al. Design, Synthesis and Biological Evaluation of Novel Coumarin Derivatives as Multifunctional Ligands for the Treatment of Alzheimer's Disease. *Eur. J. Med. Chem.* **2022**, *242*, 11468.

23. Dar, N. A.; Wani, O. H.; Wang, Y.; Khan, F. I.; Ganie, B. A.; Shah, S. W. A.; Dar, T. A.; Ismail, T. Novel Triazole-Based Coumarin Compounds as Acetylcholinesterase Inhibitors: Evidence and Mechanism of 3-Acetyl Coumarin Tethered (2-Bromophenyl)-1,2,3-Triazole as a Potential Mixed-Type Inhibitor. *Eur. J. Med. Chem. Rep.* **2025**, *15*, 100289.

24. Pourabdi, L.; Küçükkılınç, T. T.; Khoshtale, F.; Ayazgök, B.; Nadri, H.; Farokhi Alashti, F.; et al. Synthesis of New 3-Arylcoumarins Bearing N-Benzyl Triazole Moiety: Dual Lipoxygenase and Butyrylcholinesterase Inhibitors with Anti-Amyloid Aggregation and Neuroprotective Properties Against Alzheimer's Disease. *Front. Chem.* **2022**, *9*, 810233.

25. Dimkovski, A.; Dobričić, V.; Simić, M. R.; Jurhar Pavlova, M.; Mihajloska, E.; Sterjev, Z.; Poceva Panovska, A. Synthesis, Biological Evaluation, and Molecular Docking Studies of Novel Coumarin–Triazole–Isatin Hybrids as Selective Butyrylcholinesterase Inhibitors. *Molecules* **2025**, *30*, 2121.

26. Najafi, Z.; Mahdavi, M.; Saeedi, M.; Karimpour-Razkenari, E.; Edraki, N.; Sharifzadeh, M.; Khanavi, M.; Akbarzadeh, T. Novel Tacrine–Coumarin Hybrids Linked to 1,2,3-Triazole as Anti-Alzheimer's Compounds: In Vitro and In Vivo Biological Evaluation and Docking Study. *Bioorg. Chem.* **2019**, *83*, 303–316.

27. Sharma, A.; Bharate, S. B. Synthesis and Biological Evaluation of Coumarin Triazoles as Dual Inhibitors of Cholinesterases and β-Secretase. *ACS Omega* **2023**, *8* (12), 11161–11176.

28. Bhagat, K.; Singh, J. V.; Sharma, A.; Kaur, A.; Kumar, N.; Gulati, H. K.; Singh, A.; Singh, H.; Bedi, P. M. S. Novel Series of Triazole Containing Coumarin and Isatin-Based Hybrid Molecules as Acetylcholinesterase Inhibitors. *J. Mol. Struct.* **2021**, *1245*, 131085.

29. Singh, A.; Sharma, S.; Arora, S.; Attri, S.; Kaur, P.; Gulati, H. K.; Bhagat, K.; Kumar, N.; Singh, H.; Singh, J. V.; Bedi, P. M. S. New Coumarin–Benzotriazole Based Hybrid Molecules as Inhibitors of Acetylcholinesterase and Amyloid Aggregation. *Bioorg. Med. Chem. Lett.* **2020**, *30*, 127477.

30. Nadur, N. F.; Ferreira, L. d. A. P.; Franco, D. P.; de Azevedo, L. L.; Caruso, L.; Honório, T. d. S.; et al. Design, Synthesis, and Biological Evaluation

of Novel Multitarget 7-Alcoxyamino-3-(1,2,3-Triazole)-Coumarins as Potent Acetylcholinesterase Inhibitors. *Pharmaceuticals* **2025**, *18*, 1398.

CHAPTER 7

ECO-FRIENDLY PESTICIDE DESIGN AT THE MOLECULAR LEVEL USING PYRETHRUM EXTRACT COMPONENTS

Lect. Dr. Yasemin KEŞKEK KARABULUT[1]

---

[1] Kırklareli University, Project Development and Coordination Office, Kırklareli, Turkey. ORCID: 0000-0002-6742-783X

INTRODUCTION

The rising global population has not only intensified the demand for food but also increased reliance on pesticides to safeguard agricultural products. However, the uncontrolled and excessive application of these chemicals has resulted in significant environmental pollution, making strict regulation essential. Ensuring the safe and informed use of pesticides is critical for both human health and ecological balance. In the context of food security, climate change and the need to feed a rapidly expanding global population require producing more food with limited water resources and shrinking agricultural land. In addition, recent years have witnessed a notable rise in the use of high-yield crop varieties, chemical fertilizers, pesticides, and related agricultural inputs (Kumar, 2012). Considering current consumption patterns and the pressures brought about by climate change, increasing agricultural productivity has become a key priority. As global food demand grows and climate impacts intensify, pesticides continue to play an essential role in sustaining crop yields (Deutsch et al., 2018). Their use has expanded particularly for managing pests that threaten production. At the same time, minimizing pesticide-related contamination risks has become a central objective in agricultural policies worldwide (Möhring et al., 2020). Reflecting these concerns, the European Union has set a target to reduce pesticide use and associated risks by 50% by the year 2030 (Schebesta & Candel, 2020).

Global market assessments and Food and Agriculture statistics indicate that worldwide pesticide consumption has reached 4.12 million tons annually (Boateng et al., 2023). In Turkey, the data show that the country ranks 12th in global pesticide usage, representing approximately 1.23% of total worldwide consumption. In 2022 alone, nearly 55,000 tons of pesticides were applied across the country (Sevim et al., 2023). The pursuit of fast and effective outcomes in agricultural production has led many producers to rely heavily on chemical pesticides. However, the excessive application of these chemicals has resulted in residue accumulation in soil, water sources, and agricultural products (Sharma et al., 2017). Consequently, interest in alternative pest control strategies, rather than conventional chemical-based approaches, has grown significantly in recent years.

This shift is reflected in policy initiatives developed within the scope of the "Green Deal" in both Europe and Turkey, where actions aimed at reducing

pesticide use and promoting natural pest control solutions by 2030–2050 have begun to accelerate. The European Green Deal envisions a comprehensive and transformative approach, prioritizing objectives such as preventing environmental pollution, safeguarding biodiversity, and advancing organic farming practices (Ecer et al., 2021). In alignment with these priorities, Turkey has incorporated parallel actions into its 12th Development Plan, which includes a dedicated section on "Sustainable Agriculture." Within this framework, and in accordance with the European Union's goals for reducing pesticides and antimicrobials, Turkey aims to intensify efforts to minimize the negative effects of these substances while promoting broader adoption of alternative control methods.

Pathogens, weeds, and insect pests create major obstacles to global food security and sustainable development, as they substantially limit agricultural productivity worldwide. Integrated Pest Management (IPM) has emerged as a key policy tool within strategic programs such as the 12th Development Plan and the Green Deal. IPM incorporates a combination of pest control strategies designed to reduce, and when possible, replace the use of synthetic pesticides. This approach has long been applied in agriculture and is recognized as a sustainable and environmentally responsible pest management method (Angon et al., 2023).

IPM supports the objectives of the 12th Development Plan by decreasing reliance on chemical inputs and encouraging the adoption of biological control methods. At the same time, it aligns with the Green Deal's priorities by contributing to environmental protection, reducing chemical pesticide use, and promoting climate-resilient agricultural practices. Through these complementary benefits, integrated pest management not only enhances the sustainability of agricultural production but also provides value for both economic development and ecological preservation. For these advantages to be fully realized, however, IPM strategies must be implemented with careful planning and strong scientific guidance.

Achieving sustainable agriculture requires simultaneously protecting the environment and human health while maximizing yield per unit area. This is only possible through environmentally friendly production practices that are also economically feasible. To meet these objectives, both chemical and biological methods for managing harmful pests and weeds in agricultural fields

must be considered. Although chemical control remains widely used due to its ease of application and quick effectiveness, recent studies have shown that it can cause long-term, irreversible harm to ecosystems and human well-being. Intensive and indiscriminate use of chemical pesticides negatively affects biodiversity, while residue issues are becoming increasingly problematic in international agricultural trade. Moreover, excessive application and the subsequent runoff of pesticides into water bodies during rainfall frequently result in the death of fish and other aquatic organisms (Ayilara et al., 2023).

One of the core aims of the Green Deal is to expand the use of biological and biotechnical control methods. Biological control is increasingly viewed as a viable alternative to chemical-based approaches, supporting biodiversity and enabling the adoption of more sustainable pest management practices. Biopesticides used in biological control are considered safer, more sustainable, and, in the long term, more economical for both the environment and human health (Uygun et al., 2010; Lenteren, 2000). These biopesticides also offer new alternatives to chemical pesticides by helping address global resistance issues faced by farmers and consumers, enhancing biodiversity, reducing carbon footprints, mitigating chemical residue challenges, and meeting farmers' productivity demands (Marrone, 2023).

Biopesticides are pest-suppressing agents derived from natural sources such as bacteria, fungi, viruses, plants, animals, and minerals (Thakore, 2006). Unlike synthetic chemical pesticides, which typically affect a broad spectrum of organisms—including both harmful and beneficial species—biopesticides are designed to target specific pests or diseases. While chemical pesticides often exhibit toxic and pathogenic properties, biopesticides are generally considered non-harmful. Additionally, synthetic pesticides are produced through complex formulations involving multiple chemical compounds, whereas biopesticides are commonly obtained from naturally occurring organisms or their metabolic byproducts (Essiedu et al., 2020).

The modes of action of biopesticides vary and may include disruption of plasma membrane integrity, inhibition of cellular processes, and interference with protein synthesis in target pests or pathogens. Although certain drawbacks have limited their widespread adoption, biopesticides offer notable advantages: they exhibit high target specificity, degrade rapidly in the soil, have short environmental persistence, and are produced from renewable biological

materials—features that differentiate them from conventional pesticides (Kumar et al., 2021). However, their specificity can also become a limitation when multiple pests need to be controlled simultaneously. Their short shelf life, while environmentally beneficial, can hinder long-term pest suppression and reduce their effectiveness after application (Ayilara et al., 2023).
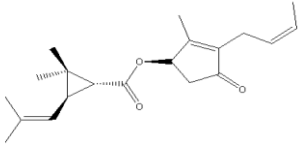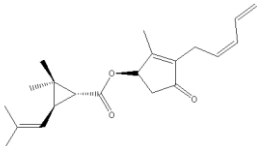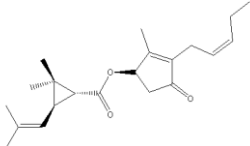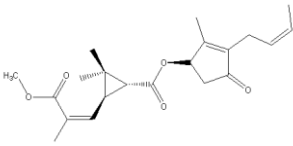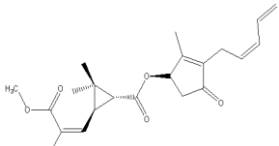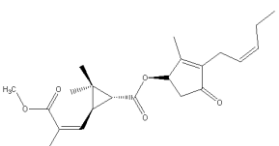
Several additional barriers still impede the full integration, development, and commercialization of biopesticides in agricultural systems. Common concerns include their perceived lower efficacy and slower action compared to chemical alternatives (Delgado-Carrillo et al., 2018). Commercial biopesticide products also tend to be costly and less accessible in global markets. Challenges such as production scalability, quality control, and limited storage stability continue to restrict their adoption (Arthurs & Dara, 2019). Furthermore, some farmers express uncertainty regarding proper dosage levels and fear the emergence of new pest populations that may develop resistance to currently available biopesticides (Stevenson et al., 2017).

In recent years, critically evaluating the advantages and limitations of biopesticides used in biological control—recognized as promising alternatives to synthetic pesticides—has become increasingly important. Equally vital is identifying potential strategies to overcome their current shortcomings. A comprehensive understanding of the molecular mechanisms that govern biopesticide activity at each stage of their interaction with pests is essential for developing more effective pest management approaches. Elucidating these mechanisms will make it possible to design synergistic combinations of biopesticides with distinct modes of action, thereby avoiding overlap and enhancing overall efficacy. Such knowledge will also facilitate the identification and characterization of diverse toxic molecules naturally present within biopesticides, potentially broadening the spectrum of pesticidal compounds available (Ayilara et al., 2023). Consequently, investigating biopesticides at the molecular level may help mitigate the harmful effects associated with synthetic pesticides and support the adoption of safer pest control agents during the transition toward sustainable agriculture.

Pyrethrum extract is one of the most commonly used plant-based biopesticides in the global market and is widely applied in agriculture, veterinary practices, and aquaculture (Karakaş, 2018). Pyrethrum refers to the oleoresin obtained from the dried flowers of Chrysanthemum cinerariaefolium.

It is composed of six primary active compounds: pyrethrin I, pyrethrin II, cinerin I, cinerin II, jasmolin I, and jasmolin II. Among these, pyrethrin I, cinerin I, and jasmolin I are esters of chrysanthemic acid, whereas pyrethrin II, cinerin II, and jasmolin II are esters of pyretic acid (Laxmishree & Nandita, 2017) (Table 1). Pyrethrins exert their effects primarily on the insect nervous system by modifying sodium channel permeability and function, thereby disrupting the normal biochemical and physiological processes of nerve membranes. Today, pyrethrins are incorporated into more than 2,000 commercial and household formulations. They are used to control disease-transmitting insects in greenhouse production and are included in disinfection sprays for aircraft. Pyrethrins also see extensive household use for managing pests such as mosquitoes, houseflies, and bedbugs (Bomzan et al., 2018; Mossa et al., 2018).

Table 1. Pyrethrum Extract Components

Cinerin I (Cas No: 25402-06-6)	**Piretrin I** (Cas No: 121-21-1)	**Jasmolin I** (Cas No: 4466-14-2)
Cinerin II (Cas No: 121-20-0)	**Piretrin II** (Cas No: 121-29-9)	**Jasmolin II** (Cas No: 1172-63-0)

Among the six constituents of pyrethrum, pyrethrins I and II are the most abundant and biologically active. Notably, they differ significantly in their toxic effects on insects. Pyrethrin I exhibits a stronger lethal impact, causing rapid mortality within minutes, whereas pyrethrin II is primarily responsible for a faster knockdown effect. However, insects can efficiently metabolize pyrethrin II, allowing them to recover within a few hours. Despite these differences, the combined presence of pyrethrin I and pyrethrin II demonstrates remarkably high effectiveness against a wide variety of insect species (Jeran et al., 2021).

Although several studies have examined the environmental toxicology and human health effects of individual components within pyrethrum extract, these compounds have typically been evaluated in the form of whole extracts rather than as isolated molecules. For instance, pyrethrins are known to degrade rapidly under increasing temperatures and through photolysis, disappearing quickly without leaving harmful residues or bioaccumulating in the environment. Field studies involving aerial applications of pyrethrins reported no adverse impacts on large-bodied non-target arthropods, such as certain dragonfly, spider, and butterfly species (Boyce et al., 2007). However, more recent research published in 2023 showed that pyrethrins can negatively affect some aquatic organisms (Diogo et al., 2023). Natural pyrethrins are generally more target-specific than their synthetic counterparts. They function as contact and stomach poisons, causing immediate knockdown upon exposure, and display low mammalian toxicity and short residual activity due to rapid degradation by sunlight, air, and moisture. As a result, repeated applications may be necessary (Souto et al., 2021).

Synthetic pyrethrins, in contrast, were developed based on knowledge of the chemical structures of naturally occurring pyrethrum-derived insecticidal compounds. Although the exact origin of the earliest discovery of these natural insecticidal properties remains unclear, synthetic analogs were engineered to enhance stability and potency. Like all pesticides, these compounds are specifically designed to exert toxic effects on their target organisms. Because many biochemical target sites are conserved across taxonomic groups, synthetic pyrethrins also pose toxicity risks to non-target organisms, including fish (Fulton et al., 2013).

Although some studies have explored the structures of the active components of pyrethrum extract in relation to environmental and human

health, the number of available sources and the depth of their content suggest that further research is still needed. Moreover, most existing studies rely heavily on experimental approaches and primarily examine the extract as a whole, without providing detailed insight into the individual constituents. Theoretical and computational tools—which are widely used in fields such as computational chemistry, drug design, computational biology, and materials science to model molecular behavior—have not yet been sufficiently applied to support or complement these studies. While basic calculations can be performed manually, computer-based molecular modeling is essential for systems of any meaningful size or complexity.

In silico methods can play a valuable role by predicting toxicity in cases where experimental data are lacking and by reducing the number of laboratory studies required for compounds with low toxicity, especially when high precision is not necessary for risk assessment or management. Quantitative structure–activity relationships (QSAR) provide an alternative computational approach for predicting toxicity by identifying molecular hazards based on structural and physicochemical properties. Furthermore, commercial QSAR tools—commonly used in the chemical industry to assess human and environmental impacts, prepare safety data sheets (SDS), and generate export documentation—can substantially reduce the time and cost associated with evaluating the ecotoxicological and toxicological effects of biopesticides in agricultural applications (Soni et al., 2014; Jeran et al., 2021).

In a 2006 study, a fragment-based QSAR approach was introduced to correlate LC_{50}–96 h acute toxicity in rainbow trout (*Oncorhynchus mykiss*) within the context of pesticide risk assessment. Assuming that a single molecular fragment could be primarily responsible for toxicity, the authors proposed a three-stage modeling strategy to identify the most significant fragments and prioritize them at the molecular level. This strategy was tested on a heterogeneous dataset of 282 pesticides compiled within the EU-funded Demetra project. The results obtained from both the training and test sets quantitatively demonstrated the reliability and effectiveness of the method. Nevertheless, the approach could not be successfully applied to all pesticides due to the substantial structural diversity of the compounds. The authors therefore emphasized the need for additional data to better understand the

toxicological properties of pesticides and recommended further research in this area (Casalegno *et al.*, 2006).

A 2021 study examining pesticides in a comprehensive dataset and classifying them according to their primary indications reported that insecticides tended to exhibit higher pNOEC values, whereas herbicides reached their maximum values at comparatively lower levels, and fungicides were distributed around the center of the range. This pattern is expected, as major herbicide targets—such as Photosystem II—are absent in fish, whereas many insecticides act on evolutionarily conserved targets shared between vertebrates and invertebrates (e.g., components of the nervous system) (Schmidt *et al.*, 2021).

Numerous international regulations address the evaluation of pesticides, including the European Union Pesticides Legislation, EFSA (European Food Safety Authority) guidelines, and the U.S. EPA (Environmental Protection Agency) guidelines. In Türkiye, compliance is maintained through the Plant Protection Products Regulation, the Regulation on the Licensing of Plant Protection Products, and various regulations on good agricultural practices (Tarakçı and Türel, 2009). Although these national and global guidelines include sections that acknowledge and guide the use of SAR models, they do not clearly define the extent, specific conditions, or practical scenarios in which quantitative structure–activity relationship models may be applied. Moreover, their broad applicability and reliability have yet to be conclusively demonstrated (United States, 1976).

However, in recent years, SAR and QSAR models have begun to be actively applied worldwide, including in Türkiye, particularly within the scope of the REACH regulation, which governs chemical exports in EU countries. A clear example is found in Article 23(1) of the KKDİK Regulation (Regulation on the Registration, Evaluation, Authorization and Restriction of Chemicals), published in the Official Gazette in 2017 as part of Türkiye's EU Harmonization Process. This article stipulates that vertebrate testing must be used only as a last resort and that all possible alternatives must be considered before such testing is conducted. Accordingly, registrants are required to compile all available information on the physicochemical, toxicological, and ecotoxicological characteristics of a substance, including data obtained from (Q)SAR models and chemical grouping methods. Furthermore, Annex 11 of

the KKDİK Regulation explicitly supports the use of (Q)SARs and grouping approaches in situations where new testing is not necessary, as equivalent levels of information can be generated through non-animal methods.

This study aimed to test the suitability of computational methods such as QSAR and Docking for applications within the context of food sustainability and sustainable agriculture within the framework of regulatory compliance and to address missing information in the literature. Theoretical studies were conducted on the environmental hazards of existing pyrethrum extract components. Furthermore, based on the chemical structures of pyrethrum extract components, recommendations were made regarding the effectiveness of the functional groups present on the components to design new, more environmentally friendly, and more efficient potential pesticides.

2. EXPERIMENTAL

2.1. Theoretical ecotoxicity studies of compounds in Pyrethrum Extract by ECHA QSAR

Experimental assessment of chemical toxicity in aquatic organisms has increasingly been criticized due to both high costs and ethical concerns. This has led quantitative structure–activity relationship (QSAR) modeling to become a valuable alternative for reducing the expense and labor associated with traditional toxicity testing (Muratov et al., 2020). Since 2006, the European REACH regulation has required an initial evaluation of aquatic toxicity prior to the manufacture or commercialization of chemicals. In response to this requirement, numerous QSAR-based investigations have been conducted, providing predictive models for various aquatic toxicity endpoints (Tinkov et al., 2021).

Toxicophores—also referred to as structural alerts or toxic fragments—provide a straightforward approach for identifying potentially hazardous compounds and are extensively applied in environmental toxicology and drug discovery. These alerts are incorporated into numerous software platforms, including the OECD QSAR Toolbox, Derek Nexus, ToxTree, and ToxAlerts. Structural rules generally fall into two categories: expert-derived (human-based) rules and computationally generated (inductive) rules. Human-based rules are developed from expert knowledge or published literature and are often

regarded as more accurate and easier to interpret. Their main limitation, however, is that they depend on the current state of human expertise, which may be incomplete or biased. Inductive rules, on the other hand, can be rapidly produced from large datasets using computational methods such as QSAR. Both types of structural rules help identify potential toxic liabilities and classify chemicals for read-across purposes. Moreover, toxicity-prediction QSAR models are frequently criticized for lacking interpretability and functioning as "black boxes." For this reason, models built in line with the OECD's fifth principle of QSAR modeling should aim to be interpretable whenever feasible (Tinkov et al., 2021).

The OECD QSAR Toolbox is a software platform created to support chemical hazard assessment by enabling efficient, mechanism-based evaluation of chemical substances in a cost-effective manner. As a freely accessible computational tool, it promotes the adoption of alternative methods to animal testing and helps to avoid unnecessary in vivo studies, while maintaining high standards of human health and environmental protection. The Toolbox is intended for use by regulatory authorities, the chemical industry, and other stakeholders. In essence, computational tools such as this reduce reliance on animal experiments, lower testing costs, and expand the number of chemicals that can be assessed for potential risks. Moreover, by allowing toxicity predictions to be made even before a substance is manufactured, the Toolbox supports sustainable product development and advances in green chemistry (Keşkek Karabulut et al., 2023). Developed by EU member states in 2005, the OECD QSAR Toolbox has become a key resource for predicting chemical toxicity. Its strong institutional backing (OECD and ECHA), extensive integrated databases, and reliable predictive capabilities make it a widely recognized tool in regulatory toxicology (Suarez-Torres et al., 2020).

The primary purpose of the OECD QSAR-Toolbox software is to allow users to use (Q)SAR methodologies to group chemicals into categories and fill data gaps using read-across, trend analysis, and (Q)SARs. The OECD QSAR-Toolbox includes multiple functionalities that allow users to perform a range of operations. These include:

• Identifying analogues for a chemical, retrieving existing experimental results for these analogues, and filling data gaps using read-across or trend analysis;

• Classifying large chemical inventories according to mechanism or mode of action;

• Filling data gaps for any chemical using databases within QSAR models;

• Assessing the robustness of a potential analogue for read-across;

• Assessing the suitability of a (Q)SAR model to fill a data gap for a specific target chemical;

• Making predictions by creating QSAR models (Dimitrov et al., 2016)

In this part of the study, theoretical ecotoxicity studies (acute aquatic toxicity to Daphnia Magna) were conducted for six active components of pyrethrum extract used as a biopesticide using the OECD QSAR method. A review of the literature revealed that theoretical ecotoxicological study results for the pyrethrin structure are insufficient, and the few experimental studies that exist have focused on different targets and have not directly studied the pure structure (Lawler et al., 2008; Jia et al., 2022; Rajini et al., 2016; Haya, 1989).

In this section, the QSAR Toolbox 4.6 program downloaded from ECHA's website "https://qsartoolbox.org/download/" was used. Acute toxicity studies of the component structures (6 units) using the OECD QSAR toolbox were carried out in the following steps (Yordanova, et al., 2019):

● The target compounds found in pyrethrum extract were identified by CAS number.

● Profiling: Identifying the structural features and mode of action (MOA) that characterize the target chemical applies a series of computerized modules (known as profilers) whose task is to identify structural and mechanistic properties related to aquatic toxicity. These profiling results are then used as query criteria to identify suitable structural analogs. The profiling module was run for the target compounds found in pyrethrum extract.

● Data collection: Relevant ecotoxicological databases were searched for the target compounds found in pyrethrum extract to obtain an initial set of structural analogs, which formed a broad initial category that was then refined for structural and mechanistic relevance.

● Subcategorization: After these initial steps, profilers were applied iteratively to further refine the structural and mechanistic consistency of the initial category of structural analogs.

● Prediction: EC50 and LC50 estimates were then calculated for the identified compounds. If the number of structural analogs is greater than (or equal to) ten, a linear QSAR model measuring changes in EC50 and LC50 values as a function of the octanol water partition coefficient Log Kow was defined and used to calculate a prediction (with Read-across/QSAR Predictions). ● Report: A report was generated for predictions for the six compounds in the Pyrethrum extract analyzed in the "Report" module, along with their similar structures (Saouter et al., 2019).

2.2 Conducting docking studies to identify the working mechanism of the compounds in Pyrethrum Extract

Gaussian09 is the latest in a series of Gaussian electronic structure programs. It is designed to model a wide range of molecular systems under a wide variety of conditions, performing calculations using the fundamental laws of quantum mechanics. It is used to conduct research in established and emerging areas of interest in Gaussian chemistry, including studies of certain or potential reactions in molecules and compounds that are impossible or very difficult to study experimentally (e.g., short-lived intermediates, transition structures, and the like) (Frisch, 2009).

Gauss View 5.0.8 is a graphical interface designed for creating input files for Gaussian packages and visualizing Gaussian outputs. Gauss View visualizes molecules, allowing us to rotate, move, and manipulate them as desired. It also allows us to easily create input files for even complex calculations. It also allows us to graphically analyze the results calculated by the Gaussian program (Dennington et al., 2009).

The Protein Data Bank (PDB) is a rich resource containing the 3D structures of large biological molecules such as proteins and nucleic acids. The information in the protein data bank is sourced from X-ray crystallography or nuclear magnetic resonance (NMR) spectroscopy. Researchers can access structural information submitted by biologists and biochemists from around the world through this system. Macromolecules in the protein data bank are stored in files with the .pdb extension. PDB files are named after four characters, the

first of which is a number. The .pdb format contains the atomic coordinates of the protein macromolecule, primary and secondary structure information, crystallographic structure factors, and NMR information. The PDB format is recognized by almost all programs used in drug design (Berman et al., 2000).

AutoDock Vina is a docking program developed in 2010 by the same laboratory as AutoDock. AutoDock Vina's algorithm is a combination of several local and global optimization approaches. AutoDock Vina performs docking twice as fast as AutoDock. As is common with all docking programs, a scoring function is used that attempts to approximate the system's standard chemical potentials. The scoring function used by AutoDock Vina is an improved version of the Xscore function. When physics-based terms such as 6-12 van der Waals interactions and Coulomb energies are used in the scoring functions, docking programs often require significant modifications to account for differences between the experimental and free energies. For these reasons, the scoring function may need to include these scoring function parameters in the program's configuration file, taking into account the combined effects of hydrophobic interactions between hydrophobic atoms and steric interactions for all atom pairs in hydrogen bonds (Trott and Olson, 2010). A graphical user interface called AutoDockTools, or ADT for short, is also available. This helps, among other things, to set which bonds in the ligand are treated as rotatable and to analyze dockings (Morris et al., 2009).

In this section, a docking study was conducted for six compounds found in Pyrethrum Extract, used as a biopesticide. The most stable structures of the chemical structures (six compounds as ligands) to be used in the docking study should be used in the docking process. Therefore, the approximate three-dimensional geometry of the recorded gas-phase molecules was drawn using GaussView 5.0 molecular imaging software. The initial geometries of the molecules were obtained from GaussView 5.0 and transferred as input to the Gaussian 09W software package. An optimization process was performed to find the most stable structures with minimum energy for the molecules drawn with Gaussian 09W. Advanced geometry optimizations were calculated using the B3LYP/6–31++G (d, p) basis set in density functional theory (DFT). The optimized molecules were converted to .pdb format and prepared for docking.

The modified structure files were opened using the autodock tools (adt) user interface. First, the torsion root and the number of torsions in the ligand

molecule were determined. Finally, the resulting structure molecules were saved in .pdbqt format and prepared for docking.

To identify the mechanisms by which compounds in pyrethrum extract affect the nervous system, the dissolved sodium channel structure was selected from the RSCB database based on its dissolution type, solubility coefficient, presence of mutations, and year of dissolution. Based on these parameters, the pdb code 6A90 (Shen, et all., 2018) was selected. The selected structure was separated from its ligands and its active site was identified. The prepared sodium channel structure was saved in .pdbqt format.

A configuration file containing the enzyme and ligand .pdbqt files prepared with ADT was prepared for the docking process with AutoDock Vina. The file information for the enzyme and ligand to be calculated was also prepared, along with the Cartesian coordinates of the target and docking area, and the width of the docking region. The Cartesian coordinates obtained from the grid map were prepared for docking. A configuration file named "conf" is available in .txt format. It contains the file name and format of the ligand and macromolecule to be docking, the Cartesian coordinates of the grid map, and the grid box size values. The configuration file is the sole input file for Vina calculations. The vina.exe file, developed by The Scripps Research Institute, which runs the Vina program, was invoked via the command prompt. Log files were then recorded by the program. The results were interpreted using the ADT interface.

3. RESULTS AND DISCUSSION

3.1 Results of theoretical ecotoxicity studies of compounds in Pyrethrum Extract by ECHA QSAR

Using the ECHA QSAR program, we first examined the toxicological data to determine whether the six active compounds in pyrethrum extract cause skin irritation. The program's simplicity allows us to determine whether the results are directly irritating or non-irritating. Therefore, unlike other QSAR methods, detailed expert opinion is not required. Following skin irritation/skin

corrosion testing, it was determined that all components had no irritating or corrosive effects on the skin (Table 2).

Table 2. Skin Irritation or Skin Corrosion for Pyrethrum Extract Components

Pesticide	Irritation Condition	Pesticide	Irritation Condition
Pyrethrin I	Non-irritating	**Pyrethrin II**	Non-irritating
Cinerin I	Non-irritating	**Cinerin II**	Non-irritating
Jasmolin I	Non-irritating	**Jasmolin II**	Non-irritating

In another part of the study, the ECHA QSAR program was used to examine toxicological data to determine whether the six active compounds in pyrethrum extract cause eye irritation. The program's simplicity can be attributed to its ability to provide direct irritant/non-irritant results. Therefore, unlike other QSAR methods, detailed expert opinion is not required. Following the eye irritation test, all components were found to be non-irritating to the eye (Table 3).

Table 3. Eye Irritation for Pyrethrum Extract Components

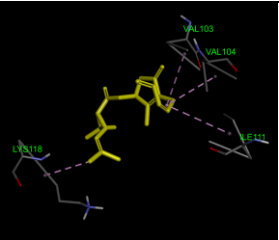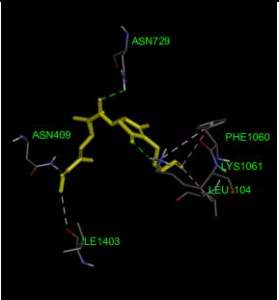| Pesticide	Irritation Condition	Pesticide	Irritation Condition
Pyrethrin I	Non-irritating	**Pyrethrin II**	Non-irritating
Cinerin I	Non-irritating	**Cinerin II**	Non-irritating
Jasmolin I	Non-irritating	**Jasmolin II**	Non-irritating

In the final phase of this part of the study, acute aquatic toxicity in Daphnia was studied using the ECHA QSAR method to examine ecotoxicological properties. This calculation was based on the calculation of the EC_{50} value, focusing on a 48-hour exposure to Daphnia. The EC_{50} value represents the maximum concentration at which the substance in question is toxic. The lower the EC50 value, the more toxic the substance in question. When the results were examined, it was theoretically found that each component had different EC50 values. Jasmolin II had the lowest EC50 value at 0.00742 mg/L, while Cinerin I had the highest at 0.016 mg/L (Table 4).
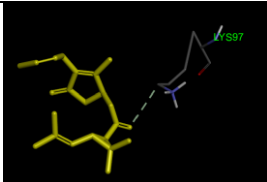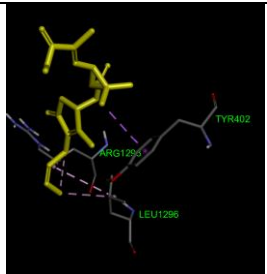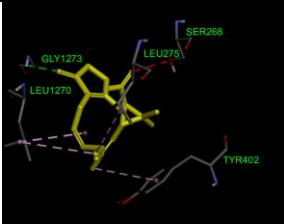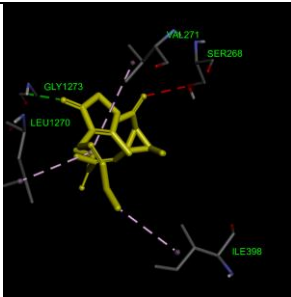
Table 4. 48h Daphnia Acute Aquatic Toxicity Values for pyrethrum extract components

Pesticide	EC$_{50}$	Pesticide	EC$_{50}$
Pyrethrin I	0.0117 mg/L	**Pyrethrin II**	0.00812 mg/L
Cinerin I	0.016 mg/L	**Cinerin II**	0.0111 mg/L
Jasmolin I	0.0108 mg/L	**Jasmolin II**	0.00742 mg/L

3.2 Results of conducting docking studies to identify the working mechanism of the compounds in Pyrethrum Extract

Table 5. Doking results of ingredients in pyrethrum extract

Structure	Binding Energy	Interactions	Interacting Amino Acids in Active Site	3D Image
Pyrethrin I	-7.6 kcal/mol	Alkyl Interactions	LYS118, VAL103, ILE111, VAL104	
Pyrethrin II	-7.0 kcal/mol	3 H Bond (ASN409, ASN729, LYS1061) Alkyl and Pi-Alkyl Interactions	ILE1403, ASN409, ASN729, LYS1061, PHE1060, LEU1104	

Cinerin I	-7,9 kcal/mol	-	LYS97	
Cinerin II	-7.3 kcal/mol	Pi-Sigma and Alkyl Interactions	TYR402, ARG1293, LEU1296	
Jasmolin I	-7.8 kcal/mol	1 H Bond (GLY1263) Alkyl and Pi-Alkyl Interactions	TYR402, SER268, GLY1273, LEU1270, LEU275	
Jasmolin II	-7.8 kcal/mol	1 H Bond (GLY1273) Alkyl Interactions	SER268, GLY1273, LEU1270, ILE398, VAL271	

When the docking results were examined (Table 5), Cinerin I component showed the best binding with a binding energy of -7.9 kcal/mol. This was followed by Jasmolin I and Jasmolin II components with binding energy of -7.8 kcal/mol. Cinerin II component showed the lowest binding energy with a binding energy of -7.3 kcal/mol.

4. CONCLUSION

This study demonstrated that theoretical ecotoxicity assessment and molecular docking approaches can be effectively integrated to assess the environmental behavior and biological activity of biopesticide components derived from pyrethrum extract. QSAR-based predictions revealed that six active compounds (pyrethrins I and II, cinerin I and II, and jasmolin I and II) exhibited non-irritating properties upon both skin and eye contact, supporting their suitability as safer alternatives to traditional synthetic pesticides. Acute aquatic toxicity analyses using the ECHA QSAR Toolbox showed that, although all components exhibited some level of toxicity to Daphnia magna, their EC50 values varied significantly, with Jasmolin II being the most toxic and Cinerin I the least. These results highlight the importance of evaluating each component individually rather than treating pyrethrum extract solely as a uniform mixture.

Molecular docking studies, however, provided further insight into the mechanisms of action of these components through their interactions. Binding affinity values ranged from -7.0 to -7.9 kcal/mol, indicating a generally strong and consistent interaction pattern among all compounds. Among the analyzed compounds, Cinerin I had the highest binding affinity, while Cinerin II had the lowest energy score. These results also highlight structural differences in binding behavior, suggesting that certain functional groups can enhance or weaken their insecticidal potential.

The main difference between the nomenclatures of compounds I and II stems from the presence of the functional group in the acid group, despite both molecules sharing the same core structure. Structures II contain an additional carboxyl functional group. From this perspective, the results suggest that the carboxyl group does not cause any change in the toxicological irritation characteristic, but does affect ecotoxicological toxicity. Furthermore, the results suggest that this carboxyl functional group also plays a role in sodium channel inhibition in insects, reducing its inhibitory potential.

Overall, the combined use of QSAR and molecular docking methods has yielded valuable results in elucidating the toxicological and mechanistic profiles of pyrethrum-derived biopesticides. This approach is not only compatible with international regulatory frameworks that encourage the reduction of animal testing but also facilitates the rational design of new,

environmentally friendly, and effective pesticide molecules. The findings of this study suggest that modifications of specific functional groups in pyrethrin-like structures could lead to the development of next-generation biopesticides with optimized efficacy and minimal ecological impact. Future studies may benefit from integrating experimental validations, additional target proteins, and extended computational models to further enhance predictive accuracy and support sustainable agricultural practices.
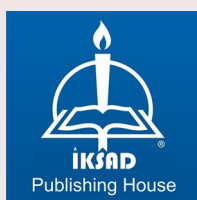
REFERENCES

Lawler, S.P., Dritz, D.A., Johnson C.S., Wolder M. (2008). Does synergized pyrethrin appliedover wetlands for mosquito control affect Daphnia magnazooplankton or Callibaetiscalifornicusmayflies?. *Pest. Manag. Sci.,* 64, 843 – 847.

Frisch, A. (2009). gaussian 09W Reference. Wallingford, USA, 25p, 470.

Jia, Q., Wang, J., Yan, F., Wang, Q. (2022). A QSTR model for toxicity prediction of pesticides towards Daphnia magna. *Chemosphere,* 291(2), 132980.

Berman, H. M., Westbrook, J., Feng, Z., Gilliland, G., Bhat, T. N., Weissig, H., ... & Bourne, P. E. (2000). The protein data bank. Nucleic acids research, 28(1), 235-242.

Dennington, R., Keith, T., & Millam, J. (2009). GaussView, version 5.

Saouter, E., Biganzoli, F., Pant, R., Sala, S., Versteeg, D. (2019). Using REACH for the EU environmental footprint: building a usable ecotoxicity database, part I. *Integrated Environmental Assessment and Management,* 15(5), 783.

Yordanova, D., Schultz, T.W., Kuseva, C., Ivanova, H., Pavlov, T., Chankov, G., Karakolev, Y., Gissi, A., Sobanski, T., Mekenyan, O.G. (2019). Alert performance: A new functionality in the OECD QSAR Toolbox. *Computational Toxicology,* 10, 26-37.

Rajini, A., Revathy, K., Chitrikha, T. (2016). Toxicity and Reproductive Effect of Combination Pesticide to Daphnia magna. *Indian Journal of Science and Technology,* 9(3), 1-5.

Haya, K. (1989). Toxicity of pyrethroid insecticides to fish. *Environmental Toxicology and Chemistry,* 8(5), 381-391.

Suarez-Torres, J.D., Ciangherotti, C.E., Jimenez-Orozco, F.A., (2020). The predictivity of the -alert performance- functionality of the OECD QSAR-Toolbox (c/w further issues on the predictivity of nonclinical testing). *Toxicology in Vitro,* 66, 104858.

Kumar, S. (2012). "Biopesticides: A Need for Food and Environmental Safety". *Journal of Fertilizers & Pesticides*, 3(4), 1000e107.

Dimitrov, S.D., Diderich, R., Sobanski, T., Pavlov, T.S., Chankov, G.V., Chapkanov, A.S., Karakolev, Y.H., Temelkov, S.G., Vasilev, R.A.,

Gerova, K.D., Kuseva, C.D., Todorova, N.D., Mehmed, A.M., Rasenberg, M., Mekenyan, O.G. (2016). QSAR Toolbox – workflow and major functionalities. *SAR and QSAR in Environmental Research,* 27, 203-219.

Deutsch, C.A., Tewksbury, J.J., Tigchelaar, M., Battisti, D. S., Merrill, S.C., Huey, R.B., Naylor, R.L. (2018). Increase in crop losses to insect pests in a warming climate. *Science,* 361 (6405), 916-919.

Möhring, N., Ingold, K., Kudsk, P., Martin-Laurent, F., Niggli, U., Siegrist, M., Studer, B., Walter, A., Finger, R. (2020). Pathways for advancing pesticide policies. *Nature Food,* 9, 535-540.

Trott, O., & Olson, A. J. (2010). AutoDock Vina: improving the speed and accuracy of docking with a new scoring function, efficient optimization, and multithreading. *Journal of computational chemistry,* 31(2), 455-461.

Morris, G. M., Huey, R., Lindstrom, W., Sanner, M. F., Belew, R. K., Goodsell, D. S., & Olson, A. J. (2009). AutoDock4 and AutoDockTools4: Automated docking with selective receptor flexibility. *Journal of computational chemistry,* 30(16), 2785-2791.

Schebesta, H., Candel, J.J.L. (2020). Game-changing potential of the Eu's farm to fork strategy. *Nature Food,* 1, 586-588.

Boateng, K.O., Dankyi, E., Amponsah, I.K., Awudzi, G.K., Amponsah, E., Darko, G. (2023). Knowledge, perception, and pesticide application practices among smallholder cocoa farmers in four Ghanaian cocoa-growing regions. *Toxicology Reports*, 10, 46-55.

Sevim, Ş., Boyacı, M., Gülmez, M., Ateş, E., Karakaş, U.S., Kaya, C., Bars Orak, A. (2023). Pestisit Kullaniminda Üreticilerin Bilgi Düzeyi: Diyarbakir İli Örneği. A*vrasya Sosyal ve Ekonomi Araştırmaları Dergisi,* 10(1), 247-257.

Shen, H., Li, Z., Jiang, Y., Pan, X., Wu, J., Cristofori-Armstrong, B., ... & Yan, N. (2018). Structural basis for the modulation of voltage-gated sodium channels by animal toxins. *Science*, *362*(6412), eaau2596.

Sharma, A., Kumar, V., Bhardwaj, R., Thukral, A.K. (2017). Seed presoaking with 24-epibrassinolide reduces the imidacloprid pesticide residues in green pods of Brassica juncea L. *Toxicological & Environmental Chemistry,* 99(1), 95–103.

Ecer, K., Güner, O., Çetin M. (2021). Avrupa Yeşil Mutabakatı ve Türkiye Ekonomisinin Uyum Politikaları. *İşletme ve iktisat çalışmaları dergisi,* 9(2), 125-144.

Angon, P. B., Mondal, S., Jahan, I., Datto, M., Antu, U. B., Ayshi, F. J., & Islam, M. S. (2023). Integrated Pest Management (IPM) in Agriculture and Its Role in Maintaining Ecological Balance and Biodiversity. *Advances in Agriculture,* 2023(1), 5546373.

Ayilara, M. S., Adeleke, B. S., Akinola, S. A., Fayose, C. A., Adeyemi, U. T., Gbadegesin, L. A., ... & Babalola, O. O. (2023). Biopesticides as a promising alternative to synthetic pesticides: A case for microbial pesticides, phytopesticides, and nanobiopesticides. *Frontiers in Microbiology,* 14, 1040901.

Uygun, N., Ulusoy, M.R., Satar, S. (2010). Biyolojik mücadele. *Türkiye Biyolojik Mücadele Dergisi,* 1(1), 1-14.

Lenteren, J.C. (2000). A greenhouse without pesticides: fact or fantasy?. *Crop protection,* 19(6), 375-384.

Marrone, P. G. (2024). Status of the biopesticide market and prospects for new bioherbicides. *Pest Management Science*, *80*(1), 81-86.

Thakore, Y.B. (2006). The biopesticide market for global agricultural use. Industrial Biotechnology, 2(3), 194-208.

Essiedu, J.A., Adepoju, F.O., Ivantsova, M.N. (2020). Benefits and limitations in using biopesticides: A review. AIP Conference Proceedings, 2313(1), 010001.

Kumar, J., Ramlal, A., Mallick, D., & Mishra, V. (2021). An overview of some biopesticides and their importance in plant protection for commercial acceptance. Plants, 10(6), 1185.

Delgado-Carrillo, O., Martén-Rodríguez, S., Ashworth, L., Aguilar, R., Lopezaraiza-Mikel, M., & Quesada, M. (2018). Temporal variation in pollination services to Cucurbita moschata is determined by bee gender and diversity. Ecosphere, 9(11), e02506.

Arthurs, S., & Dara, S. K. (2019). Microbial biopesticides for invertebrate pests and their markets in the United States. *Journal of invertebrate pathology,* 165, 13-21.

Stevenson, P. C., Isman, M. B., & Belmain, S. R. (2017). Pesticidal plants in Africa: A global vision of new biological control products from local uses. *Industrial Crops and Products,* 110, 2-9.

Karakaş,, M. (2018). Bitkisel İnsektisitler. *Türk Bilimsel Derlemeler Dergisi,* 11(2), 32-37.

Laxmishree, C., Nandita, S. (2017). Botanical pesticides – a major alternative to chemical pesticides: A review. *Int. J. of Life Sciences*, 5(4), 722-729.

Bomzan, D.P., Bhavya, M.L., Chandu, A.G.S., Manivannan, S., Lavanya, G., Lamasamy, K., Pasha, A. (2018). Potential of pyrethroid-synergised pyrethrum on stored product insects and implications for use as prophylactic sprays. *J Food Sci Technol.,* 55(6), 2270-2278.

Mossa, A.H., Mohafrash, S.M.M., Chandrasekaran, N. (2018). Safety of Natural Insecticides: Toxic Effects on Experimental Animals. *Biomed Res Int.,* 16, Article 4308054.

Jeran, N., Grdiša, M., Varga, F., Šatović, Z., Liber, Z., Dabić, D., Biošić, M. (2021). Pyrethrin from Dalmatian pyrethrum (Tanacetum cinerariifolium (Trevir.) Sch. Bip.): biosynthesis, biological activity, methods of extraction and determination. *Phytochemistry,* 20, 875-905.

Boyce, W.M., Lawler, S.P., Schultz, J.M., Mccauley, S.J., Kimsey, L.S., Niemela, M.K., Nielsen, C.F., Reisen, W.K. (2007). Nontarget Effects Of The Mosquito Adulticide Pyrethrin Applied Aerially During A West Nile Virus Outbreak In An Urban California Environment. *Journal of the American Mosquito Control Association,* 23(3), 335-339.

Diogo, B.S., Antunes, S.C., Rodrigues, S. (2023). Are biopesticides safe for the environment? Effects of pyrethrum extract on the non-target species Daphnia magna. *Environmental Toxicology and Pharmacology,* 99, 104114.

Souto, A. L., Sylvestre, M., Tölke, E. D., Tavares, J. F., Barbosa-Filho, J. M., & Cebrián-Torrejón, G. (2021). Plant-derived pesticides as an alternative to pest management and sustainable agricultural production: Prospects, applications and challenges. *Molecules,* 26(16), 4835.

Fulton, M. H., Key, P. B., & Delorenzo, M. E. (2013). Insecticide toxicity in fish. *In Fish physiology* (Vol. 33, pp. 309-368). Academic Press.

Soni, V., Anjikar, A. (2014). Use of Pyrethrin/ Pyrethrum and its Effect on Environment and Human: A Review. *PharmaTutor*., 2 (6), 52-60.

Jeran, N., Grdiša, M., Varga, F., Šatović, Z., Liber, Z., Dabić, D., Biošić, M. (2021). Pyrethrin from Dalmatian pyrethrum (Tanacetum cinerariifolium (Trevir.) Sch. Bip.): biosynthesis, biological activity, methods of extraction and determination. *Phytochemistry,* 20, 875-905.

Casalegno, M., Sello, G., & Benfenati, E. (2006). Top-priority fragment QSAR approach in predicting pesticide aquatic toxicity. *Chemical research in toxicology,* 19(11), 1533-1539.

Schmidt, S., Schindler, M., Faber, D., & Hager, J. (2021). Fish early life stage toxicity prediction from acute daphnid toxicity and quantum chemistry. *SAR and QSAR in Environmental Research,* 32(2), 151-174.

Tarakcı, Ü., & Türel, İ. (2009). Halk sağlığı amaçlı kullanılan pestisitlerin (Biyosidal) güvenilirlik standartlarının karşılaştırılması. *Yüzüncü Yıl Üniversitesi Veteriner Fakültesi Dergisi,* 20(1), 11-18.

United States. 1976. Federal Insecticide, Fungicide, and Rodenticide Act Amendments of 1975. Public Law 94-140. 90 Stat. (2003). Retrieved from https://www.govinfo.gov/content/pkg/STATUTE-90/pdf/STATUTE-90-Pg2003.pdf#page=10

Muratov, E. N., Bajorath, J., Sheridan, R. P., Tetko, I. V., Filimonov, D., Poroikov, V., ... & Tropsha, A. (2020). QSAR without borders. *Chemical Society Reviews,* 49(11), 3525-3564.

Tinkov, O., Polishchuk, P., Matveieva, M., Grigorev, V., Grigoreva, L., & Porozov, Y. (2021). The influence of structural patterns on acute aquatic toxicity of organic compounds. *Molecular Informatics,* 40(9), 2000209.

Keşkek Karabulut, Y., Yalçın Gürkan, Y. (2023). Investigation of Some Azo Dyes by QSAR Method and Acute Toxicity Test with Daphnia Magna. *Journal of the Institute of Science and Technolog,* 13(2), 1110-1119.